Actin Polymerization Dynamics at the Leading Edge

Xiaohua Hu

Dissertation submitted to Faculty of Virginia Polytechnic and State University in partial fulfillment of the requirements for the degree of

Doctor of Philosophy
In
Biological Sciences

Jeffrey R. Kuhn
Diya Banerjee
Daniel Capelluto
Jianhua Xing

October 5, 2012
Blacksburg, Virginia

Keywords: Cell movement; Actin; Actin capping proteins; Actin-related protein 2-3 complex

Actin Polymerization Dynamics at the Leading Edge

Xiaohua Hu

Abstract

Actin-based cell motility plays crucial role throughout the lifetime of an organism. While the dendritic nucleation model explains the initiation and organization of the actin network in lamellipodia, two questions need to be answered.

In this study, I reconstructed cellular motility *in vitro* to investigate how actin filaments are organized to coordinate elongation and attachment to leading edge. Using total internal reflection fluorescence microscopy of actin filaments, we tested how profilin, Arp2/3, and capping protein (CP) function together to propel beads or thin glass nanofibers coated with N-WASP WCA domains. During sustained motility, physiological concentrations of Mg^{2+} generated actin filament bundles that processively attached to the nanofiber. Reduction of total Mg^{2+} abolished particle motility and actin attachment to the particle surface without affecting actin polymerization, Arp2/3 nucleation, filament capping, or actin shell formation. Addition of other types of crosslinkers restored both comet tail attachment and particle motility. We propose a model in which polycation-induced filament bundling sustains processive barbed end attachment to the leading edge.

I lowered actin, profilin, Arp2/3, and CP concentrations to address the generation of actin filament orientation during the initiation of motility. In the absence of CP, Arp2/3 nucleates barbed ends that grow away from the nanofiber surface and branches remain stably attached to nanofiber. CP addition causes shedding of short branches and barbed end capture by the nanofiber. Barbed end retention by nanofibers is coupled with capping, indicating that WWCA

and CP bind simultaneously to barbed ends. In pull-down assays, saturating CP addition only blocks WWCA binding to barbed end by half. Labeled WWCA bound to barbed ends with an affinity of 14 pM and unlabeled WWCA with an affinity of 75 pM. CP addition increased WWCA binding slightly at low CP concentrations and decreased WWCA binding to 50% at high CP concentrations. Molecular models of CP and WH2 domains bound respectively to the terminal and penultimate actin subunit showed no overlap and that CP orientation might blocks WWCA dissociation from the penultimate subunit. Simultaneous binding of CP and WWCA to barbed ends is essential to the establishment of filament orientation at the leading edge.

Dedication

Dedicated to my parents, Qingmei Yang and Gensheng Hu.

Acknowledgements

I am very grateful for my mentor, Dr. Kuhn, for his guidance, encouragement, inspiration and assistance throughout my graduate study and in the preparation of this dissertation.

I wish to express my sincere appreciation to my committee members, Drs. Diya Banerjee, Daniel Capelluto, Jianhua Xing for their valuable comments and suggestions in conducting my research project and support throughout my graduate study.

I would like to also extend my sincere thanks to my previous and current lab members Ying Li, Nimisha Khanduja, Brent Bowdon, and Sihui Zhang for their friendships, technical discussions, and support during my graduate study. I will forever cherish the memories of the good times I had with them. I also thank the faculty, staff, and graduate students of the Department of Biological Sciences for their support during my graduate study.

Finally, I would like to thank my parents, for their unconditional love and support. I would also like to thank my husband, for his 80,000 miles commute from Pittsburgh to Blacksburg in the past five years, for his love, faith, patience and understanding.

Table of Contents

List of Figures

List of Tables

Chapter 1 Literature Review

Introduction – Cell Motility as an Actin-based process

Cell motility plays an essential role in many physiological and pathological processes. During embryonic development, cell migration is required for morphogenetic processes such as gastrulation. In vertebrate embryogenesis, neutral crest cells also undergo cell migration to form several tissues. Wound healing and immune response are also coupled with cell migration. Finally, carcinoma cells spread through metastatic cell migration [1].

To migrate, cells undergo a four-step cycle: (1) protrusion of the leading edge in response to extracellular signals and linked flow of the actin cytoskeleton rearward; (2) formation of focal adhesions between the actin cytoskeleton and the extracellular matrix; (3) retraction of the rear to allow the cell to move forward; and (4) disassembly of focal adhesion sites at the rear [2]. This dissertation focuses on protrusion of the leading edge (step 1). Directed cell migration requires spatially controlled and continuous actin nucleation and coordinated turnover of actin filaments in a flat protrusion called the lamellipodia: a branched actin filaments network in the leading edge that produces physical protrusive forces as the polymers grows beneath the plasma membrane.

Several systems have been used to model the motility process in vitro. The pathogens Listeria monocytogenes and shigella flexneri travel within and between host cells by subverting the host cell's actin-based protrusion mechanism. Actin-based motility of the bacteria or of functionalized microspheres can be reconstituted in vitro from a core set of proteins including actin, Arp2/3 complex, profilin, capping protein, and ADF/cofilin. The reconstituted actin-based motility assay allows testing of the function of the putative regulators of actin motility, discovery

and testing of new actin dynamic mechanisms, and resolving controversies about the mechanism of actin dynamics at the leading edge.

1. Actin assembly thermodynamics and kinetics

Protrusion of a motile cell's membrane is driven by actin filament polymerization at the leading edge, which in turn depends on free filament ends. De novo initiation of new actin filaments is rare, due to the instability of actin dimer and trimer filament nuclei [3] (**Figure 1.1**)and sequestering proteins such as profilin that inhibit nucleation. Thus, cells require nucleators such as formins, Arp2/3 complex, and Spire to initiate new actin filaments. Once nucleated, filaments rapidly elongate at the fast-growing barbed end, where actin subunits associate with a diffusion-limited rate constant [4].

As filaments grow, actin subunits hydrolyze their bound ATP and release the free phosphate. Hydrolysis and phosphate release drives the different polymerization kinetics at each filament end and provides a natural clock that structurally indicates filament age. Once polymerized, Mg-ATP-actin subunits at the barbed end rapidly hydrolyze their γ-phosphate with a half-time of 2 seconds [5] and slowly release their γ-phosphate to form Mg-ADP-actin with a half-time of 6 min [6, 7](**Figure 1.1**).

The fast growing barbed end and slow-growing pointed end behave differently in buffer containing ATP. Phosphate binds and dissociates on ADP-actin subunit at both ends much more rapidly than in the middle of the filament, which could explain the effects of phosphate on depolymerization. In addition the affinity of pointed ends for phosphate appears to be lower than the rest of the filament. Pollard proposed that although the mechanism of this surprising thermodynamic difference is not understood, it must arise from cooperative interactions among

the subunits near the end of the filament. The mechanism such as the rates of phosphate binding and dissociation on ADP-actin monomers and along the filament still need more investigation [8].

While ATP hydrolysis is rapid in filaments, hydrolysis is much slower on actin monomers and is further inhibited by the ubiquitous actin monomer sequestering protein, thymosin β4 [8]. In contrast, the exchange of spent ADP for fresh ATP occurs rarely in actin filaments but more rapidly on monomers. Nucleotide exchange on monomer is accelerated by the monomer binding protein profilin. Profilin binding opens the nucleotide binding cleft of an actin monomer, greatly increasing nucleotide association and dissociation rates [8]. A high ratio of ATP to ADP in resting cells drives the formation of profilin-ATP-actin complexes that rapidly bind to free filament barbed ends followed by profilin dissociation.

2. Dendritic nucleation model at the leading edge

Actin-based cell motility plays a crucial role throughout the lifetime of organism. The front or leading edge of a typical crawling cell forms a broad, fan-like lamellipodial protrusion that contains a branching actin filament network generated by the Arp2/3 complex [9, 10]. In the dendritic nucleation model of actin-based cell motility [11, 12](**Figure 1.5**), binding of nucleation promoting factors (NPFs), such as Wiskott–Aldrich syndrome protein (WASP) or WASP-family verprolin-homologous protein (WAVE) to the leading edge membrane exposes their active C-terminal WASP homology 2 (W or WH2), central (C), and acidic (A) domains. Exposed WCA domains bind to an actin monomer and to the Arp2/3 complex to form a complex that binds to the side of an existing filament to generate a new, rapidly-polymerizing filament with its barbed end directed towards the membrane. The combined force of many growing actin filament barbed ends push the cell membrane outwards until each filament's growth is halted by barbed end capping protein (CP), which keeps actin filaments short and stiff. ATP-actin

filaments are slowly hydrolyzed to ADP, providing a natural timing mechanism that delineates filament age and distance from the advancing membrane. Cofilin binds to and severs older ADP-actin filaments some distance away from the leading edge, and the severed oligomers rapidly depolymerize into ADP-actin monomers. Profilin replaces cofilin on actin monomers and promotes actin nucleotide exchange to provide a fresh pool of ATP-actin for filament polymerization. Profilin also suppresses *de novo* actin nucleation. In vitro these proteins are sufficient to reconstitute sustained, actin-based motility [13]. The details of each step and evolved protein are reviewed below.

Arp2/3 complex activation

To maintain a constant actin treadmilling rate, migrating cells must continue nucleating actin filaments to balance the blocking of free barbed ends by capping protein. In the lamellipodium of migrating cells, Arp2/3 complex serves as the primary nucleation factor and is activated by Nucleation Promoting Factors (NPFs) [1].

The Arp2/3 complex is composed of seven subunits: two actin-related proteins, Arp2 and Arp3, stabilized in an inactive state by five other subunits (**Figure 1.1**): ARPC1 (for the 40-kD subunit), ARPC2 (35-kD subunit), ARPC3 (21-kD subunit), ARPC4 (20-kD subunit), and ARPC5 (16-kD subunit). Among these subunits, Arp2 and Arp3 bind ATP [8]. NPFs for Arp2/3 always have three functional domains at the C-terminus: the WASP homology 2 domains (WH2 or W, frequently designated as V for verprolin-homology domain), the central (C) domain (erroneously called cofilin homology in early work), and a negatively chargedacidic (A) domain. Together, the VCA domain remains largely unstructured while binding with actin monomer or Arp2/3 complex[8](**Figure 1.4**). The CA domain of NPFs interacts with the Arp2/3 complex, while the W domain binds an actin monomer [14]. W motifs are approximately 20 residues in

length and form a three-turn, amphipathic α-helix followed by an extended chain. The α-helix binds the barbed end of actin monomers at the hydrophobic cleft between subdomains 1 and 3 according to the crystal structures [15]. The extended chain (C-terminal to the helix) binds along the surface of actin between subdomains 2 and 4. C motifs bind both actin and Arp2/3 complex [16] and acts like a linker between W motif/actin monomer and A motif/Arp2/3. The conformational change of Arp2/3 caused by NPFs activation was examined by Goley et al. [17] by using fluorescence resonance energy transfer (FRET). They use both CFP and YFP to tag the C termini of ARPC1 and ARPC3. Their results showed that binding of nucleotides increased the energy transfer between the fluorescence probes, and WCA could further increase the energy transfer. In addition, nucleotide binding favors WCA binding and *vice versa* [17, 18].Activation of Arp2/3 complex requires NPFs, mother filaments, and actin monomers working cooperatively (**Figure 1.2**). Mother filaments alone are not enough to activate Arp2/3 complex [17], but in the absence of mother filaments nucleation by Arp2/3 complex, WCA, and actin monomers remains slow [19]. A recent model indicates that Arp2/3 complex has two distinct binding sites for WCA. One site is on Arp3 and the second is on APRC1 and Arp2 [20, 21]. A complex of VCA_2 : $actin_2$: Arp2/3 forms in Arp2/3 activation and branch formation. The two bound WCAs have distinct roles. WCA bound to Arp2 delivers actin to Arp2 with high affinity but activates Arp2/3 complex weakly, while WCA bound to Arp3 delivers actin to Arp3 with low affinity but is critical for activity. This suggests that nucleation fundamentally proceeds through two VCAs and two actins, even when presented as monomers.

Nucleation of actin filaments by the Arp2/3 complex

The cooperation of VCA, Arp2/3 complex, actin monomer, and the mother filament is essential for branch formation (**Figure 1.2**). The hypothesis that Arp2 and Arp3 mimic the first

two subunits at the pointed end of the daughter filament was confirmed by two-dimensional cryo-electron microscopic reconstructions of branches [22]. In the inactive form of the complex, the two Arps are separated in the crystal structures [23, 24] by a large distance (**Figure 1.3**). A substantial conformational change is thus required to bring them together to form the pointed-end mimic upon activated (**Figure 1.3**).

The first three-dimensional reconstruction of actin filament branches [25] showed how the two Arps are brought together to activate the complex and initiate daughter filament formation (**Figure 1.3**). Upon activation , the CA domain of NPFs, Arp2 moves approximately 2 nm to overlap by 50% with Arp3 in the active form. In the active structure, the interaction surfaces of between Arp3, Arp2, and the first and second actin subunits in the daughter filament are conserved and similar to successive subunits along the short-pitch helix of an actin filament [26]. Subdomains 3 and 4 of Arp3 and ARPC3 also rotate modestly during activation into an actin-subunit like conformation, whereas the rest of the complex is stationary. Although cryo-electron microscopy showed the endpoints of this motion, the mechanism of arp2 motion remains unclear. Two possible mechanism potentially drive this movement: (1) Arp2 dissociates from ARPC1 and ARPC4, while the N terminus of ARPC5 acts like a flexible tether between Arp2 and the rest of the complex; or (2) Arp2 could be repositioned next to Arp3 by bending motion with no dissociation of Arp2 from ARPC1 and ARPC4 [8].

The active branch model [25] also shows that the conformations of two of five mother filament actin subunits that interact with Arp2/3 complex undergo conformational change upon Arp2/3 binding (**Figure 1.3**). These changes “open up” actin subunits to create a larger binding interface between Arp2/3 and the mother filament. Suprisingly, all seven subunits of Arp2/3 complex interact with the mother filament in the branch model with the interface buried over

9000 $Å^2$ of surface, consistent with the rigidity of the junction [19]. Other groups have also shows similar contacts of ARPC2/ARPC4 with the mother filament [15].

ATP binding and hydrolysis in branch junction

ATP hydrolysis by Arp2/3 complex and actin could influence the formation and stability of branches. Like actin monomer, neither Arp hydrolyzes ATP in the inactive complex [27]. For Arp2 the mobility of subdomains 1 and 2 may preclude ATP hydrolysis until a branch is formed. For Arp3, the displacement of the catalytic histidine from its position might lead to low ATPase activity of Arp3 [23].

Arp2/3 complex with bound ATP binds NPFs with higher affinity than with bound ADP, and ATP binding to Arp2/3 complex is required for nucleation of daughter filaments. Moreover Arp2 hydrolyzes ATP much faster than does Arp3. These are the consistent conclusion from three groups [18, 28, 29]. Controversy remains over the rate of ATP hydrolysis by Arp2 and the possible effect of ATP hydrolysis in nucleation and dissociation of branches from mother filaments. Due to the difficulty to focus on the hydrolysis of Arps instead of actin, these experiments are done with radiolabeled ATP covalently cross-linked to the Arps and with unlabeled ATP in the buffer and on actin.

The timing of ATP hydrolysis by Arp2 is controversial. Le Clainche et al. [30] reported that bovine Arp2 hydrolyzes ATP on greater than one minute timescale, well after branches form, while others found that amoeba and yeast Arp2 hydrolyze ATP rapidly in less than 1 min after branch formation [18, 28, 29]. Moreover, Dayel & Mullins [29] showed that ATP hydrolysis by Arp2 is not triggered by binding Arp2/3 complex with an NPF to a mother actin filament; instead, it happens after the daughter filament starts to grow. The addition of the first actin subunit in the daughter filament stimulates Arp2 to hydrolyze ATP. This observation is similar to subunit

interactions within actin filaments stimulating ATP hydrolysis. Martin et al. [28] agree that Arp2 hydrolyzes crosslinked ATP during the course of branch formation. Based on the observation that Arp2 with the H161A mutation, defective in ATP hydrolysis, could nucleate branches, the authors concluded that as in actin, hydrolysis is associated with but not required for nucleation.

Whether the nucleotide state of actin influences the branch formation remains an open question. Fluorescence microscopy showed more branches on younger sections of mother filaments with ATP-actin (51). However, ADP-actin mother filaments, ADP-Pi mother filaments, and aging ATP mother filaments have the same branches assembly rate [31]. In contrast, the density of branches declines exponentially over time [32, 33], with the same half time (6 min) as dissociation of phosphate from ADP-Pi-actin filaments [7]. Thus, the branch disassembly (debranching), rather than branch assembly, is likely influenced by nucleotide state. Whether debranching is correlated with phosphate dissociation from the Arp2/3 complex, the mother filament, or the daughter filament has yet to be determined. Le Clainche et al. [30] observed that both ATP hydrolysis by Arp2 and branch dissociation took place over several hundred seconds, thus they claimed that they are related, but others found that Arp2 hydrolyzes ATP on a timescale of seconds during branch formation [18, 28, 29], which provide contrast evidence for Le Clainche et al's claim. Considering that these experiments are all conducted with real time fluorescence microscopy, one need to compare the number of branches formed in bulk solution because many more branches form in solution than observed by microscopy [31]. The difference was attributed to rapid dissociation of branches that never grow long enough to be distinguished from the mother filament.

Nucleation promoting factors in cell migration

Nucleation Promoting Factors (NPFs) that activate Arp2/3 are themselves primarily activated by the Rho-family GTPases, including Rac1, Cdc42, and RhoA, which induce the formation of ruffles, filopodia, and stress fibers, respectively [34]. The Wiskott-Aldrich syndrome family of Arp2/3 activating proteins (WASP) control actin assembly downstream of Cdc42 and Rac1. The WASP family in vertebrates includes: WASP, expressed only in hematopoietic cells; Neuronal-WASP (N-WASP), which is expressed ubiquitously; and SCAR (suppressor of cAMP receptor) /WAVE (WASP-family verprolin homology protein) isoforms 1, 2, and 3. [35, 36].

Each Arp2/3 activator has distinct activities and regulates specific cellular functions. N-WASP is 16-fold more active at stimulating Arp2/3-based nucleation than WASP and 68-fold more active than Scar1/WAVE1 in solution [37]. N-WASP/WASP is important in filopodia formation and endocytosis in response to Cdc42 [38],while WAVE isoforms are responsible for lamellipodium protrusion in response to Rac1 [39].

By coupling actin assembly to different membrane curvature proteins, N-WASP and WAVE also regulate different aspects of membrane shape. One major membrane curvature protein interacting with NPFs is Bin-Amphiphysin-Rvs161/167 (BAR) domain-containing proteins [40]. Several BAR-NPF interactions have been shown to induce various shapes of membrane protrusions including lamelipodia and filopodia, or invaginations including trafficking organelles such as endosomes and clathrin coated pits. BAR domains differs in their membrane-binding surfaces, allowing them to sculpt membranes differently to generate either invagination or protrusions. Most BAR proteins contain an SH3 domain, through which they bind to proline rich domain in NPFs. BAR domain proteins could further divided into three distinct classes (BAR, F-

BAR and I-BAR) based on amino acid sequence similarity [40]. N-WASP associates with BAR domain-containing proteins such as endophilin [41] and F-BAR domain-containing proteins such as syndapin-I [42]. By associating with N-WASP, these BAR domain proteins that sense positive inward membrane curvature promote membrane invagination in endocytosis [43]. In contrast, WAVE2 interacts with the I-BAR domain containing protein Irsp53 [44], which sense negative inward membrane curvature. I-BAR/WAVE thus induces membrane protrusion. An in-depth dissection of the spatial and temporal localization of Arp2/3 regulators in relation to proteins that bind to curved membranes is required to obtain a full map of the contribution of membrane curvature to Arp2/3 induced cell shape changes.

Arp2/3 Activators – WASP and N-WASP

N-WASP and WASP are modular proteins consisting of a NH2-terminal WASP homology 1 domain (WH1), followed by a basic region (B), a GTPase binding domain (GBD), a proline-rich domain (PRD), and a COOH-terminal WCA domain as described in section of Arp2/3 complex activation (**Figure 1.4**). N-WASP has two consecutive W domains, while WASP has one. N-WASP and WASP are autoinhibited by intramolecular binding between the WCA and GBD domains. The binding of Cdc42-GTP and PIP_2 to the GBD and the basic domains, respectively, dissociates GBD from the VCA domain to relieve the autoinhibition and activate N-WASP synergistically [45]. The unmasked WCA domain interacts with Arp2/3, actin monomer, and actin filament nucleate actin.

In a physiological context, the previous described components are not sufficient to mediate Cdc42 induced N-WASP/WASP activation. The majority of cytosolic N-WASP and WASP are found in complex with Wasp-interacting protein (WIP) [46]. WIP binds to the WH1 domain and

stabilizes the inactive form of N-WASP or WASP in the absence of activating signals. Upon activation, a BAR family protein, TOCA-1 (transducer of Cdc42-dependent actin assembly 1), binds to both Cdc42 and a WIP-WASP complex through its SH3 domain, and is required for Cdc42 induced N-WASP/WASP activation [47]. Therefore, TOCA1 serves as an essential component of Cdc42 pathway.

Cdc42 is not the only activator for N-WASP. The Rho GTPase Rac1 also activates N-WASP through a similar mechanism [48]. In addition to GTPases, SH3 domain-containing proteins such as Grb2, Nck, or Abi1 target the proline-rich region of N-WASP to help relieve autoinhibition and activate N-WASP [49-51]. More recently, IQGAP1, a protein with multiple binding partners including actin filaments, the microtubule binding proteins CLIP-170 and APC, the adherens junctions proteins E-cadherin and β-catenin, the Rho GTPases Cdc42 and Rac1, and calmodulin [52] was found as a novel activator of N-WASP [53, 54]. Bensenor et al. proposed that IQGAP1 links activation of the fibroblast growth factor (FGF) receptor FGFR1 [53] to Arp2/3 nucleation of actin filaments at the leading edge.

Phosphorylation also plays a role in N-WASP/WASP activation. Torres and Rosen [55] demonstrated that the after activation by Cdc42, Y291 of WASP is exposed and could be phosphorylated by Src kinase. This phosphorylation inhibits the autoinhibitory interaction and keeps WASP in its active conformation after Cdc42 dissociation [55]. Moreover, Cory et al. [56] also discovered that two serines (S483 and S484) located in the VCA domain could be phosphorylated by casein kinase II. Interestingly, this phosphorylation does not require the previous activation of WASP. WASP phosphorylation increases its affinity for Arp2/3 and results in a higher stimulation of actin assembly both *in vitro* and *in vivo* [56]

Barbed end capping proteins

Heterodimeric CP (CapZ) binds tightly to the barbed end and prevents actin subunit addition. It is found in every eukaryotic organism and every metazoan cell type. Knockdown of CP abolishes the formation of lamillipodia, removes Arp2/3 complex from the leading edge and induced excess of filopodia [57].

CP consists of two subunits, α and β, that share sismilar secondary and tertiary structure although the sequence similarity is very low. Each subunit is around 30 KD and unstable unless heterodimer is formed. One CP binds one actin barbed end with high affinity (10 – 100 nM) and prevent subunit addition to barbed end [57]. CP remains active for capping actin in the absence or presence of divalent cation and with variety of salt, osmolarity and pH. The actin "funneling" model proposes that capping protein decreases the number of free barbed ends, and thus increase the concentration of soluble monomeric actin, thus increase the rate of filament elongation [58]. However, this model is challenged recently by observations that increasing capping protein concentration does not increase the concentration of monomeric actin available during steady-state motility or symmetrical shell growth, and capping protein also has no effect on the average number of free barbed ends contributing to the motility or the overall actin assembly [59].

The structure of CP resembles mushroom with two subunits arranged with a peudo-two-fold axis of rotational symmetry. Narita et al. proposed the structure of CP on filament barbed end. To interact with barbed end, a primary contact is made by C terminus of α subunit and the body of β subunit. In the second step, a flexible C terminus of β subunit binds to the hydrophobic cleft on actin. The mobility of this tenacle-like amphipathic α-helix allows CP to move ("wobble") at barbed end, which may allow other molecule to bind [60].

In vitro experiments testing the dynamics of interaction between capping protein and barbed ends shows that the dissociation rate constant of capping protein from barbed ends is very low, 0.0005 s^{-1}, while *in vivo* measurement using fluorescence speckle microscopy shows that the dissociation constant rate is three orders of magnitude shorter (0.58 s^{-1}), indicating the existence of uncapping mechanisms in the cell. The protein CARMIL removes CP from barbed end, serving as an "uncapper". Phosphatidylinositol 4,5-bisphosphate (PIP_2) also inhibits the activity of CP by binding to three conserved basic residues on the surface of CP near C-terminus of α-subunit. The binding sites of PIP_2 and actin on CP may overlap [57]. Single molecular kinetic analysis further revealed that $PI(4,5)P_2$, $PI(3,4)P_2$, and $PI(3,4,5)P_3$ prevent mouse CP from binding to barbed ends but cannot dissociate CP from barbed end, indicating that phosphatidylinositol lipids are not "uncappers"**[61]**. Several proteins indirectly regulate CP. Formin protein, another actin nucleator binding to filament barbed end, acts as competitors of CP at barbed end. Vasolilatoe-stimulated phosphorylation (VASP), a processive actin polymerase at barbed end, functions as an antagonist of CP [57, 62].

Profilin

Profilin is 15 KD protein that was first purified with actin monomer from calf thymus. Mammals have 4 profilin isoforms whereas *c.elegans* has 3 and plants have more than 10 isoforms. Profilin 1 from mammal expressed is in all tissues with cellular concentration of more than 50 μM. Profilin is enriched in plasma membrane of locomoting or spreading animal cells, and internal membranes that involved in vesicular transport and nucleus. Mice deficient in profilin 1 fails to develop beyond blastocyst stage and results in embryonic death. Profilin 1 also play an important role in actin dynamics during neuritogenesis and synaptic plasticity [63].

Profilin has the capacity to interact with 4 classes of ligands. Profilin binds to actin monomer with dissociation constant of 20 nM – 1 μM. Nucleotide free actin has the highest binding affinity to profilin whereas profilin has 20 fold lower affinity for ADP actin than for ATP actin. Because profilin-actin interaction results in a slight deformation of actin and stabilization of an actin conformation with a wide nucleotide pocket, profilin facilitates nucleotide exchange of bound ADP and ATP by 1000 fold. Profilin allows ATP-actin-profilin to elongate at the similar rates to free actin monomers but blocks binding to filaments pointed ends. In amoeba, the concentration of profilin and its affinity to actin are sufficient to account for the entire pool of unpolymerized actin monomers. Moreover, because profilin helps to recycle the actin monomers, profilin and cofilin working together could enhance the treadmilling rate by 125-fold [64]. Either Arp2 or Arp3 subunit can bind with profilin, enabling the addition of profilin-actin to Arp2/3 initiated branch. Profilin can also bind to poly-L-proline proteins (PLP) including Ena/Vasp, Wasp/Wave, and formin. 8-10 PLPs are required for this interaction. Profilin binds to phosphatidylinositol lipids including $PI(4,5)P_2$, $PI(3,4)P_2$, $PI(3,4,5)P_3$. $PI(4,5)P_2$ competes with poly-L-proline proteins and actin to bind with profilin [63].

ADF/cofilin

Cofilin expressed in all eukaryotes. Mammals have three isoforms of cofilin, actin dissociating factor (ADF), cofilin 1 and cofilin 2. ADF is more efficient in actin monomer sequestering, and knockout of ADF in mice leads to postnatal blindness [65]. Coflin 1 is the major form in non-muscle cells whereas cofilin 2 is the major form in muscle cells. Cofilin1 is more efficient in actin nucleation and filament severing, and knockout of cofilin 1 is embryonic lethal in mice [65].

Cofilin 1 binds to ADP actin subunits in actin filaments after phosphate is released. When the ratio of cofilin/actin in actin filament is low, cofilin 1 persistently severs actin filament. When the ratio is higher, cofilin1 severs actin filament rapidly and transiently and then stabilize actin filament in a twisted form [66]. When the concentration of cofilin1 is even higher, it nucleates short filamentous actin through severing. Once the concentration of cofilin1 exceeds the threshold or cells are energetically or oxidatively stressed , cofilin-actin will form bundles or rods. More recently, cofilin has also been shown to play an important role in debranching by competing directly with Arp2/3 complex to bind with filament[67].

Cofilin 1 is regulated by several factors including $PI(4,5)P_2$, pH and phosphorylation. $PI(4,5)P_2$ inhibits cofilin 1 activity by directly binding to cofilin 1. Because phosphate release is pH dependent, higher pH results in more cofilin 1 severing. LIM kinase phosphorylates cofilin and further inhibits cofilin 1 activity whereas slingshot dephosphorylates and activates cofilin 1. The upstream signals of cofilin 1 phosphorylation include oxidative stress, energetic stress, fluctuation of calcium, cAMP release and coronins [65].

Cofilin plays an important role in Alzhaimer disease and HIV infection. When cofilin-actin forms rod in neurons, protein tau would be hyperphosphorylated. This serves as a precursor of striated neutrophil threads, which is the hallmark for Alzhaimer disease. In HIV infection, cofilin inactivation by LIM kinase in T lymphocytes impairs cell motility and allows HIV viruses to evade immune-detection [65].

3. Reconstitution of actin-based motility *in vitro*

Tremendous progress has been made in the last two decades in understanding how actin networks assemble. A key innovation driving this research was the use of bacteria pathogen, such as *Listeria* and *Shigella*, that hijack the actin cytoskeleton of host cells to drive their

movement [68, 69]. The rate of actin-based motility of intracellular *Listeria* equals the rate of actin polymerization [70]. Motility of these pathogens was reconstituted in cell extracts, indicating that factors at the surface of pathogens are sufficient to recruit host cytoskeleton. The surface proteins responsible for the generation of branches actin network were later identified as NPFs of the Arp2/3 complex, ActA for *Listeria* [12, 71] or IscA for *Shigella* [72, 73]. These purified NPFs, when conjugated to artificial particles, triggers actin-based motility from the minimum pure proteins [74]. Thus, in vitro motility converts a complex cell biology problem into a biochemically tractable problem.

Critical factors to establish motility

The design of the minimum media for actin-based protrusion is the logical results from the regulation of actin dynamics. The critical factors to support sustained motility include actin, Arp2/3 complex, NPF bound particles, capping protein, profilin and motility buffer with desired ATP and ions.

Spatially controlled activation of Arp2/3 complex - Several different systems have been used to mimic the leading edge, including the ActA-protein coat of *Listeria* bacteria, the N-WASP binding protein IcsA of Shigella bacteria, and ActA- or N-WASP coated polystyrene-based (PS) beads, oil droplet, or giant unilamellar vesicles (GUVs) [58]. Each of these systems spatially controls the activation of Arp2/3 complex to generate a "comet tail" of polymerizing actin behind the bacteria, bead, or vesicle. Polystyrene (PS) beads are simple substrates that allow easy immobilization of proteins via hydrophobic interactions under controllable surface density of activators. PS beads with size ranging from 50 nm to 100 μM have been successfully used in reconstituted motility assay [58], with particles in the 0.2-1 μm range moving the fastest.

Compared to the solid PS beads, on which the activators occupy fixed position, soft microsphere-like oil drops or GUVs are closer to biological membranes and allow the activators diffuse on the surface. Activator (N-WASP, ActA) can be coated directly to the soft microphere, or the signal molecules like cdc42/RhoGDl complex, activator of N-WASP, can be attached to the lipid-coated beads to activate N-WASP as the first step [75].

Protein factors that enhance motility

Along with the essential components described above, several other proteins enhance the actin motility. Filament severing protein, crosslinkers and other nucleators are studied in symmetry breaking, force generation and sustained motility

Capping protein - At the suboptimal concentration of CP, particle movement is slow and actin branches grow away fromm rather than towards, the bacterium before becoming capped [58]. Carlier et al explain this bias in barbed end orientation by proposing that CP controls the density of the actin network by limiting the length of actin filaments. More recently, CP was found to be crucial in shell growth, symmetry breaking, and barbed end rearrangement by increasing the rate of Arp2/3 nucleation [59].

Profilin – Profilin inhibits the spontaneous actin nucleation outside the bacteria or artificial particle. With profilin, the actin nucleation is restricted to the NPF coated surface. In lengthy reactions, profilin also maintains actin monomers in a polymerizable state by facilitating nucleotide exchange.

Cofilin – Cofilin severs ADP bound actin filament and helps to maintain the actin monomer concentration. Addition of Cofilin to the motility medium increases the rate of *Listeria* movement and shorten the length of comet tail [76].

Cross-linking proteins - Addition of filament bundling proteins such as α-actinin [13], T-plastin [77], or fascin [78] to a standard *in vitro* motility assay increases the propulsion velocity of tethered beads or bacteria. Once filaments are nucleated with barbed ends facing the particle, Arp2/3 appears to be dispensable to propulsion. Brieher *et al* [78] showed that *Listeria* expressing ActA on their surfaces were rapidly propelled through cytoplasmic extract by fascin-bundled filaments, even after an Arp2/3 inhibitor was added. Bundling protein is also used in dissecting the mechanism of symmetry breaking. By modulating the physical properties of the actin network, α-actinin increases the time for symmetry breaking and comet tail formation in a concentration dependent manner [79]. Paluch et al further pointed out that the elasticity of the actin network, modulating by crosslinkers, is important in force generation [80].

VASP –Vasodilator-stimulated phosphoprotein (VASP) has various functions in regulating cell motility including actin filament nucleation, profilin and monomeric actin recruitment, anti-capping activity, filament detaching capability, and filament bundling [81]. In reconstitution assays, VASP binds to a central proline rich region of ActA at the surface of *Listeria* and enhances the movement of *Listeria* by increasing local formation of polarized and tethered actin filaments [8].

Biophysical parameters that influence motility

Surface density of NPFs - Groswasser et al proposed that changes in the surface density of WCA domain will markedly affect the velocity regime, shifting from a continuous to a jerky movement resembling that of the mutated "hopping" *Listeria* [82]. Delatour et al further pointed out that vesicle propulsion occurs in a restricted range of surface density of N-WASP. For His-tagged N-WASP coated to Ni-NTA-derivatized lipids, they found that optimum surface density was 0.19 ± 0.06 molecules/100 nm^2, corresponding to a mean distance of 23 nm between nearest

neighbors. At lower densities of N-WASP, the actin meshwork lacks the cohesive structure to break, and the vesicle remains in a homogenous actin shell. While at high densities of N-WASP, the pressure developed by the growth of actin gel is so high that the network collapses before breaking symmetry [75].

Microsphere diameter - Change of the bead diameter leads to the shift from a continuous to a jerky movement [82]. Cameron et al further found out that bead size has a profound effect on all aspects of motility, with increasing size causing slower, straighter movement and inhibiting symmetry breaking [83]. In contrast, smaller beads had increased trajectory curvature and faster movement.

Extract dilution - If the experiments are performed in cell extract, the dilution of extract reduces motility speed. However, the exact role that dilution has on motility has been difficult to determine as each component has a different roles in motility [83].

Methylcellulose - The presence of methylcellulose leads to an increase in the curvature of the particle's trajectory [83]. The role of methylcellulose in the velocity is still debated [84, 85]. Since methylcellulose increases medium viscosity, one group found increasing viscosity decreased particle velocity [REF], while another group argues that velocity is independent of the medium viscosity [REF].

Establishing sustained motility

For beads, bacteria, or vesicles coated uniformly with NPFs, actin polymerization must somehow become biased towards one side of the particle for sustained motility in one direction. Three steps are needed to initiate this biased movement: (1) the formation of nonpolarized shell (or "cloud") of filamentous actin around the particle, followed by (2) breakage of symmetry

(deformation), and finally, (3) the establishment of a stationary movement regime characterized by a comet tail of polymerizing actin behind the particle [84](**Figure 1.6**).

For soft beads with liposome surface, the concentration of active Arp2/3 is controlled by a biased localization of activators toward the rear of the particle. The activator must remain segregated on the surface for continuous movement to be sustained [86]. When a rigid particle is coated with an immobilized NPF, the polymerizing actin network itself must become biased towards one side of the particle In either case, symmetry breaking is essential to establish the directional movement of the bead or vesicle. The "cloud" of actin growing around coated beads loses symmetry by spontaneously "melting" on one side of the bead.(**Figure 1.6**) The actin comet tail subsequently develops at the other side, propelling the particle forward. In smaller beads, stochastic amplification of local variation in the number of free ends eventually lead to a biased actin growth at one side of the beads and disassembly at the other side. For larger beads, elastic models are more successful in describing the events because stochastic fluctuations are less significant in large beads. Growth of actin at the bead surface pushes the outer actin layer outward, stretching it and generating growing tangential stress. When a critical tangential stress is reached, a crack at the gel outer surface develops and propagates to the bead surface [83]. In soft lipid vesicles, Arp2/3 activators converts from homologous distribution to segregated distribution at only one side of the vesicle due to the fluid nature of the lipid vesicle [86].

How actin polymerization generates a protrusive force: Force-velocity models from the reconstituted assay

There are several models proposed to decipher the force-velocity relationship. In the "Tethered ratchet" model, filaments are attached to the surface during branching reaction, and then detached to allow the growth of the filaments: the growing detached filaments push while

the attached filaments pull on the surface. This model predicts the biphasic force-velocity relation: the velocity decreases rapidly at low loads and slowly at greater loads [87].

The "End-tracking motor" model, also called "actoclampin" model, proposes that two end-tracking motor subunits associate with the filament's tip. Assembly of the ATP-actin monomer to the tips will trigger the hydrolysis on the clamped penultimate actin subunit, leading to shift the motor subunit forward to attach the new assembled actin subunit. This model suggests the existence of a "stepping motor" coupling protrusion to ATP hydrolysis on the filament while the motor remains attached. Formin has been guessed to be this "end-stepping motor" because profilin-actin ATP hydrolysis cycle is coupled to the release of the formin subunit in the formin-coated beads motility assay [18]. However, formin is not present in many in vitro motility assays that clearly demonstrate sustained connections between the comet tail and the particle surface. The WH2 domain of N-WASP is also proposed to be the candidate of "end-stepping motor", except for that no ATP hydrolysis is involved in N-WASP binding to the barbed end [75].

The "Elastic propulsion" model suggests that the propulsion is a balance between the elastic stress squeezing the object forward and the actin-surface friction lagging the objects backward. The elastic stress is generated by actin polymerization near the surface. This model predicts a convex shaped force-velocity curve [87].

Summary

The dendritic nucleation model explains how actin branching mediated by the Arp2/3 complex directs the rapidly polymerizing filament barbed ends towards the membrane, and how the combined forces of many growing actin filaments push the cell membrane outwards. Much of our understanding of this dendritic nucleation model was contributed by reconstitution of

actin-based motility. Motility reconstructions *in vitro* thus provide a powerful tool to study actin network dynamics at the leading edge.

Although compelling, the dendritic nucleation model cannot fully explain filament architecture and dynamics at the leading edge. Specifically, several questions must be addressed (1) how filament networks remain attached to the leading edge as they grow, (2) how bundled filaments can propel an NPF coated particle, (3) why barbed ends are oriented toward the membrane, and (4) how capping protein influences filament nucleation and orientation. By using NPF-coated nanofiber to reconstruct actin based motility (**Figure 1.7**), the work I present in next two chapters provides compelling answers to each of these questions.

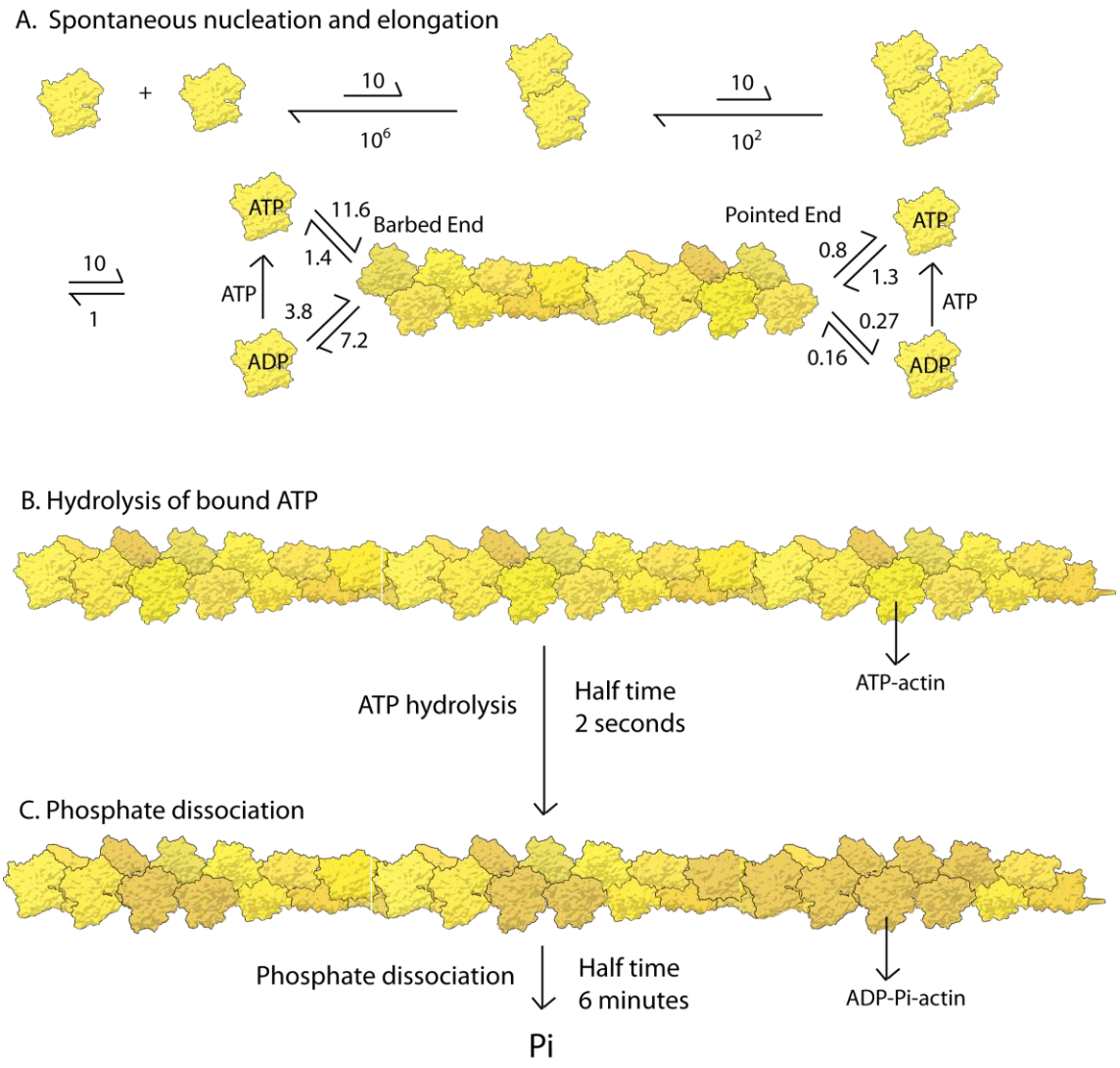

Figure 1.1.Actin spontaneous nucleation and elongation, ATP hydrolysis, and phosphate dissociation.

(A) Spontaneous nucleation and elongation. Dimer and trimer are unstable. Once nuclei formed, filament starts to elongate rapidly at barbed end and slowly at pointed end. Rate constants are shown with units of μM^{-1} s^{-1} for *k*+ and s^{-1} for *k*-. **(B)** Hydrolysis of ATP bound to each subunit is fast with half time 2 seconds. **(C)** Dissociation of the phosphate is very slow with half time 6 minutes.

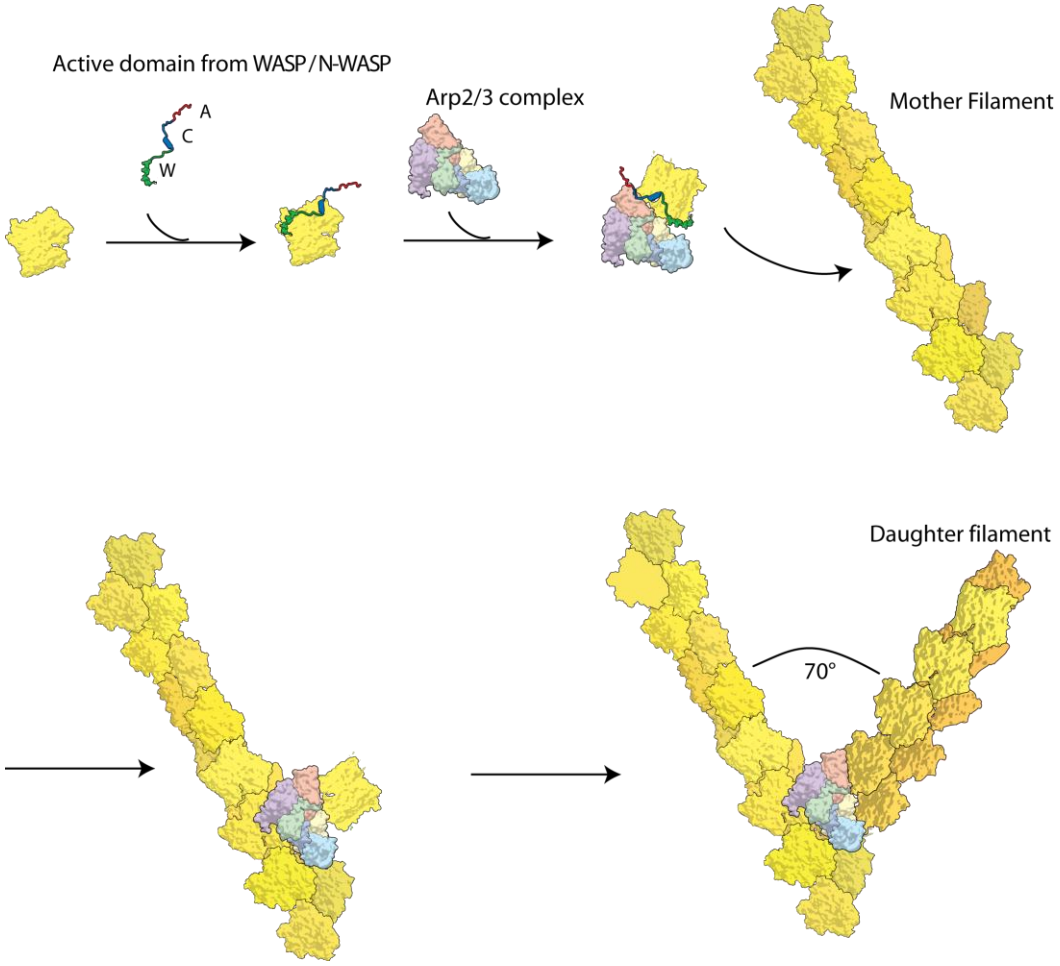

Figure 1.2. Arp2/3 complex mediated actin nucleation.

Nucleation Promoting Factor (NPF) such as Wasp and N-Wasp binds to actin monomer and Arp2/3 complex. The ternary structure binds to the side of mother filament and completes activation. The barbed end of daughter filament nucleates from Arp2/3 complex.

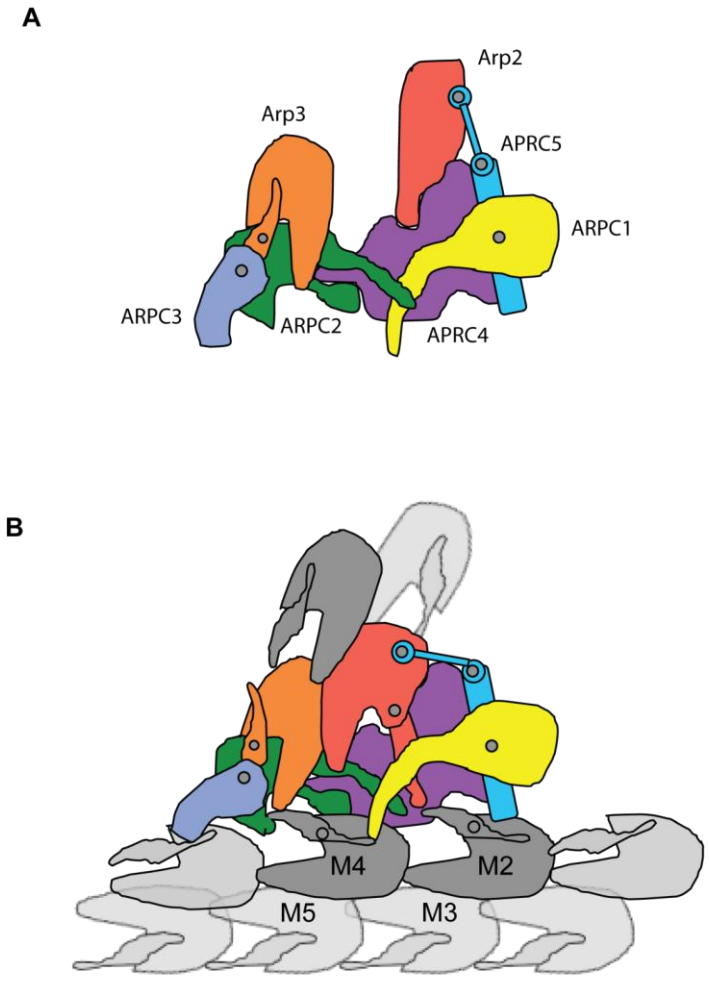

Figure 1.3. Structure of Arp2/3 complex.

(A) Drawing of inactive Arp2/3 complex. **(B)** Drawing of active Arp2/3 complex with Arp2 and Arp3 arranged like two subunits along the short-pitch helix of an actin filament.

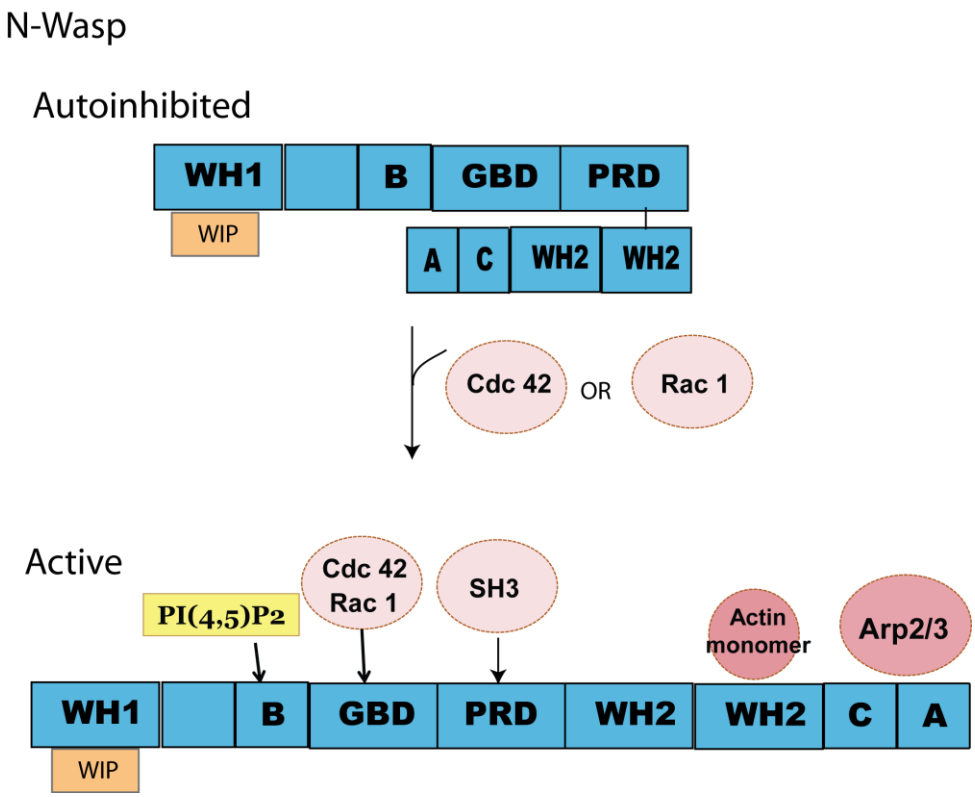

Figure 1.4. N-WASP, a Nucleation Promoting Factor (NPF).

N-WASP are modular proteins that contain an N-terminal WASP homology 1 domain (*WH1*), a basic region (*B*), a GTPase binding domain (*GBD*), a proline-rich domain (*PRD*), and a C-terminal catalytic domain (*WWCA*) composed of two WASP homology 2 domain (*WH2, or W, or V*), a connector region (*C*), and an acidic domain (*A*). WASP contains only one WH2 domain (not shown). N-WASP is auto-inhibited by intramolecular binding of the WWCA domain to the B/GBD domains. The binding of WIP (WASP interacting protein) to the WH1 domain of WASP and N-WASP maintains this inactive state. A variety of ligands synergistically activates WASP and N-WASP by disrupting the intramolecular interaction and exposes the COOH-terminal domain that binds and activates the Arp2/3 complex.

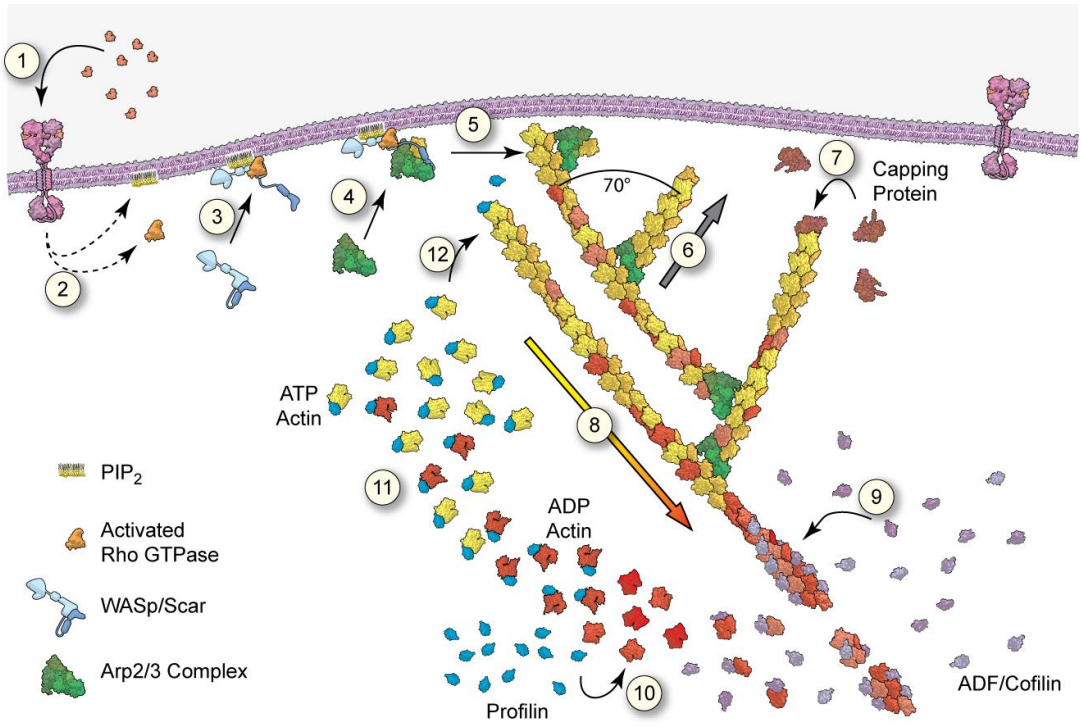

Figure 1.5. Dendritic nucleation model for actin assembly of the leading edge.

(1) An extracellular signal induces (2) activation of intracellular second messengers which (3) turn on nucleation promotion factors (NPFs) bringing them to the cell membrane. (4) WASp/Scar proteins bring together Arp2/3 complex and an actin monomer on the side of a preexisting filament (5) to form a branch. (6) Rapid growth at the barbed end of the new branch pushes the membrane forward. (7) Capping protein rapidly terminates growth. (8) Filaments age by hydrolysis of ATP bound to each actin subunit (white subunits turn yellow) followed by dissociation of the γ phosphate (subunits turn red). (9) ADF/cofilin promotes phosphate dissociation, severs ADP-actin filaments and promotes dissociation of ADP-actin from filament ADP ends. (10) Profilin catalyzes the exchange of ADP for ATP (turning the subunits white),

returning subunits to (11) the pool of ATP-actin bound to profilin, ready to(12) elongate barbed ends as they become available.

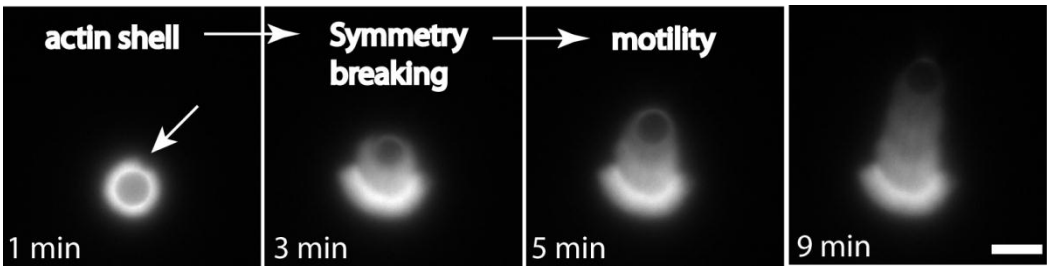

Figure 1.6. Reconstitution of actin-based motility of functionalized particles.

GST tagged N-WASP WWCA coated polystyrene bead (4.5 μm in diameter) generates actin tail and undergoes propulsion in the medium containing Arp2/3 complex, capping protein, profilin, and actin. To establish the motility, actin polymerized evenly at the bead surface to form actin shell. A breakage in actin shell (*white arrow*) induces symmetry breaking. After symmetry breaking, actin filaments polymerize at only one side of the bead and propel the directional movement. Scale bar, 5 μm

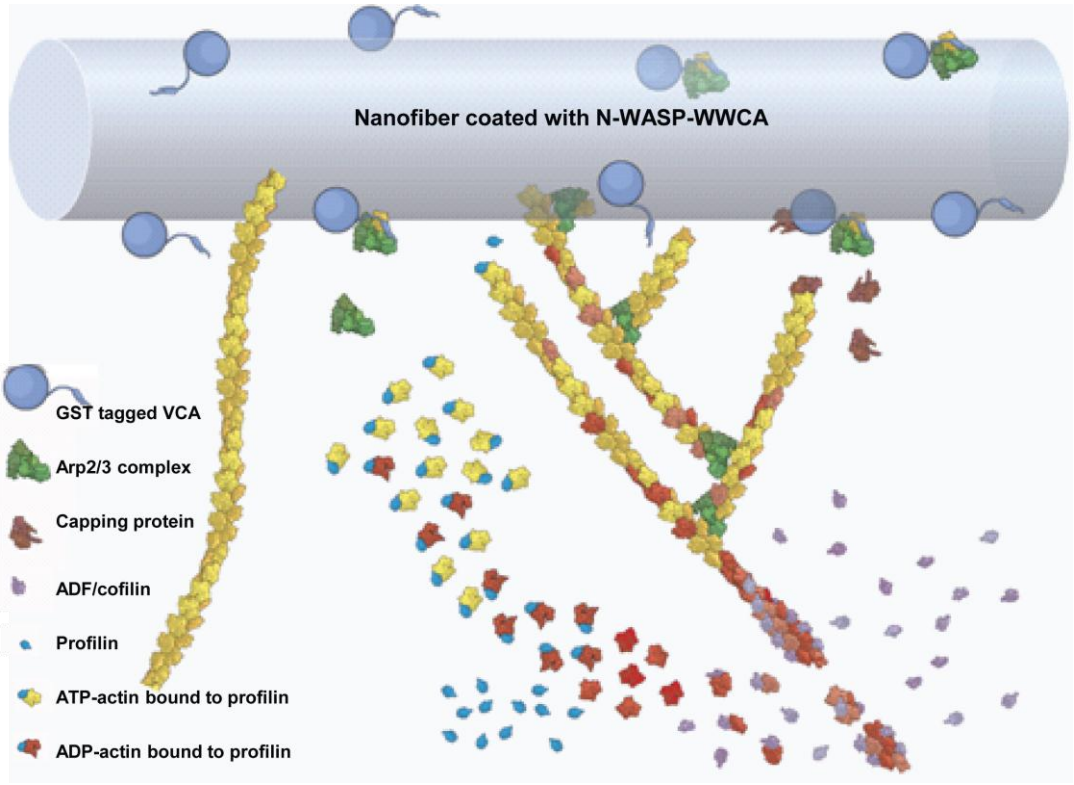

Figure 1.7. Reconstitution of actin-based motility of nanofiber.

Nanofibers with diameter of 200nm - 700 nm were coated with GST tagged N-WASP WWCA. Arp2/3 complex, profilin and capping protein and actin were included in a minimum motility medium.

Chapter 2 Actin filament attachments for sustained motility *in vitro* are maintained by filament bundling.

Xiaohua Hu and Jeffrey R. Kuhn

PLoS One, 2012 Feb 16; 7(2): e31385.

Abstract

We reconstructed cellular motility *in vitro* from individual proteins to investigate how actin filaments are organized at the leading edge. Using total internal reflection fluorescence microscopy of actin filaments, we tested how profilin, Arp2/3, and capping protein (CP) function together to propel thin glass nanofibers or beads coated with N-WASP WCA domains. Thin nanofibers produced wide comet tails that showed more structural variation in actin filament organization than did bead substrates. During sustained motility, physiological concentrations of Mg^{2+} generated actin filament bundles that processively attached to the nanofiber. Reduction of total Mg^{2+} abolished particle motility and actin attachment to the particle surface without affecting actin polymerization, Arp2/3 nucleation, or filament capping. Analysis of similar motility of microspheres showed that loss of filament bundling did not affect actin shell formation or symmetry breaking but eliminated sustained attachments between the comet tail and the particle surface. Addition of Mg^{2+}, Lys-Lys^{2+}, or fascin restored both comet tail attachment and sustained particle motility in low Mg^{2+} buffers. TIRF microscopic analysis of filaments captured by WCA-coated beads in the absence of Arp2/3, profilin, and CP showed that filament bundling by polycation or fascin addition increased barbed end capture by WCA domains. We propose a model in which CP directs barbed ends toward the leading edge and polycation-induced filament bundling sustains processive barbed end attachment to the leading edge.

Introduction

Actin-based cell motility plays a crucial role throughout the lifetime of organism. The front or leading edge of a typical crawling cell forms a broad, fan-like lamellipodial protrusion that contains a branching actin filament network generated by the Arp2/3 complex [9, 88]. In the dendritic nucleation model of actin-based cell motility [89, 90], binding of nucleation promoting factors (NPFs), such as WASP and WAVE family proteins to the leading edge membrane exposes their active C-terminal WCA domains. Exposed WCA domains bind to an actin monomer and to the Arp2/3 complex to form a complex that binds to the side of an existing filament to generate a new, rapidly-polymerizing filament with its barbed end directed towards the membrane. The combined force of many growing actin filament barbed ends push the cell membrane outwards until each filament's growth is halted by barbed end capping protein (CP), which keeps actin filaments short and stiff. ATP-actin filaments are slowly hydrolyzed to ADP, providing a natural timing mechanism that delineates filament age and distance from the advancing membrane. Cofilin binds to and severs older ADP-actin filaments some distance away from the leading edge, and the severed oligomers rapidly depolymerize into ADP-actin monomers. Profilin replaces cofilin on actin monomers and promotes actin nucleotide exchange to provide a fresh pool of ATP-actin for filament polymerization. Profilin also suppresses *de novo* actin nucleation. In vitro these proteins are sufficient to reconstitute sustained, actin-based motility [13].

Much of the current understanding of dendritic nucleation dynamics comes from studies of *in vitro* reconstitution of actin-based motility. The pathogenic bacteria *Listeria monocytogenes* [70, 91, 92] and *Shigella flexneri* [72, 73, 93], which spread in the host body by subverting the host cell's actin motility machinery [94]. Each bacterium species expresses a single surface NPF,

ActA for *Listeria* [12, 71] or IscA for *Shigella* [72, 73], which activates the cellular Arp2/3 complex to form a shell of polymerizing actin. The actin shell eventually breaks symmetry [95-98] to form a branched, propulsive "comet tail" of polymerizing actin that is structurally similar to a lamellipodia [99].

Exogenous NFPs are sufficient to effect actin-based motility in cellular cytoplasmic extracts [73, 100] or in a suite of purified proteins [13]. Thus, bacteria can be substituted with microspheres [16, 98, 101], micro-discs [102], lipid droplets [103], vesicles [104], or lipid-coated particles [105, 106] that are coated with either bacterial or eukaryotic cellular NPFs such as WASP or WAVE family proteins [16, 77, 106] to study actin-based motility either in cell extracts or purified proteins.

The majority of barbed ends within a comet tail are directed toward the particle surface. How then does this filament network remain attached to the particle surface as it grows? Distortions of NPF coated lipid vesicles or droplets from round to teardrop shape show that some actin filaments must transiently attach to the particle to provide a pulling force that apposes the pushing force generated by growing barbed ends. The theoretic "tethered ratchet" model of Mogilner and Oster [107, 108] and closely related "cooperative thermal breakage" models [109, 110] predict that a subset of non-polymerizing actin barbed ends are transiently attached to the leading edge while other barbed ends push against the leading edge. The transient links are broken as the compressive force of polymerization against the barrier is translated through the crosslinked network to the attached ends. The WH2 (W) domain of the cellular NPF, WASP can bind both to actin monomers [111] and the terminal subunit at the barbed end of an actin filament [112-114] and thus may provide this linkage. While some studies have shown that WH2 domains at the particle surface bind independently of the Arp2/3 complex [75], others have

indirectly shown that WH2 domains maintain their attachment to filaments primarily through Arp2/3 [106] with direct WH2 to barbed end attachments playing a secondary role in a cycle of attachment, release, and elongation. While WASP likely plays roles in both maintaining comet tail attachment to the leading edge and in transiently maintaining barbed end orientation, both the mechanism and the role of Arp2/3 in this process remains unresolved.

In contrast to the tethered ratchet model, the "actoclampin" model of Dickinson and Purich [97, 115, 116] presumes that the particle surface remains processively bound to growing actin barbed ends. While processive barbed end binding has been shown for VASP [117] and formins [118], no evidence has been provided for processive attachment of WASP or WAVE proteins to barbed ends. A positively charged Arg at the N-terminus of WASP's WH2 domain alpha helix sits at the longitudinal binding region between actin subdomains 1 and 3 [114], presumably blocking further barbed end addition. However, consecutive WH2 domains such as those in N-WASP have been shown to bind longitudinal actin dimers [112]. Thus, individual WH2 domains might bind to the side of filaments without steric inhibition of barbed end addition. Though WASP may not block elongation, WASP is a monomer while processive barbed end binding proteins such as formin and VASP are multimers. Multimeric actin binding proteins can have both bound and unbound subunits within the same multimer. Because WH2 domains at the leading edge are monomeric, it is unclear how a single WH2 domain could remain processively attached to a growing barbed end after dissociating.

Bundling of barbed ends could provide the multimerization required for processive attachment to WH2 domains. In support, several lines of evidence point to a role of actin bundling in comet motility. In an early study, melanoma cells lacking expression of the bundling protein ABP280/filament did not migrate or produce lamellipodia compared to ABP280

expressing melanoma cells [119]. Direct perturbation of actin-fascin binding completely prevented C2C12 myoblast spreading and migration on thrombospondin-1 and partially blocked migration of fibronectin [120]. In support of the role of bundling in motility, several *in vitro* reconstitution experiments have shown that addition of filament bundling proteins increases particle propulsion rates [77, 78, 80]. Addition of filament bundling proteins α-actinin [13], T-plastin [77], or fascin [78] to a standard *in vitro* motility assay increases the propulsion velocity of tethered beads or bacteria. Once filaments are nucleated with barbed ends facing the particle, Arp2/3 appears to be dispensable to propulsion. Brieher *et al* [78] showed that Lysteria expressing ActA on their surfaces were rapidly propelled through cytoplasmic extract by fascin-bundled filaments, even after an Arp2/3 inhibitor was added. However, the relative contribution that filament bundling plays in an Arp2/3 generated network have not been resolved.

We have used total internal reflection fluorescence (TIRF) microscopy [121, 122] and a modified *in vitro* motility assay to explore actin filament dynamics and the role of filament bundling in comet tail formation and maintenance. Thin glass nanofibers coated with WCA domains in motility buffers produced actin comet tails that propelled the particle yet were thin enough for observation of filament geometry in the comet tail. We found prominent filament bundles within the comet tail. The degree of bundle formation was controlled by CP concentration. These bundles grew faster than the surrounding dendritic actin network. Processive attachment of these fast-growing, bundled barbed ends to the particle surface often generated prominent bending and buckling of the bundle. Reduction of buffer Mg^{2+} to levels that prevented bundling without affecting actin polymerization or Arp2/3 nucleation abolished motility by eliminating comet tail formation but not shell formation or symmetry breaking. In parallel experiments with microspheres, this reduction of both persistent comet tail attachment

and elongation could be rescued by addition of either excess Mg^{2+} or lys-lys^{2+}. Addition of the actin bundling protein fascin rescued both comet tail attachment and elongation in low Mg^{2+}, but fascin supported slower motility than did additional divalent cation. Both divalent cations and fascin promoted the direct attachment of bundled barbed ends to tethered WCA domains in a concentration dependent manner and independently of Arp2/3. We propose a model in which filament bundling allows barbed ends to cooperate for semi-processive attachment to WCA domains at the leading edge and thus help maintain the orientation of growing barbed ends at the comet tail-particle interface.

Material and Methods

Protein expression, purification, and fluorescent labeling. Actin was purified from rabbit skeletal muscle acetone powder through one round of polymerization, depolymerization, and gel filtration [123]. Actin was labeled with pyrenyl iodoacetamide (Invitrogen, Carlsbad, CA) [124] or with Oregon green 488 iodoacetamide (Invitrogen) as previously described [122]. Before use, labeled and unlabeled actins were dialyzed overnight against fresh buffer G (2 mM Tris-Cl pH 8, 0.2 mM ATP, 1 mM NaN_3, 0.1 mM $CaCl_2$, 0.5 mM dithiothreitol, DTT) and centrifuged at 100,000 g for 2 hr at 4 ℃. Arp2/3 complex was purified from bovine thymus as described [125]. Recombinant mouse capping protein was expressed in *E. Coli* and purified as described [126]. Human N-WASP-WCA was expressed as GST fusion proteins in *E. Coli* and purified on a Glutathione Agarose affinity column (Thermo Scientific, Rockford, IL) followed by anion exchange chromatography on a Source Q (GE Healthcare, Piscataway, NJ) column [111]. Recombinant human profilin I was expressed in *E. Coli* and purified by poly-L-proline affinity chromatography as described [127]. Recombinant human fascin I was expressed in *E. Coli* and

purified and cleaved as described [128]. Actin and labeled actins were stored for 1 month at 4 ℃. All other proteins were flash frozen in liquid nitrogen and stored at -80 ℃.

Nanofiber and bead preparation. Nanofibers (200 nm nominal diameter, Johns Mansville, Denver, CO) were separated in chloroform with a Dounce homogenizer, centrifuged at 3750 rpm for 15 min in a clinical centrifuge, and the chloroform was evaporated in a fume hood. Nanofibers were washed once with deionized water by centrifugation and sonicated for 1 hour in 1M KOH in a bath sonicator to remove contaminants. Nanofibers were washed briefly in deionized water, resuspended in 1 M HCl, sonicated for 1 hour, and incubated overnight in HCl. Cleaned nanofibers were subsequently pelleted by centrifugation and sonicated for 30 minutes each in in ddH_2O, 1 mM EDTA, 70% ethanol, and absolute ethanol to dry, with pelleting between each step. Cleaned nanofibers were stored in glass containers in absolute ethanol for up to three months.

Carboylated polystyrene 4.5 μm diameter microsphere (Polysciences, Warrington, PA) or glass nanofiber were coated respectively with 8.5 uM or 10 uM GST tagged WCA by incubation for 1h at room temperature. Particles were pelleted by low speed centrifugation and resuspended in storage buffer (10 mM HEPES pH 7.8, 0.1 mM KCl, 1 mM $MgCl_2$, 1 mM ATP, 0.1 mM $CaCl_2$, 0.01% NaN_3) containing 1 mg/ml bovine serum albumin (BSA, Sigma-Aldrich, St. Louis, MO) to block subsequent nonspecific binding. Particles were stored at 4 ℃ for up to 1 week.

Reconstitution of nanofiber and bead motility under TIRF microscopy. Glass slides and coverslips were cleaned, and flow cells constructed as previously described [122]. For buffer exchange, flow cells were coated with 300 nM n-ethylmaleimide inactivated myosin II for 2 minutes. For all experiments, flow cells were coated with 1% BSA for 5-7 min as described [122]. After blocking, 16 μl of reaction mixture was wicked through the chamber and the

chamber was either sealed with warm VALAP (1:1:1 vaseline/ lanolin/paraffin) or left unsealed for subsequent buffer exchange. For bead motility assays, glass slides and coverslips were blocked overnight in 1% BSA at 4 ℃ and dried in air before use. We placed 16 µl of reaction mixture on a BSA coated slide, covered with a BSA coated coverslip, and sealed the chamber with VALAP.

Labeled and unlabeled Ca-ATP actin were diluted to the desired labeled fraction, mixed 9:1 with 10x magnesium exchange buffer (10x ME: 10 mM EGTA, 1 mM $MgCl_2$) and incubated on ice for 2 minutes to form 4x final concentrations of Mg-ATP actin. We placed 8 µl of Mg-ATP actin at the bottom of a 1.5 ml Eppendorf tube and added 7 µl of motility protein mixtures and 1 µl of coated nanofibers or beads on the side of the tube. We washed both drops together with 16 µl 2x TIRF buffer (2x: 100 mM KCl, 2 mM $MgCl_2$, 2 mM EGTA, 20 mM imidazole, pH 7.0, 200 mM DTT, 0.4 mM ATP, 30 mM glucose, 0.5% 1500 cP methylcellulose, 40 µg/ml catalase, 200 ug/ml glucose oxidase) and placed the reaction mixture in either a flow cell or slide-coverslip as described above.

Image acquisition and processing. Actin fluorescence was observed with a 60x 1.49 NA TIRF objective on an Olympus IX2 inverted microscope. Images were captured with a Retiga EXi cooled CCD camera (QImaging) using SlideBook image acquisition software (Intelligent Imaging Innovations, Inc). All subsequent image-processing steps were performed in ImageJ, available at http://rsbweb.nih.gov/ij. TIRF microscopy images were gamma corrected using a value of between 0.5 and 0.8. An Unsharp Mask filter was applied with a radius of 1 to 1.3 pixels and a 60% mask weight. Widefield fluorescence microscopy images were unprocessed. For DIC images, each image was divided by an averaged background image and contrast was adjusted to locate the nanofiber. Images were rotated and cropped for publication.

Bead motility in low magnesium. For low Mg^{2+} motility buffers, we made the following changes: (1) For each experiment, we diluted fresh Ca-ATP actin into buffer G with no added Ca^{2+}. (2) We mixed actin 9:1 with 10x low magnesium exchange buffer (10x lowME: 2 mM EGTA, 0.2 mM $MgCl_2$) for 2 minutes to form 4x final concentration of actin. (3) We diluted all proteins in buffer G with no added Ca^{2+}, or Mg^{2+}, or EGTA. (4) We reduced $MgCl_2$ in 2x TIRF buffer from 2 mM to 0.2 mM to form 2x low-ME TIRF buffer. The final total concentration of Mg^{2+}, Ca^{2+}, EGTA, and ATP were 0.105 mM, 5 μM, 1.05 mM, and 0.2 mM, respectively. Free Mg2+, Ca2+, and ATP concentrations were calculated using MaxChelator software [129, 130] available from maxchelator.stanford.edu.

Filaments binding to microspheres. Coverslips were coated with 1 mg/ml poly-L-lysine (30 to 70 kDa, Sigma-Aldrich) for 2 minutes, rinsed 3x with deionized water, and dried in air. We polymerized 8 μM (30% Oregon green labeled) Mg-ATP actin in buffer F (buffer G with 10 mM Imidazole pH 7, 50 mM KCl, 0.15 mM $MgCl_2$, 2 mM EGTA) for 10 minutes at room temperature. Actin seeds were diluted 3-fold in buffer F and vortexed at maximum speed for 1 minute to break filaments. To prepared seeds, we added 4.5 μm diameter GST-WCA coated microspheres, 1 μM Oregon green labeled Mg-ATP actin monomers, and 1 mg/ml BSA. Mg^{2+}, Lys-Lys^{2+}, fascin or K^+ were also added at this step. The reaction was incubated for 10 minutes at room temperature, beads and bound filaments and bundles were pelleted by centrifugation at 5000 rpm for 1 min, and the supernatant was removed. The pellet containing beads and bound filaments was gently diluted 16-fold in buffer F, mixed 1:1 with 2x TIRF buffer in the absence of methylcellulose, and 16 μl was added to a poly-L-lysine coated coverslip. Filaments/bundles and beads were observed, respectively, by TIRF or DIC microscopy.

Bulk pyrene-actin spectroscopy assays. For actin and profilin-actin experiments, we diluted labeled and unlabeled Ca-ATP actin to 30% labeled fraction with or without added profilin, mixed 9:1 with 10x low-Mg exchange buffer, and incubated on ice for 2 minutes to form 2x final concentrations of Mg-ATP actin in the lower row (preparatory wells) of a 96 well half area flat bottom plate (Corning). Various concentrations of $MgCl_2$ were placed in the upper row (reaction wells) of the same plate along with 1.6 µl of 100x antifoam (100x: 0.005% antifoam-204, Sigma-Aldrich), 2x initial concentration of low-Mg KMEI (10x: 500 mM KCl, 1 mM $MgCl_2$, 10 mM EGTA, 100 mM Imidazole, pH 7), and buffer G without added Ca^{2+}. We started the reaction by transferring 80 µl of actin mixture from the lower preparatory row the upper reaction row containing 80 µl in each well for a 160 µl total reaction. The reaction was gently mixed with a 12-channel pipette, and pyrene-actin fluorescence was measured in a Spectra MAX Gemini XPS fluorescent plate reader (Molecular Devices, Sunnyvale, CA) with excitation and emission wavelengths of 364 nm and 407 nm, respectively. Arp2/3 nucleation experiments were similarly performed with Arp2/3 and GST-WCA added to the reaction well prior to the reaction start. For capping protein activity assays, we added CP to the reaction well followed by short (vortexed) unlabeled actin filament seeds prior to the reaction start as previously described [61].

Results

Actin architecture in moving nanofibers.

We coated thin glass nanofibers with GST-tagged WCA domains (GST-WCA) from N-WASP and observed formation of individual actin filaments with TIRF microscopy in the presence of profilin-actin, Arp2/3, and CP. We excluded cofilin, VASP, and actin bundling proteins from these experiments to understand how a minimal set of proteins direct filament organization in moving nanofibers. Although cofilin is an important player in dendritic

nucleation, cofilin acts downstream of the dendritic nucleation pathway. For *in vitro* motility assays, cofilin increases propulsion rates in long-term studies by maintaining an actin monomer pool [59]. We therefore restricted our initial observations to the first 60 to 90 minutes of comet tail formation. Experiments with and without cofilin showed little difference in particle velocities in similar motility buffers for these short-term observations (**Table I**).

In well-blocked flow-cells, nanofibers rarely adhered to the top surface but fell to the chamber bottom. We thus required a TIRF microscope with evanescent excitation at the chamber bottom to observe moving nanofibers. In contrast, previous prism-based TIRF microscopy observations of actin comet tails generated NPF-coated glass nanofibers [131] were restricted to nanofibers permanently affixed to the chamber top. Consequently, these experiments were limited to observations of actin architecture during branch initiation and not during sustained nanofiber motility.

Actin shells formed around nanofibers in motility buffer at actin concentrations of 8.5 μM and a CP to Arp2/3 ratio of 0.75 to 2, often before the nanofiber drifted to the chamber bottom and into the TIRF microscopy excitation field. After initial shell formation, the nanofibers usually broke symmetry to form either one or two comet tails. Though 68% of observed nanofiber initially formed one comet tail of polymerizing actin, 33% initially formed two comet tails, one on either side of the nanofiber axis (**Figure 2.1**F). In the latter case, one tail usually attained dominance and the residual tail was left behind near the original shell as the nanofiber moved (**Figure 2.1**B). In rare cases, two tails persisted on either side of the nanofiber, and the nanofiber remained relatively stationary while the tails were pushed away from the nanofiber by new filament growth at the nanofiber surface (**Figure 2.1**G). For both single and double comet tails, the majority of new filament growth appeared at the nanofiber surface, while the network

within the comet tail either remained stationary or was pushed rearward at a slow rate. Thus, the majority of barbed end growth was directed toward rather than away from the nanofiber surface, consistent with dendritic nucleation.

Nanofibers with single tails moved at 0.14 μm/min at an optimal CP to Arp2/3 ratio of 1.0 and slightly slower at a CP to Arp2/3 ratio of 2.0 (**Table I**). These speeds were substantially slower than previous reports of 2.2 μm/min movement of spherical particles in similar buffers lacking cofilin[59]. Much of this difference could be attributed to our use of muscle actin, which produced 4-fold slower particle speeds than did cytoplasmic actin [59]. In support, we found that 4.5 μm diameter spherical particles moved at 0.48 μm/min in the same motility buffers used for nanofibers (**Table I**). These rates were comparable to previous studies in which similarly sized beads moved at 0.5 μm/min in similar motility buffers containing muscle actin [132]. Thus, the 4-fold difference between nanofiber and bead speeds in our motility buffers was due to particle geometry, and likely attributable to the thin but wide comet tails generated by 200 nm thick nanofibers.

Capping Protein controls the transition between bundled or branched actin networks.

Previous studies showed that actin filaments can form from dendritically nucleated networks *in vitro* and that CP can control the proportion of branched to bundled filaments [133, 134]. However, filament barbed ends in these studies grew away from the particle surface and bundling did not result in particle motility. We found that comet tails with barbed ends directed toward WCA-coated nanofibers also contained two populations of actin filaments. Under TIF microscopy, bundled filaments resembling microspikes primarily formed perpendicular to the direction of movement within a dendritic network of highly branched filaments. In contrast, these bundles were invisible under widefield microscopy (**Figure 2.1**D). The variance in actin

network architecture between bundled and branched filaments persisted as comet tails grew at the nanofiber interface. The dominance of these two structures in comet tails changed with different concentration of CP. Actin filament bundles were more prominent at lower CP concentration (100 nM) (**Figure 2.1**A) while branched filaments dominated at higher CP concentration (200 nM) (**Figure 2.1**B).

Actin branches and bundles were inter-convertible. Although comet tail formation was rare at lower actin concentrations of 2 μM, the origins of bundles and branches were more easily discerned in the few, sparse comet tails that formed. Here, individual filaments converged to form brighter bundles (**Figure 2.1**E *left panel*) and bundles could sometimes be seen to dissociate into individual daughter filaments emerging from the same mother filament (**Figure 2.1**E *right panel*).

Bundles terminate at the nanofiber surface.

At low (≤ 75 nM) CP concentrations, actin filament bundles frequently projected beyond the nanofiber surface as they elongated (not shown). In higher CP (≥ 100 nM), the majority of bundles continuously terminated at the nanofiber as they grew (**Figure 2.13**A-C *black arrowheads*). In contrast to bundles, individual actin filaments within the comet tail often elongated across and beyond the nanofiber surface, even at higher CP concentrations (**Figure 2.13**A, C *arrows*).

Bundles elongated faster than the surrounding comet tail, consistent with previous studies in which filament bundling proteins increased motility speeds [13, 77, 78]. For example, four bundles from Figures **2.2**A-B elongated at 0.22 ± 0.05 μm/min, while the overall comet tails expanded at 0.09 ± 0.01 μm/min. Faster bundle elongation often resulted in bending or buckling

of the bundle between the fast growing barbed ends at the nanofiber surface and the pointed ends embedded within the dendritic network (Figure **2.2**A, B *arrowheads*).

Processive or semi-processive attachment between growing bundled barbed ends and the nanofiber surface was further illustrated by the reduction of CP concentration through an exchange of motility buffer on an existing comet tail (Figure **2.2**C). Here, short bundles present before the buffer exchange (top panels) elongated substantially after CP concentration was reduced (bottom panels). Processive attachment of bundled barbed ends to the nanofiber surface coupled with their faster growth rates (2.4 μm/min) resulted in significant looping of these bundled filaments. We observed similar buckling and looping of bundles on moving nanofibers (not shown). At low (≤ 75 nM) CP concentrations, 27% nanofibers (n=37) were observed with buckling and looping of filament bundles. Thus, bundled barbed ends were not physically trapped by strong attachments between the nanofiber and the chamber surface, but were likely attached through specific molecular interactions with GST-WCA at the nanofiber surface.

As bundled loops grew, they split into individual filaments of varied lengths. Measurement of individual filament growth rates from several bundles showed that filaments within a bundle grew in a salutatory fashion (Figure **2.2**D-G), indicating that capping times varied between individual barbed ends within the bundle.

Cellular levels of magnesium generate actin bundles *in vitro*.

Actin bundles or microspikes form at the leading edge of motile cells *in vivo* [135] and bead-based *in vitro* motility experiments have shown that actin bundles generate more propulsive force than individual branched filaments [13, 77, 78]. Our *in vitro* experiments indicated that actin filament bundles were prevalent even in the absence of specific actin crosslinking or

bundling proteins in our motility buffers. We therefore sought to eliminate bundles to determine the relative contributions of dendritic and bundled filaments to particle motility.

Both the methylcellulose used in most in vitro TIRF microscopy assays of actin dynamics [136, 137] and polyvalent cations such as Mg^{2+} [138] can bundle filaments. However, the mechanism of bundle formation by these two solutes differs substantially [139]. Methylcellulose contributes to bundle formation through entropic depletion forces that reduce effective solution volume. Polycations overcome the 14 e^{-}/subunit negative charge of filamentous actin to promote filament side-to-side association.

One study of the concentration dependence of methylcellulose on bundling [140] found that filaments start to bundle in high viscosity methylcellulose (88 kDa, 4000 cPs at 2%) at a threshold concentration of 0.2%. Similar studies with polyethylene glycol showed that the filament bundling threshold also depends upon the chain length of the excluding solute [141, 142]. Although we used 0.25% methylcellulose in our TIRF microscopic assays to stabilize actin filaments for imaging, we used a lower viscosity species (63 kDa, 1500 cPs at 2%). Thus, the contribution of methylcellulose to bundling was unclear but likely near the threshold concentration.

Actin paracrystals formation requires Mg^{2+} concentrations of $\geq$ 10 mM [138], but several studies have reported anecdotal evidence that bundles form at the 1 mM Mg^{2+} concentrations used in typical TIRF actin microscopy and *in vitro* motility buffers once filament densities increase [143-145]. We therefore sought Mg^{2+} concentrations that would eliminate filament bundling in the presence of minimal, 0.25% of 63 kDa methylcellulose.

In typical actin polymerization assays, the Ca^{2+} bound to the high affinity Mg^{2+} site on actin is first exchanged with Mg^{2+} by addition of an excess of Mg-EGTA prior to addition of KCl. To

generate low Mg^{2+} conditions, we diluted Ca-ATP-actin monomers into buffer without added Ca^{2+} and reduced Mg-EGTA concentrations 5-fold during the exchange step. We correspondingly reduced ATP concentrations from 0.38 mM used above to 0.2 mM, a concentration sufficient for both actin polymerization and Arp2/3 nucleation. Total Mg^{2+} concentration in the assay was regulated by subsequent addition of $MgCl_2$. We calculated free Mg^{2+} concentration from the pH and total buffer $CaCl_2$, EGTA, $MgCl_2$, ATP, and KCl concentrations using existing methods [129, 130]. At standard 1 mM total Mg^{2+} concentration, filament bundles could be seen after 30 min of polymerization (Figure **2.3**). An increase in total Mg^{2+} to either 5 or 10 mM increased both the speed of bundle formation and thickness of bundles. Reduction of total Mg^{2+} to 0.5 mM (0.3 mM free) or below abolished bundle formation in the presence of 0.25% methylcellulose. As the typical cellular Mg^{2+} ranges from 0.5 to 1.5 mM [146-148], we expect that similar Mg-actin bundles form at the leading edge where filament density is high.

Reduction of Mg^{2+} below cellular levels abolishes motility.

Remarkably, lowering Mg^{2+} 10-fold to 0.1 mM total (0.03 mM free) completely abolished nanofiber motility (not shown). Restoration of Mg^{2+} to 1 mM total (0.7 mM free) with additional $MgCl_2$ restored nanofiber motility. While glass nanofibers provided a good model of a leading edge, they varied in length, diameter, and curvature. Thus, analysis of nanofiber motility speeds as a function of Mg^{2+} concentration could be substantially influenced by variations in nanofiber geometry. As an alternative to nanofibers, we used 4.5 μm diameter polystyrene microspheres to quantify the dependence of particle motility on Mg^{2+} concentration. We found that bead motility speeds also varied greatly with free Mg^{2+} concentration (Figure **2.4**A, C). Reduction of total

Mg^{2+} concentration to 0.5 mM (0.3 mM free) or below abolished comet tail growth from GST-WCA coated beads.

Restoration of total Mg^{2+} to cellular concentration level of 1 mM total (0.7 mM free) restored comet tail growth rates to 0.16 ± 0.07 μm/min (Figure **2.4**E). Additional of Mg^{2+} aboce 1 mM accelerated comet tail growth rates in a concentration-depended manner. For example, 10 mM total (9.4 mM free) Mg^{2+} accelerated comet tail growth rates to 0.59 ± 0.17 μm/min, an approximate 4-fold increase over the rate in 1 mM Mg^{2+}. Comet tail growth showed a similar dependence on Mg^{2+} in the absence of methylcellulose (Figure **2.4**E). These results indicate that cellular levels of Mg^{2+} are necessary for generating *in vitro* motility and that entropic depletion forces play little to no role in this requirement.

Actin binding proteins show little Mg^{2+} dependence.

Actin polymerization in KCl has been shown to be independent of excess magnesium [149]. We sought to test the possibility that Mg^{2+} was necessary for some aspect of *in vitro* motility other than actin filament bundling. We thus measured actin polymerization, Arp2/3 nucleation, and CP binding using bulk pyrene actin assembly assays in the same range of Mg^{2+} concentrations as our TIRF microscopy assays of bead motility (**Figure 2.12**). As expected, varying free Mg^{2+} concentrations over a 300-fold range had no effect on KCl induced actin polymerization or Arp2/3 nucleation. Polymerization of profilin-actin from capped filament seeds showed a slight Mg^{2+} dependent increase in apparent final filament concentration. However, the initial slope of polymerization, an indicator of concentration of free ends, decreased slightly with Mg^{2+} concentration, and CP was the least active in low Mg^{2+} concentrations that abolished bead motility. Thus, abolishment of motility in low Mg^{2+} and

restoration in high Mg^{2+} was not due to the effect of Mg^{2+} on individual components of the motility machinery.

Cofilin does not rescue polycation-dependent motility.

At high Mg^{2+} concentrations, comet tail elongation slowed over the course of each 140 min experiment (Figure **2.4**C-D). This decrease was likely due to a decrease in available ATP-actin monomers over time from their incorporation into filaments. To test whether this decrease in monomers influenced Mg-dependent comet tail formation, we added cofilin to the motility buffer to establish a steady state of free actin monomers (Figure **2.5**). Cofilin addition abolished the gradual decrease in comet tail elongation over time seen at high Mg^{2+} concentrations but did not restore motility in low Mg^{2+} buffers. As with motility in buffers lacking cofilin, addition of 0.7 mM or more free Mg^{2+} restored motility in the presence of cofilin. Average comet tail growth rates were slightly higher in cofilin than without, but growth rates showed approximately the same dependence on free Mg^{2+} with or without cofilin (Figure **2.5**C). Coupled with the formation of both primary and secondary actin shells around beads in low Mg^{2+} buffers (see below), the lack of comet tail formation in low Mg^{2+} buffers without cofilin was not due to a lack of polymerization competent actin monomers.

Di-lysine restores bead motility in sub-cellular concentration Mg^{2+} buffers.

Based on the above observations, we reasoned that if *in vitro* bead motility depends upon the actin bundling activity of Mg^{2+} and not its coordination of ATP hydrolysis, then other polycations that bundle filaments should restore bead motility in low Mg^{2+} buffers. Oligomers of lysine have been shown by light scattering to bundle actin filaments [138], with the extent of bundling dependent upon the number of lysine residues. To match the effects of Mg^{2+} on motility as closely as possible, we added millimolar concentrations of the divalent cation Lys-Lys^{2+} to

low (0.03 mM free) Mg^{2+} motility buffers. Because lys-lys^{2+} is too large to fit into the high-affinity ATP binding cleft, it would not affect Mg-ATPase activity of either Arp2/3 or actin.

Addition of 0.5 mM Lys-Lys^{2+} to low Mg^{2+} buffers did not restore bead motility, but addition of 1 to 10 mM Lys-Lys^{2+} restored bead motility in a concentration-depended manner (Figure **2.4**B). Although Lys-Lys^{2+} did not restore bead motility to the same extent as additional Mg^{2+} (Figure D-E), Lys-Lys^{2+} is a zwitterion at cellular pH and not a true divalent cation. We expect that the negative charge of the deprotonated carboxyl group of Lys-Lys^{2+} limited the extent of its bundling activity. In contrast, addition of 5, 10, or 15 mM of monovalent KCl did not restore bead motility in low Mg^{2+} buffers (Figure **2.4**E). Thus, restoration of bead motility by Lys-Lys^{2+} was not simply due to an increase in buffer osmolarity or ionic strength, and *in vitro* motility absolutely requires polyvalent cations such as physiological concentrations of Mg^{2+}.

Filament bundling by fascin restores processive motility.

To test if the dependence of *in vitro* motility polycations was due to actin bundling, we added the bundling protein fascin to low Mg^{2+} motility buffers and measured comet tail lengths generated by GST-WCA coated beads. In very low, 0.03 mM free Mg^{2+}, addition of 80 nM fascin optimally increased comet tail growth rates (Figure **2.4**F, H, **Figure 2.11**). Addition of 500 or 1000 nM fascin restored comet tail growth but to a lesser extent than did 80 nM fascin.

TIRF microscopic images of comet tails with added fascin (**Figure 2.11**) showed a subset of straight, bright filament bundles within the comet tail that persisted throughout the entire observation period. These rigid fascin bundles were consistent with fully coupled bending in which filaments are rigidly adhered by specific crosslinks [150]. In contrast, magnesium bundles were highly dynamic and curved (Figure **2.2**), consistent with decoupled bundle bending and non-specific polycation-mediated adhesion between actin filaments. Thus, the failure of fascin to

fully restore motility could be due to differences between fascin and magnesium bundle rigidity. In support, addition of fascin *in vitro* has been previously been shown to slow initial particle motility [151], although this effect could be due to a reduction Arp2/3 mediated branching [152].

To address different contributions of fascin- and magnesium-bundled filaments to motility, we increased the free Mg^{2+} to 0.3 mM, a concentration that did not support motility on its own (Figure **2.4**G-H, **Figure 2.11**). Addition of 80 nM fascin restored motility to the same extent as in 0.03 mM free Mg^{2+}, but addition of 500 or 1000 nM fascin restored motility to a greater extent than in the lower Mg^{2+} concentration. Although fascin did not restore motility to the same extent as did high Mg^{2+}, the difference in stiffness and persistence between fascin and magnesium bundles, coupled with competition between fascin and Mg^{2+} for inter-filament binding could explain the difference in comet tail elongation seen between fascin and high Mg^{2+}.

Filament bundling mediates sustained comet tail attachment.

Beads in low Mg^{2+} grew thick actin shells that eventually broke symmetry (Figure **2.4**A, bottom panel). However, the resulting nascent comet tails did not elongate but completely detached from the bead surface and floated away (Figure **2.6**A). Comet tail detachment was not due to a lack of polymerization competent actin or Arp2/3, as a secondary actin shell often formed on the bead surface after the primary shell detached (Figure **2.4**H and **2.6**B). We interpreted this comet tail detachment as a failure to establish rapid rebinding of barbed ends to WCA domain in moving particles in the absence filament bundling.

To test the dependence of attachment on bundling, we quantified the fraction of GST-WCA coated beads with attached actin shells or comet tails over time (Figure **2.6**C-E). Of the beads that initially formed actin shells in 0.03 mM Mg^{2+} buffers, these shells were eventually lost so that by 90 minutes only 15% of beads retained their primary shell and 55% of beads had formed

secondary shells. Additional of Mg^{2+} restored bead-actin attachment in a concentration dependent manner (Figure **2.6**C). Increased comet tail growth rate was correlated with increased comet tail attachment. Therefore, Mg^{2+} induced bundling was likely required to maintain comet tail attachment to WCA at the bead surface to sustain bead motility. Similarly, addition of lys-lys^{2+} (Figure **2.6**D) or fascin (Figure **2.6**E) also restored sustained attachment of comet tails to the bead surface in 0.03 mM free Mg^{2+} buffers in a concentration dependent manner. Restoration of attachment was most dramatic in 1 μM fascin, as 100% of beads retained their comet tails over 90 minutes of observation. Thus, filament bundling did not mediate actin shell formation but continued attachment between actin filaments and the bead surface once motility was established.

Bundling enhances barbed end binding to WH2 domains in the absence of Arp2/3 and CP

To better dissect the role of filament bundling played in barbed ends binding to leading edge, we captured pre-formed filaments by GST-WCA coated beads in the absence of profilin, Arp2/3, and CP. Fluorescent actin was polymerized in low Mg^{2+} buffer and sheared to increase the number of ends. Short filaments were then incubated for 10 minutes with GST-WCA coated beads, actin monomers in low Mg^{2+} buffer, and added Mg^{2+}, Lys-Lys^{2+}, or fascin. After the beads were separated by centrifugation, filaments captured along the bottom surface of the bead were imaged by TIRF microscopy (Figure **2.7**A). We scored filaments or bundles that terminated at the bead surface as captured barbed ends. Because the thickness of bundles was unknown, bundles were scored as two filament ends. Counts of total filament ends captured per bead (Figure **2.7**B) showed that additional Mg^{2+}, Lys-Lys^{2+}, or fascin increased barbed end capture by tethered GST-WCA. Among all three bundling factors, 1 μM fascin provided the highest number of captured barbed ends (27 ± 5 per bead), a 10-fold increase over the number of barbed ends

captured in 0.03 mM free Mg^{2+} (2.7 ± 1.2 per bead). Barbed end capture in low Mg^{2+} was only slightly higher than the number of filaments that coincidentally overlapped with control BSA coated beads (0.9 ± 0.2).

Increased barbed end capture by increased Mg^{2+} was not due to an increase in the number of filaments as the Mg^{2+} range used did not affect actin polymerization (**Figure 2.12**A), nor was increased capture due solely to increased ionic strength as additional KCl only minimally increased the number of captured ends. Further analysis of captured barbed ends (Figure **2.7**C) showed that the number of single filaments captured did not vary substantially across all conditions. Beads captured from 2 to 1 individual filaments with increasing concentrations of Mg^{2+} or Lys-Lys^{2+} and from 2.5 to 0.7 individual filaments with increasing fascin. Rather, the increase in captured barbed ends resulted from a substantial increase in the number of captured bundles. Thus, capture of barbed ends by tethered WCA domains was largely due to filament bundling and WCA binding did not require Arp2/3 or CP.

Discussion

We used TIRF microscopy to observe the generation and maintenance of actin filament architecture in an *in vitro* motility system that utilized thin glass nanofibers as an analog for the leading-edge membrane of a motile cell. Our assay differed from previous TIRF observations of nanofiber-supported nucleation [131] in that our nanofibers moved within the TIRF excitation field rather than being immobilized. Thus, we were able to observe actin filament architecture during the later stages of sustained nanofiber motility after shell formation and symmetry breaking.

Our central finding was that filament bundling was essential for maintaining persistent attachments between growing barbed ends and N-WASP WCA domains on the moving particle.

Multiple lines of evidence support this claim. (1) Bundles form within the dendritic network in the absence of bundling proteins. While entropic depletion forces contribute to bundling, bundling is primarily due to cellular concentrations of the polyvalent cation, Mg^{2+}. (2) CP antagonizes bundle length, but short bundles are still generated within the comet tail even at high CP concentrations. (3) Like branched filaments, bundled barbed ends face the particle surface and can bind to WCA domains independently of Arp2/3. In moving nanofibers, these barbed end attachments are pseudo-processive and provide enough force to cause significant buckling of short bundles or looping of longer bundles. (4) Although filament bundling does not affect actin shell formation or symmetry breaking, bundling is required to maintain continued attachments between the growing comet tail and the particle surface. (5) WCA-tethered bundles elongate faster than the surrounding dendritic network, suggesting that WCA binding to bundled barbed ends antagonizes CP binding.

It is not surprising that bundles form in the absence of bundling proteins. In published ultrastructure studies of dense actin branched actin in motile cells [10, 153], the leading edge contains a wealth of short, parallel actin filaments consistent with polycation-mediated bundles. Although many of the longer bundles are generated by VASP, VASP remains at the elongating bundle tip and fascin recruitment to the bundle is delayed [154]. Polycations-mediated bundling could serve as the bridge between initial bundle formation and bundle stabilization by specific bundling proteins. We propose that filament densities at the leading edge are high enough that filaments likely form initial bundles when cellular Mg^{2+} concentrations exceed 0.5 mM. Other cellular polycations such as spermine may further promote short filament side-to-side association typically seen in nascent filopodia or microspikes. Thus, multivalent cation-induced filament

bundling in the absence of specific bundling proteins may be more important to dendritic nucleation than previously thought.

How might actin bundling promote processive barbed end attachment to monomeric WH2 domains at the leading edge? Both formin dimers [118, 155] and VASP tetramers [117, 156] can remain processively attached to growing barbed ends. Although WASP family proteins are monomeric in solution, they are present at high concentrations at the leading edge membrane and multiple WCA domains from adjacent WASP family proteins could cooperate to attach to filament barbed ends (Figure **2.8**A). Bundling of filaments by divalent cations aids WCA binding to barbed ends at the leading edge (Figure **2.8**A). Bundling would switch barbed end WCA attachments from slow, "cooperative thermal breakage" attachments (Figure **2.8**B) found in branched networks [109, 110] to fast, processive attachments (Figure **2.8**A) to WCA domains. Dimerization of WASP/WAVE has been shown to greatly enhance it Arp2/3 activation activity [157, 158]. Similarly, dimerization of WASP/WAVE family WCA domains at the leading edge could act synergistically with filament bundling to enhance processive binding to barbed ends. In support, we note that our study used GST-tagged WCA, which has been shown to dimerize *in vitro* [158].

Although the affinity of WCA domains to the terminal actin monomer is weak (K_d of 0.6 μM [111]), bundled filament barbed ends could cooperate to maintain processive attachments to several nearby WCA domains at the nanofiber surface. As one barbed end binds to a WCA domain, sister barbed ends within the bundle would be free to elongate. Rapid transmission of compressive force from free barbed ends polymerizing against the barrier to WCA-attached barbed ends within the same bundle would accelerate their detachment. In this way, the filament

bundle could processively elongate and remain attached although individual ends would be free to attach and detach from WCA domains during polymerization.

Like VASP, cooperative enhancement of the apparent WCA-barbed end affinity might also allow several nearby WCA domains to compete with the high affinity binding of CP to barbed ends (K_d of ~0.1 nM [159]), either by delaying CP association or accelerating CP dissociation at the nanofiber surface. Decreased CP activity near the NPF-coated surface would bias productive barbed end elongation towards the surface, while nonproductive Arp2/3 nucleated barbed ends that were pointed away from the surface would be rapidly capped.

Though we showed that motility *in vitro* requires polycations, the requirement of polyvalent cations such as magnesium for motility in vivo remains unclear. Magnesium has long been associated with integrin-mediated cell attachments that provide traction for moving cells [160]. The metal ion-dependent adhesion site (MIDAS) extracellular domains found in all β- and some α-integrins requires Mg^{2+} to coordinate extracellular matrix binding [161-164]. For example, wound healing *in vivo* is blocked by chronic removal of Mg^{2+} from the wound fluid [165]. However, cell spreading is also an actin polymerization-driven process very similar to directed motility [166]. Like Ca^{2+}, Mg^{2+} levels can be acutely increased by release from mitochondrial, nuclear, and ER stores, and chronic exposure of cells to low extracellular Mg^{2+} would deplete stores.

Could the requirement of extracellular Mg^{2+} for integrin-mediated cell adhesion have masked its intracellular requirement for actin-based motility? Typical cellular free Mg^{2+} concentrations range from 0.5 to 1.5 mM [146-148, 167], precisely the range at which we find the greatest effect on processive motility in vitro (Figure **2.4**). While it should be noted that cellular Mg^{2+} measurements have varied for the same cell type [167], intracellular Mg^{2+} levels

have been shown to increase upon cell stimulation. For example, free cellular Mg^{2+} levels in platelets increase from 0.6 to 1.27 mM upon insulin stimulation [168] and from 0.5 to 1.3 mM upon thrombin stimulation [169].

High cellular Mg^{2+} levels have been linked to angiogenesis and endothelial cell migration. Though Mg^{2+} increases cell proliferation [170], its main action during angiogenesis appears to be linked to motility [171]. Lapidos et al [172] found that Mg^{2+} acted as potent chemoattractant for endothelial cells. Chemotaxis towards Mg^{2+} was blocked by inhibition of $G_{\alpha}i$ heterotrimeric G-proteins. Thus, Mg^{2+} chemotaxis involved second messengers and was not due solely to a gradient of integrin-mediated adhesion. Studies of free cytoplasmic Mg^{2+} with mag-fura-2 showed that cytoplasmic Mg^{2+} rapidly increased in endothelial cells from basal levels of 0.5 mM to 1.1–1.2 mM upon stimulation with the chemoattractants VEGF [173] or bFGF [174] due to release from intracellular stores. While this study does not directly address cellular Mg^{2+} levels, our findings point to direct participation of Mg^{2+} in the motility process.

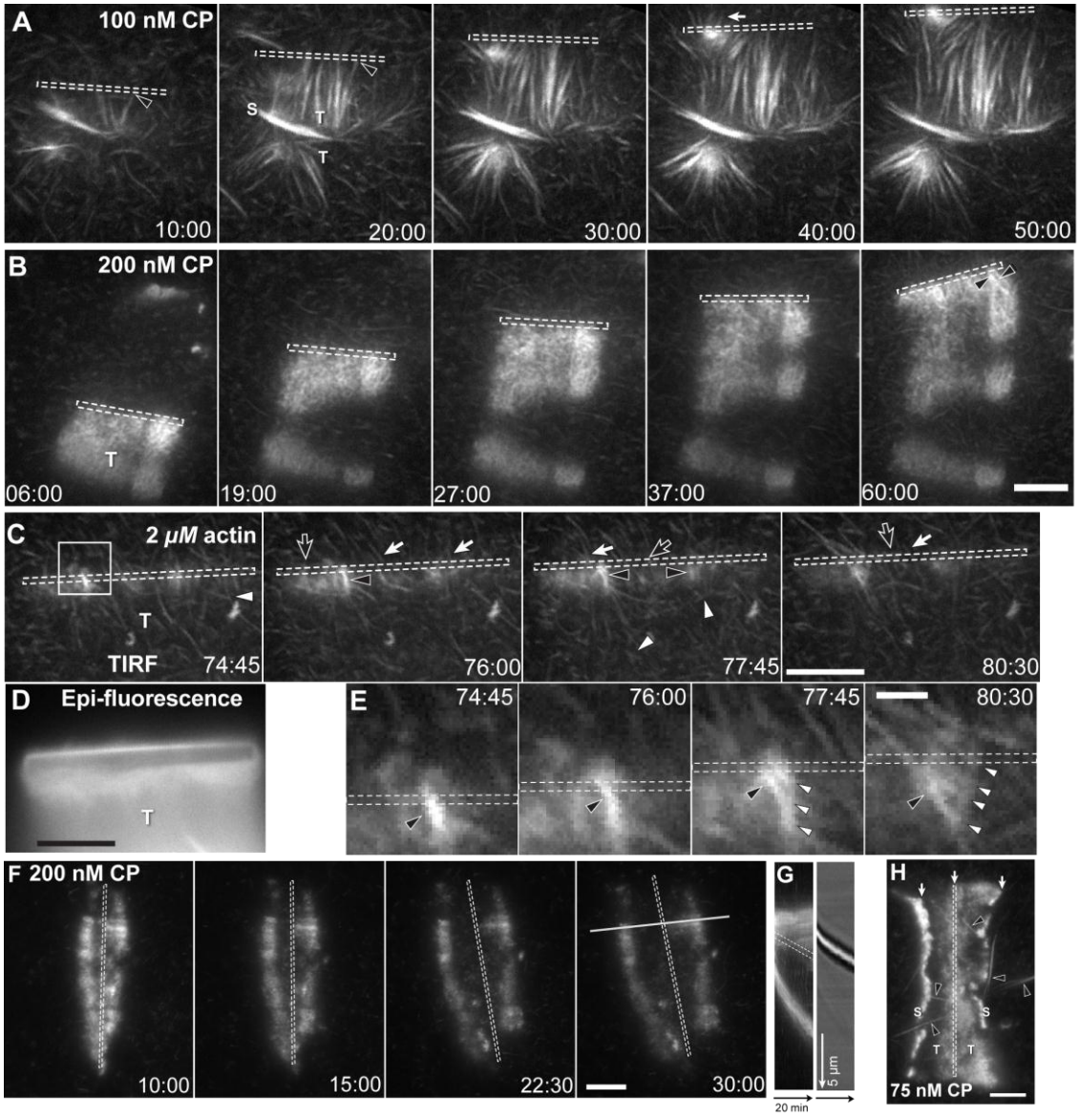

Figure 2.1. Actin filament and branch geometry in comet tails under TIRF microscopy.

Conditions: A-B, 8.5 μM (8% labeled) actin, 9 μM profilin, 100 nM Arp2/3, CP as indicated; C-E, 2 μM (10% labeled) actin, 3 μM profilin, 20 nM Arp2/3, 40 nM CP; F-H, 8.5 μM (8% labeled) actin, 9 μM profilin, 100 nM Arp2/3, CP as indicated; nanofibers coated with 10 μM GST-WCA from N-WASP, motility buffer, 0.38 mM total ATP. **(A-B)** Actin architecture in comet tails (T) of moving nanofibers (dashed outline) was visible under TIRF microscopy. In 100 nM CP, comet tails consisted primarily of long filament bundles. Increasing CP to 200 nM

generated a branched actin networks with short bundles (Black arrowhead). **(C)** Lowering profilin-actin, Arp2/3, and CP concentrations showed individual filaments and branches (white arrowheads) in the comet tail (T). Some filaments (white arrows) crossed the nanofiber boundary, while others terminated at the nanofiber (black arrows). Brighter filament bundles (black arrowhead) terminated at the nanofiber. **(D)** Epi-fluorescence image of panel C. **(E)** Magnified image of box in B showing bundle (black arrowhead) dissociation. The bundle was formed from daughter filaments from the same mother filament (white arrowheads). **(F)** In high CP, nanofibers sometimes formed two comet tails. **(G)** Kymograph of line in F showing tail expansion at the nanofiber surface (dashed outline) under TIRF (*left*) and DIC (*right*) microscopy. **(H)** Nanofibers sometimes formed two comet tails in low CP. Long actin bundles (black arrowheads) appeared within and beyond the comet tails. Scale bars are 1 μm for E and 5 μm for all others. Times are shown in min:sec.

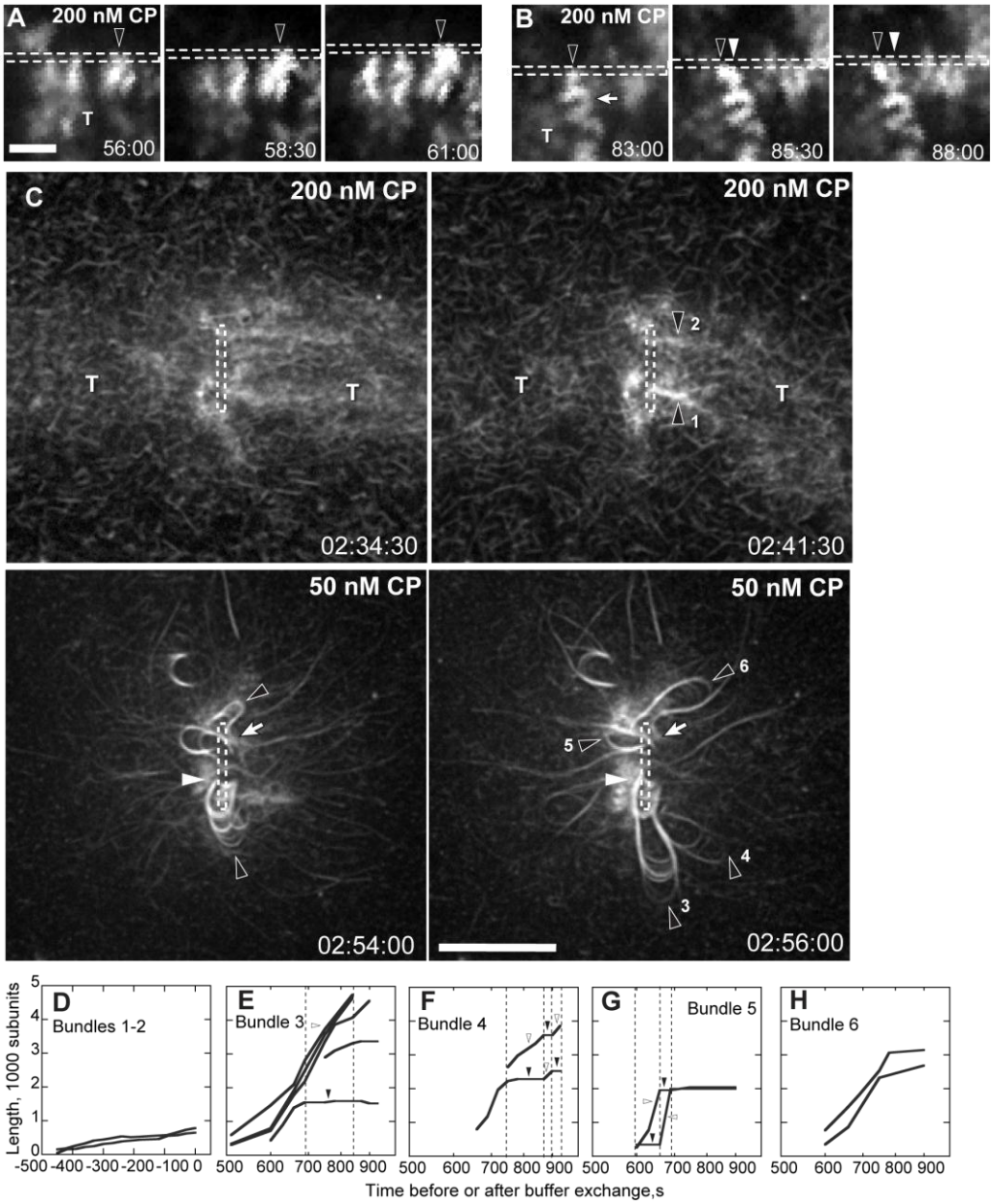

Figure 2.2. Filament bundles processively attach to the nanofiber.

Conditions: 8.5 μM (8 to 20% labeled) Mg-ATP actin, 9 μM profilin, 100 nM Arp2/3, and indicated CP. Nanofiber coating and buffers as in Figure **2.1**. **(A-B)** Bright filament spots grew against the nanofiber surface. Spots either remained attached to the same location on the moving nanofiber (A, black arrowhead) or oscillated back and forth along the moving nanofiber (B, blacks arrowhead). Bright spots grew faster than the surrounding comet tail network (T) and

often buckled from compression between the nanofiber and tail network (arrow). White arrowhead in B indicates bundle starting position. **(C)** CP was lowered from 200 to 50 nM after the establishment of two comet tails (T) by motility buffer exchange. Short, bright bundles (top panels, black arrowheads) became rapidly polymerizing bundled loops (black arrowheads, bottom panels) that remained attached to the nanofiber at their growing ends (white arrowhead) and to the tail at their pointed ends (white arrows). Growing bundles splayed into filaments of different loop lengths. **(D)** Traces of bundles lengths over time before CP reduction. Zero seconds represents the point of buffer exchange, 163 min after the experiment start. **(E-H)** Traces of individual filament lengths over time after CP reduction showed that filament within each bundle grew at different rates. Plots represent filaments from the same bundle. Some filaments continuously elongated while others show pulsed growth. Scale bars are 1 μm for A-B and 5 μm for C. Times are shown in min:sec for A-B and hr:min:sec for C.

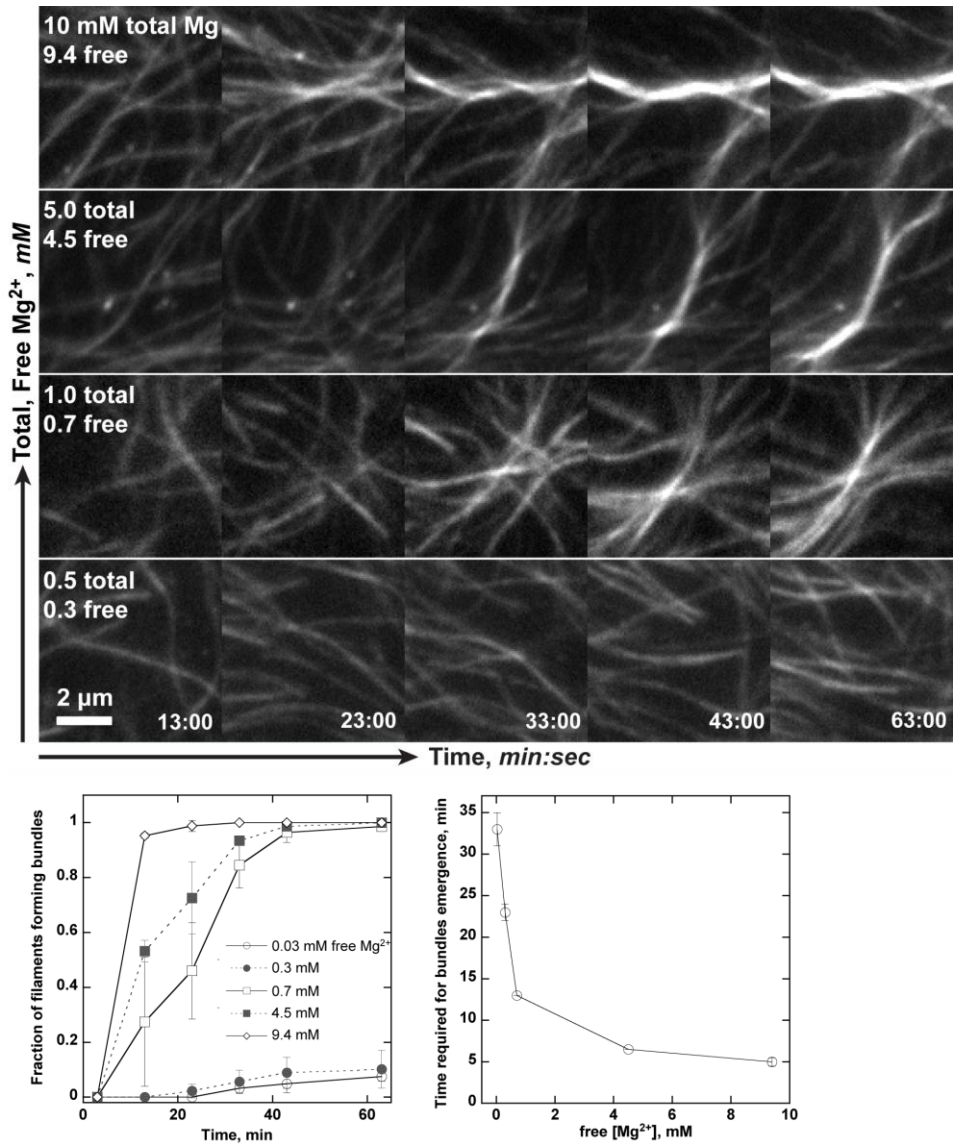

Figure 2.3. Cellular Mg^{2+} concentrations bundle actin filaments at high densities.

Conditions: 2.5 µM (20% labeled) Mg-ATP actin, 50 mM KCl, 1.05 mM EGTA, 10 mM imidazole, pH 7.0, 100 mM DTT, 0.2 mM ATP, 15 mM glucose, 20 µg/ml catalase, 100 ug/ml glucose oxidase 0.25% 1500 cP methylcellulose. **(A)** Time-lapse TIRF microscopy images of *de novo* nucleated actin filaments. Images in each column were taken at the same time (min:sec) after addition of salts. $MgCl_2$ was added to low Mg-EGTA polymerization buffer to set the total Mg^{2+} as indicated. Free [Mg^{2+}] was calculated from pH, ionic strength, and total Ca^{2+}, Mg^{2+},

EGTA, and ATP. Actin bundles readily formed at 1 mM total Mg^{2+} once filament densities increased. Increasing total Mg^{2+} to 5 or 10 mM increased the speed and extent of bundle formation. **(B)** Fraction of filaments forming bundles over time. Free Mg^{2+} concentration of at least 0.7 mM significantly increased bundle formations. **(C)** Time at which the first bundle was observed as a function of Mg^{2+} concentration. Scale bar is 2 μm.

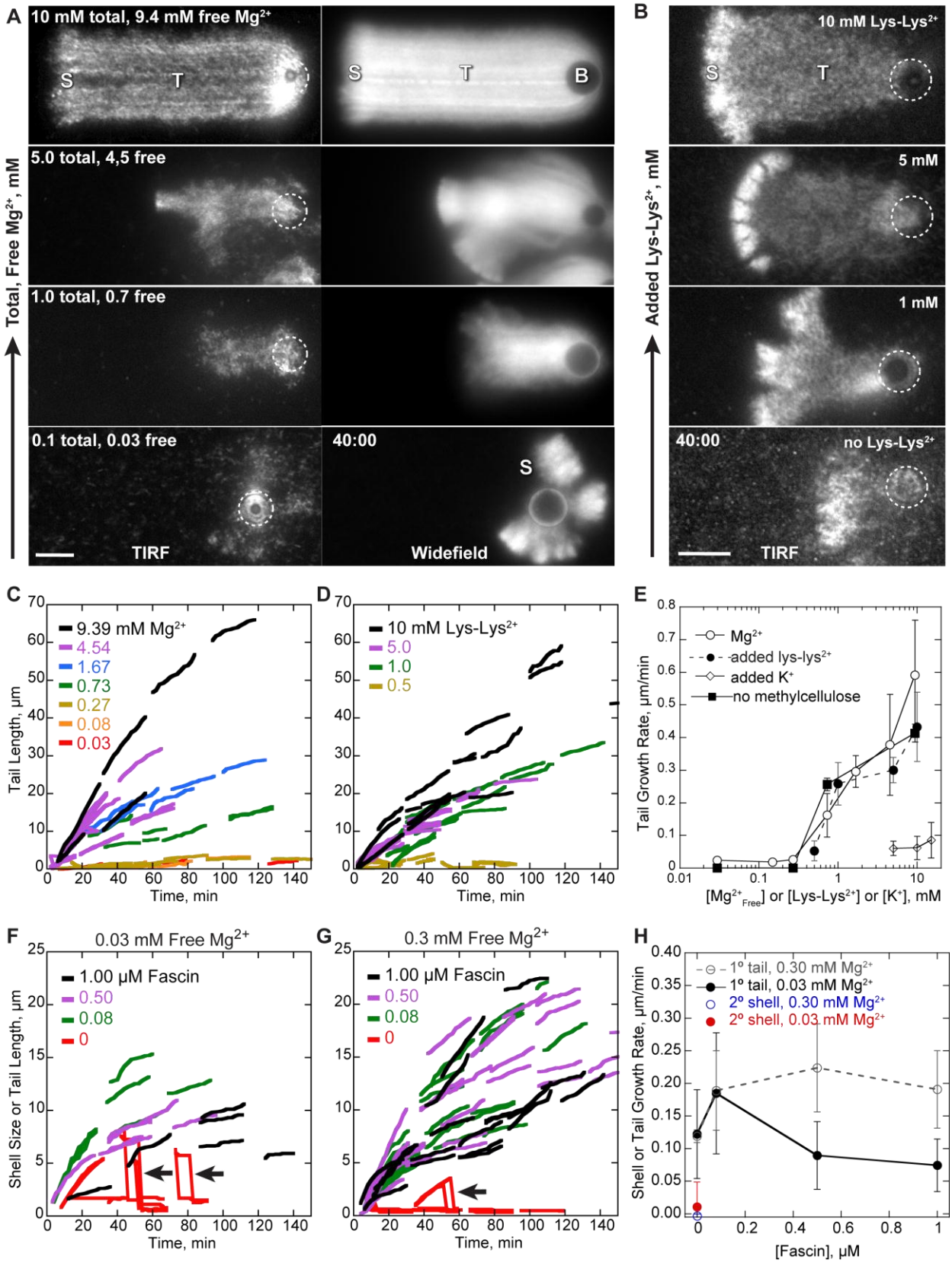
A
10 mM total, 9.4 mM free Mg2+
S
T
C
S
T
B
5.0 total, 4,5 free
1.0 total, 0.7 free
0.1 total, 0.03 free
40:00
S
TIRF
Widefield
Total, Free Mg2+, mM
B
10 mM Lys-Lys2+
S
T
5 mM
1 mM
40:00
no Lys-Lys2+
TIRF
Added Lys-Lys2+, mM
C
9.39 mM Mg2+
4.54
1.67
0.73
0.27
0.08
0.03
Tail Length, µm
Time, min
D
10 mM Lys-Lys2+
5.0
1.0
0.5
Time, min
E
Mg2+
added lys-lys2+
added K+
no methylcellulose
Tail Growth Rate, µm/min
[Mg2+Free] or [Lys-Lys2+] or [K+], mM
F
0.03 mM Free Mg2+
1.00 µM Fascin
0.50
0.08
0
Shell Size or Tail Length, µm
Time, min
G
0.3 mM Free Mg2+
1.00 µM Fascin
0.50
0.08
0
Time, min
H
1º tail, 0.30 mM Mg2+
1º tail, 0.03 mM Mg2+
2º shell, 0.30 mM Mg2+
2º shell, 0.03 mM Mg2+
Shell or Tail Growth Rate, µm/min
[Fascin], µM

Figure 2.4. Polycations or fascin are required for bead motility.

Conditions: 8.5 μM (20% labeled) Mg-ATP actin, 9 μM profilin, 100 nM Arp2/3, 200 nM CP, 4.5 μm diameter bead coated with 8.5 μM GST-WCA, low Mg^{2+} buffer (50 mM KCl, 0.105 mM $MgCl_2$, 1.05 mM EGTA, 10 mM imidazole pH 7.0, 100 mM DTT, 0.2 mM ATP, 15 mM glucose, 0.25% methylcellulose, 20 μg/ml catalase, 100 ug/ml glucose oxidase) supplemented with $MgCl_2$, Lys-Lys·2HCl, KCl, or fascin as indicated. **(A)** TIRF and Epi-fluorescence microscopy images show representative actin comet tails (T) grown from GST-WCA coated beads (B, dashed circle). All images were recorded 40 minutes after the reaction start. In low Mg^{2+}, beads formed a shell (S) that broke symmetry but rarely a comet tail. Tails that did form remained short and detached from the bead. Restoration of cellular, 1 mM Mg^{2+} restored comet tail growth. Additional Mg^{2+} accelerated comet tail growth. **(B)** TIRF microscopy images of actin comet tails grown in 0.1 mM total Mg^{2+} with added Lys-Lys^{2+} as indicated. All images were recorded 40 minutes after the reaction start. Lys-Lys^{2+} substituted for Mg^{2+} to restore motility. **(C-D)** Comet tail growth over time after the reactions start. The lengths of actin comet tails from A-B were recorded in each frame. Line segments represent growth of individual comet tails. Comet tail growth increased with the concentration of divalent cation, either in the form of (C) Mg^{2+} or (D) Lys-Lys^{2+}. **(E)** Comet tail growth rates from C-D as a function of free cation. Both $MgCl_2$ and Lys-Lys-2HCl restored motility in a concentration dependent manner. Removal of methylcellulose did not influence the trend of comet tail growth rates as a function of Mg^{2+}. Addition of 5, 10, or 15 mM KCl did not restore motility in low Mg^{2+} buffers. **(F-G)** Comet tail growth over time in low Mg^{2+} with added fascin. Line segments represent individual comet tails. (F) In low, 0.03 mM free Mg^{2+}, 80 nM fascin optimally restored motility while (G) 500 nM fascin optimally restored motility in 0.3 mM free Mg^{2+}. Line breaks (arrows) in no fascin

represent growth of an actin shell followed by shell detachment during an observation. **(H)** Comet tail growth rates from F-G as a function of fascin concentration. Errors bars in E and H show S.D. of tail growth rates. Scale bars in A-B are 5 μm.

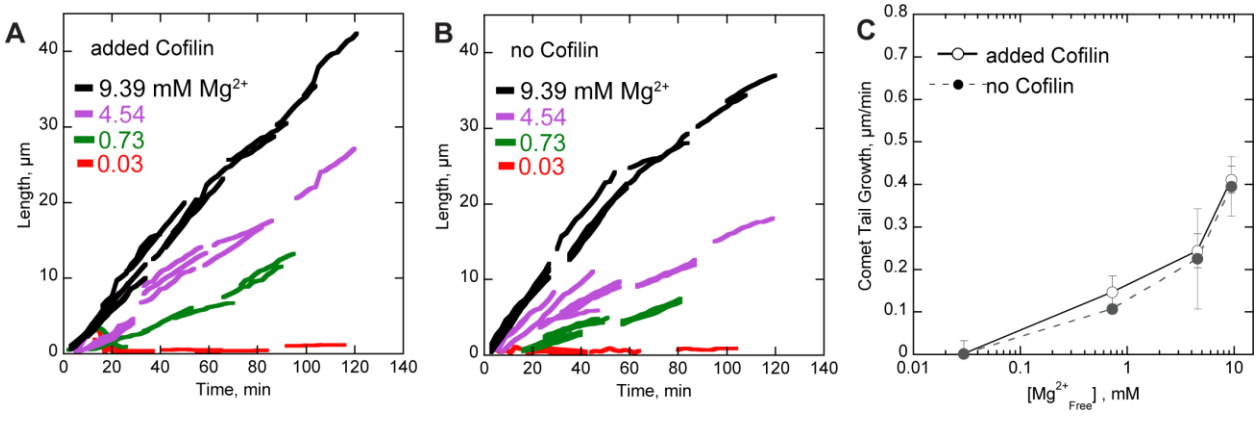

Figure 2.5. Polycation-dependent motility does not require cofilin.

Conditions: 8.5 µM (20% labeled) Mg-ATP actin, 9 µM profilin, 100 nM Arp2/3, 200 nM CP, 2 µM cofilin, 4.5 µm diameter bead coated with 8.5 µM GST-WCA, low Mg^{2+} buffer as in Figure **2.4** supplemented with $MgCl_2$ as indicated. (A-B) Comet tail growth over time after the reactions start in the presence (A) and absence (B) of cofilin. The lengths of actin comet tails were recorded in each frame. Line segments represent growth of individual comet tails. Comet tail growth increased with the concentration of Mg^{2+}, either in the presence or absence of cofilin. (C) Comet tail growth rates from A-B as a function of free Mg^{2+}. $MgCl_2$ restored motility in a concentration-dependent manner in the presence or absence of cofilin. Errors bars show S.D. of tail growth rates.

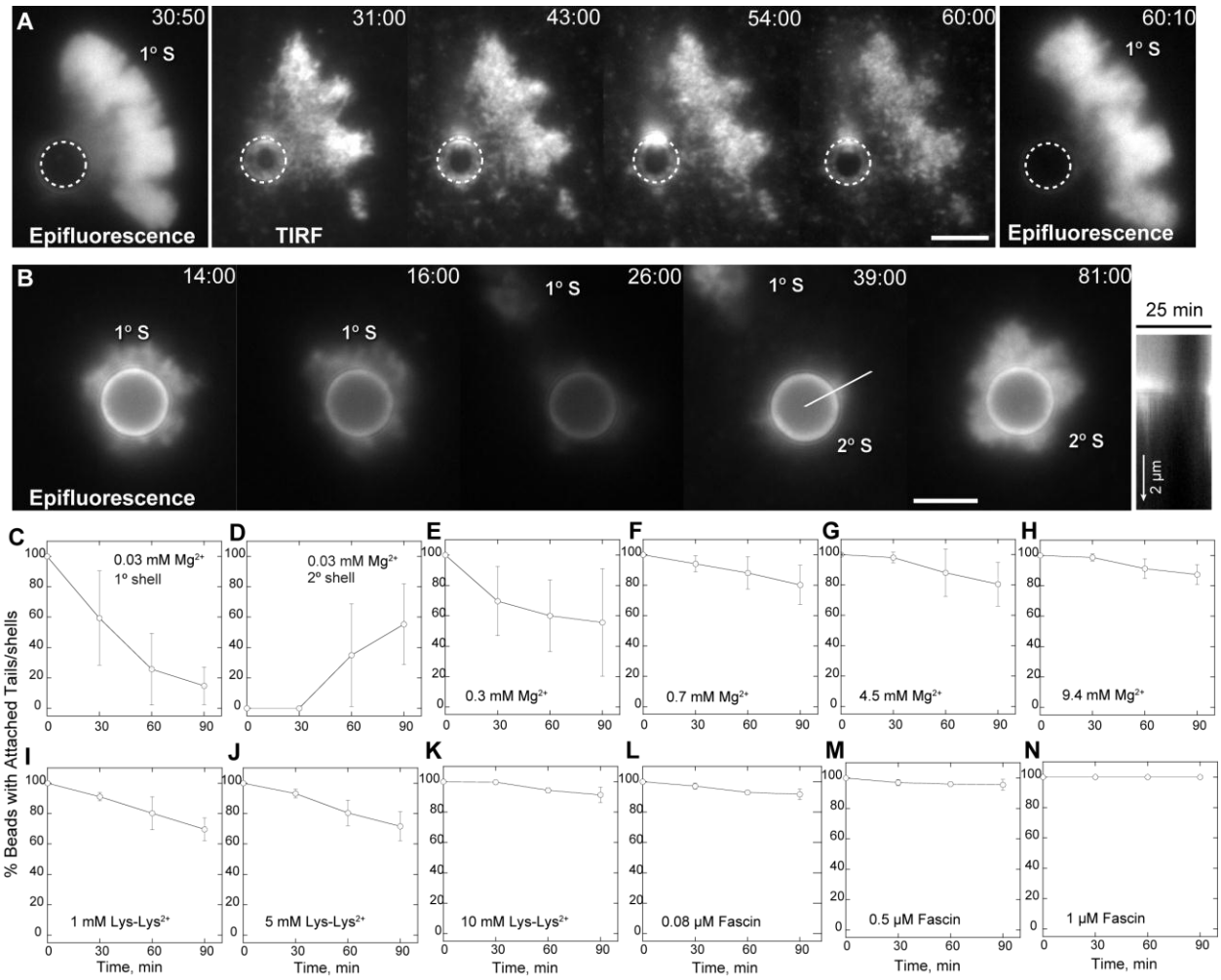

Figure 2.6. Divalent cations or fascin rescues comet tail attachment.

Conditions as in Figure **2.4**. **(A)** Time-lapse epi-fluorescence and TIRF microscopy sequence showing detachment of primary actin shell (1 ºS) from GST-WCA coated bead in 0.03 free Mg^{2+}. Filament density between the shell and the bead surface (dotted circle) is gradually lost. **(B)** Epi-fluorescence fluorescence microscopy showing formation of secondary actin shell (2 ºS) after detachment of primary actin shell (1 ºS) in low Mg^{2+}. Times are shown as min:sec. Scale bars are 5 µm. **(C)** Kymograph of line in B showing the detachment of primary shell (1) and establishment of a secondary shell (2). **(D-O)** Percentage of GST-WCA coated beads with either an actin shell or comet tail over time. At the reaction start, all beads developed a thin actin

shell. In low 0.03 mM free Mg^{2+} buffer, actin shells detached over time (D) and many beads formed a secondary actin shell (E). Addition of 0.3 mM (F), 0.7 mM (G), 4.5 mM (H), or 9.4 mM (I) free Mg^{2+} restored shell or comet tail attachment. Addition of either 1 mM (J), 5 mM (K), or 10 mM (L) Lys-Lys^{2+} restored actin shell or tail attachment in 0.03 mM free Mg^{2+} buffer. Addition of 80 nM (M), 0.5 μM (N), or 1 μM (O) fascin restored actin shell or tail attachment in 0.03 mM free Mg^{2+} buffer. Means and S.D. were calculated from three independent experiments. At least 50 beads were counted in each experiment.

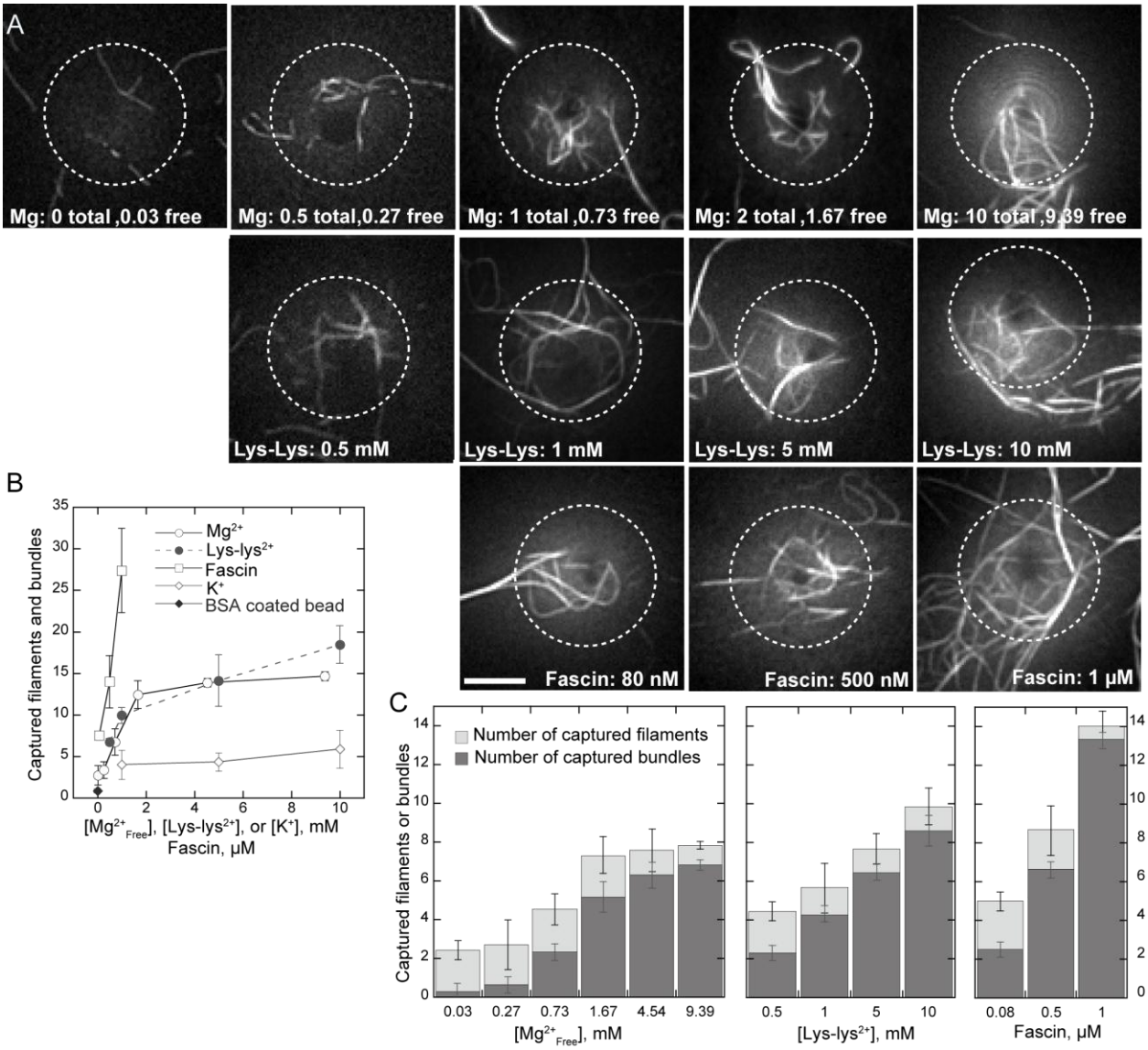

Figure 2.7. Bundling promotes barbed end attachment to WCA domains in the absence of Arp2/3 complex.

Conditions: 8 µM (30% labeled) actin was polymerized in low Mg^{2+} F buffer. Filaments were incubated with GST-WCA coated microspheres with 1 µM ATP-actin monomers and the indicated final concentration of Mg^{2+}, Lys-Lys^{2+}, fascin, or K^{+} for 10 minutes. Beads were centrifuged, resuspended in low Mg^{2+} buffer in the absence of methylcellulose, and imaged on poly-lysine coated coverslips. **(A)** TIRF microscopy images of actin filaments and bundles

attached to the bottom of coated microspheres in the indicated concentration of Mg^{2+}, Lys-Lys^{2+}, fascin, or K^{+}. The number of actin filaments and bundles crossing the bead boundary (dashed circle) were counted for each bead. Scale bar is 2 μm. An example measurement is shown in Figure**Figure 1.1**. **(B)** Count of average number of captured filaments per bead as a function of Mg^{2+} (○), Lys-Lys^{2+} (●), fascin (□), or K^{+} (◇) concentration. Bundles were counted as two filaments. Error bars show S.D. from at least 60 beads for each condition from three independent experiments. Coincidental filament overlap with control, BSA coated microsphere (◆) was negligible. (C) Stacked bar chart showing average number of filaments (light gray) or bundles (dark gray) captured by WCA-coated microspheres, with indicated Mg^{2+}, Lys-Lys^{2+}, fascin concentrations. The proportion of captured bundles increased with increasing polycation or fascin.

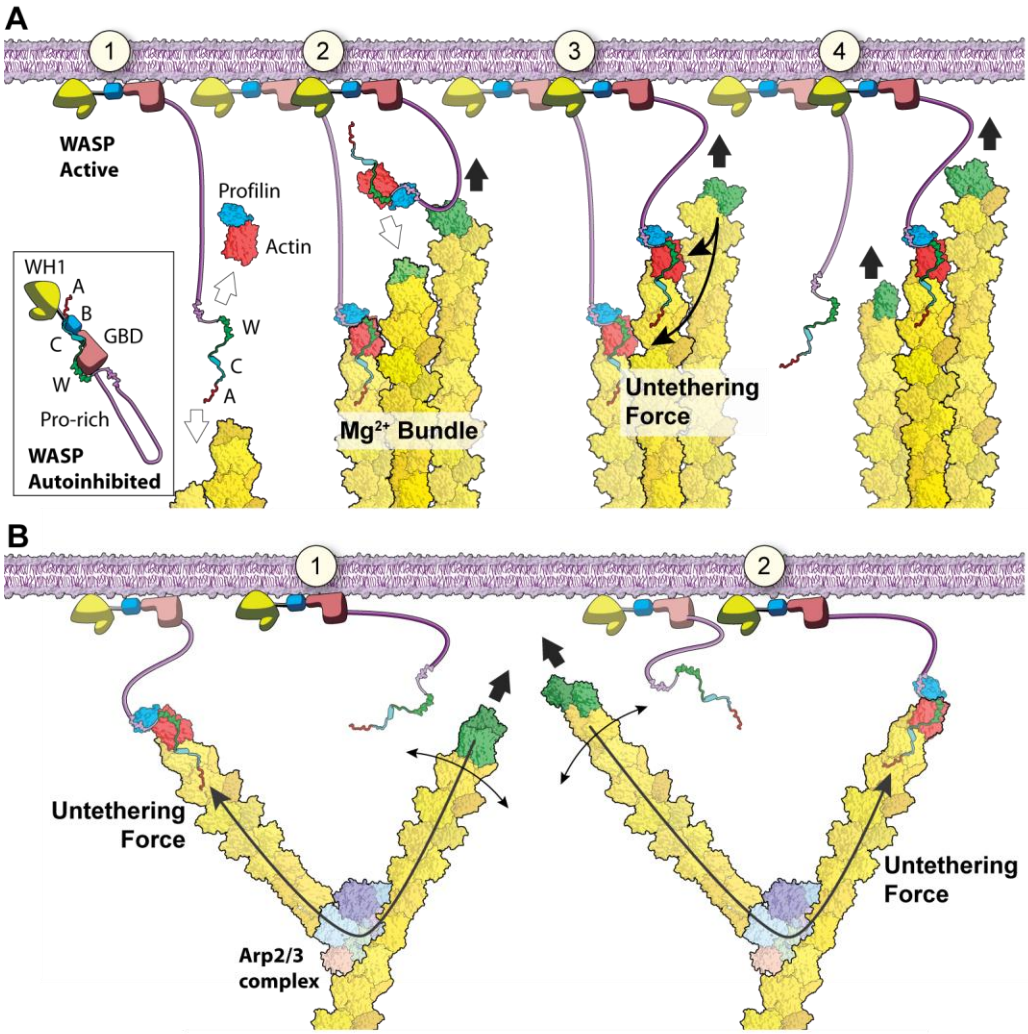

Figure 2.8. Model of bundle and branch cooperativity.

(A) Bundles cooperate efficiently to maintain barbed end orientation. (1) WASP binding to membrane and Rho family GTPase frees active WCA domains that can either bind to a free profilin-actin or the barbed end of a nearby filament bundle. (2) One filament in a bundle is attached to WCA (red), while sister filaments are free to either polymerize by subunit addition (green), bind to a nearby free WCA, or (3) bind to a profilin-actin bound WCA. The force of polymerization is efficiently transmitted through the stiff bundle to tethered barbed ends and

promotes tether dissociation. (4) Dissociation of bound WCA frees a sister barbed end for polymerization. **(B)** Branches cooperative inefficiently to maintain barbed end orientation. (1) While one barbed end is tethered to the membrane through WCA, a nearby barbed end polymerizes against the membrane (green). The force of polymerization is transmitted through branches and flexible filaments to tethered barbed ends to promote tether dissociation. (2) WCA dissociation frees a barbed end for polymerization while other filaments within the branched network become tethered.

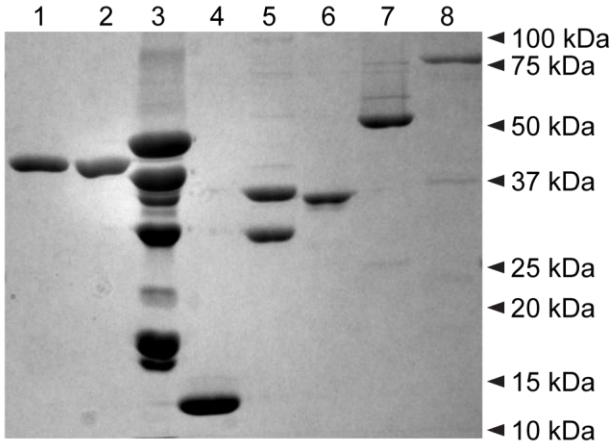

Figure 2.9. Coomassie stained SDS-PAGE gel of purified motility proteins.

Lane 1, unlabeled rabbit skeletal muscle actin; Lane 2, Oregon green 488 labeled skeletal muscle actin; Lane 3, bovine thymus Arp2/3 complex; Lane 4, recombinant human profilin; Lane 5, recombinant mouse capping protein; Lane 6, recombinant glutathione sepharose transferase (GST) N-terminal tagged WCA domains from human N-WASP; Lane 7, recombinant human fascin; Lane 8; rabbit skeletal muscle myosin II heavy chain inactivated with N-Ethylmaleimide.

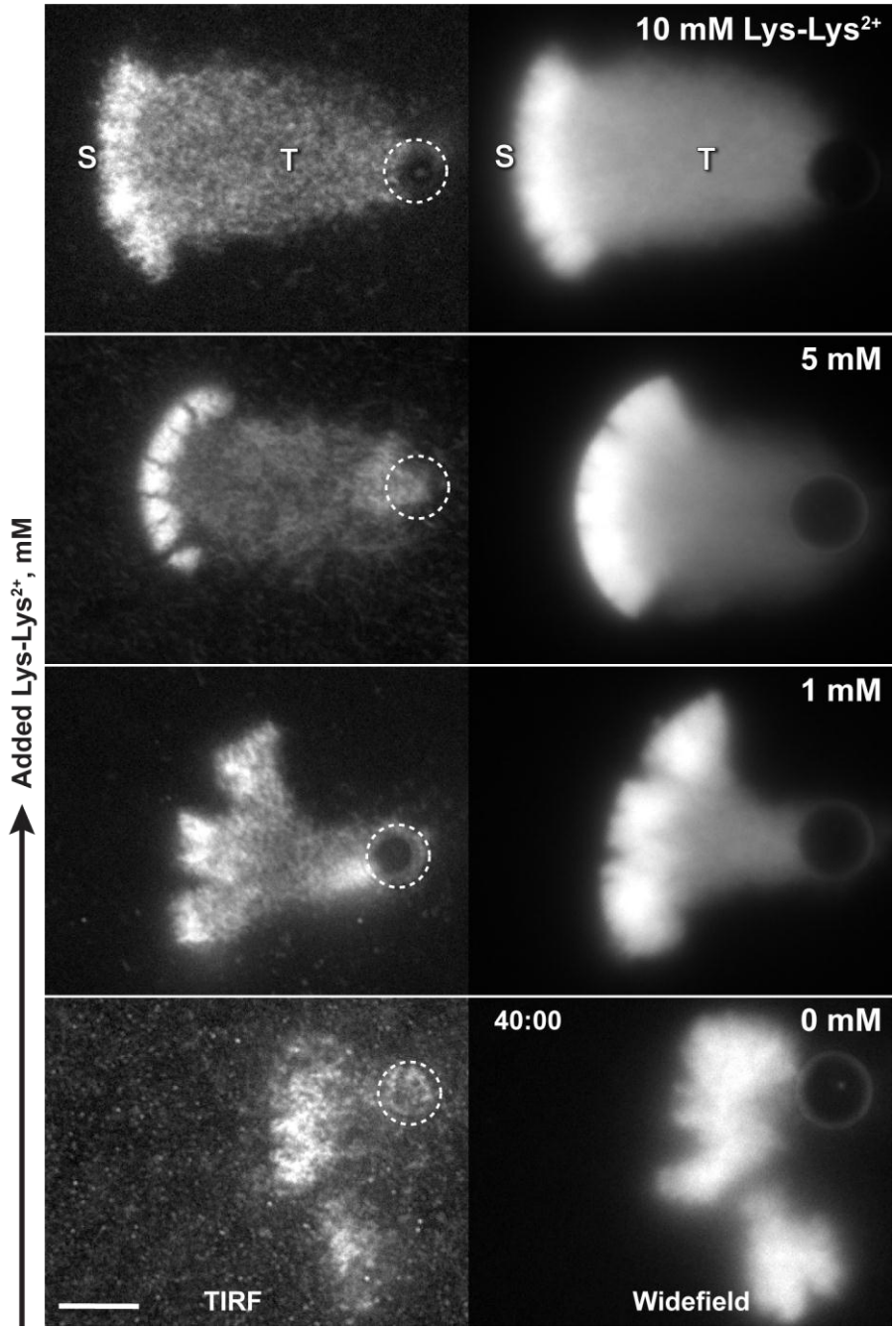

Figure 2.10. Lys-Lys2+ restores motility.

Conditions as in Figure **2.4**B. TIRF and epi-fluorescence microscopy images of actin shells (S) and comet tails (T) grown from GST-WCA coated beads in 0.1 mM total, 0.03 mM free

Mg^{2+} buffer with added Lys-Lys^{2+} as indicated. Each image was recorded 40 minutes after initiation of the reaction. Lys-Lys^{2+} substituted for Mg^{2+} to restore motility. Scale bar is 5 μm.

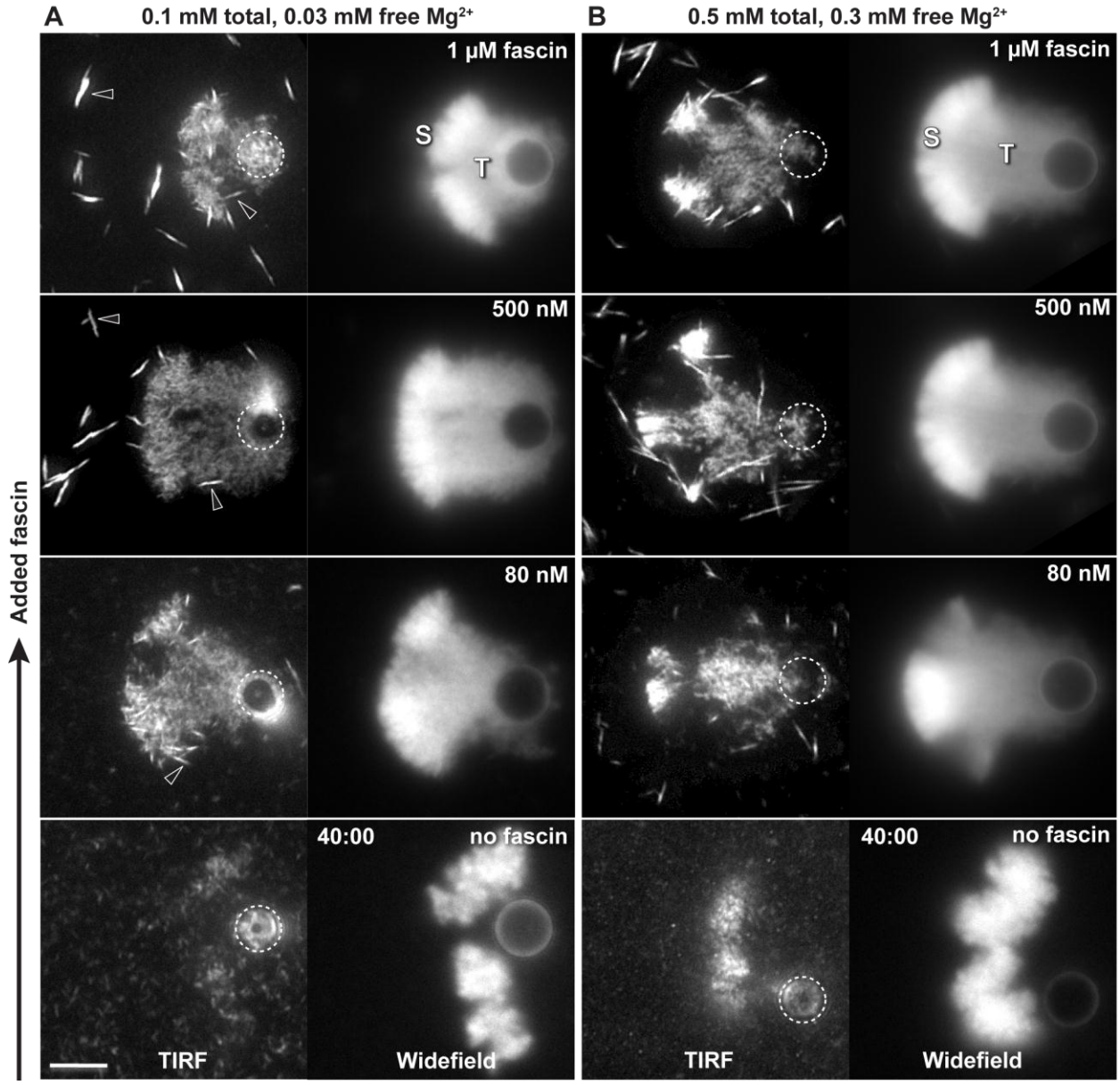

Figure 2.11.Fascin restores motility.

Conditions as in Figure **2.4**. **(A)** TIRF and epi-fluorescence microscopy images of actin shells (S) and comet tails (T) grown from GST-WCA coated beads in 0.1 mM total, 0.03 mM free Mg^{2+} buffer with added fascin as indicated. Fascin added to 80 nM optimally restored comet tail elongation. Straight fascin bundles (black arrowheads) can be seen both within the comet tail and in the surrounding media. **(B)** Actin shells (S) and comet tails (T) grown in 0.5 mM total, 0.3 mM free Mg^{2+} buffer with added fascin as indicated. Although 0.3 mM free Mg^{2+} did not support

motility on its own, fascin addition restored motility to a greater extent than in 0.03 mM free Mg^{2+}. Each image was recorded 40 minutes after initiation of the reaction. Scale bar is 5 μm.

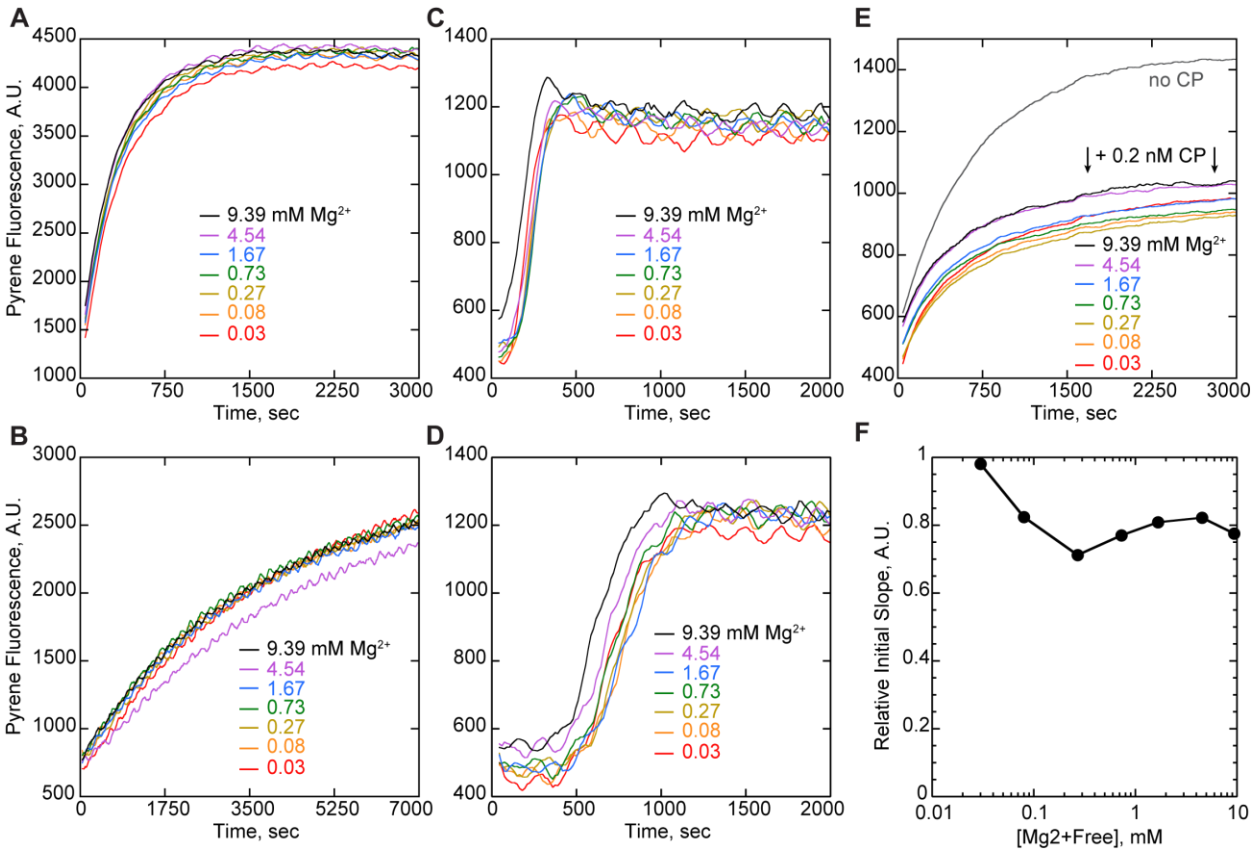

Figure 2.12. Minimal Mg^{2+} is sufficient for actin polymerization, Arp2/3 nucleation, and CP activity.

Polymerization of pyrene actin in low Mg^{2+} buffer (50 mM KCl, 0.105 mM $MgCl_2$, 1.05 mM EGTA, 10 mM imidazole pH 7.0, 0.2 mM ATP). $MgCl_2$ was added to generate indicated free [Mg^{2+}]. **(A)** Polymerization of 8.5 µM (30% pyrene labeled) Mg-ATP-actin induced by KCl was not affected by $MgCl_2$ concentration. **(B)** Addition of 8.5 µM human profilin to 8.5 µM actin did not affect Mg^{2+} independent actin polymerization. **(C)** Nucleation of 2 µM (30% labeled) Mg-ATP-actin by 40 nM Arp2/3 and 500 nM bovine N-WASP WCA. Mg^{2+} did not affect the time course or extent of Arp2/3 mediated nucleation. **(D)** Nucleation conditions in C with addition of 2 µM profilin. Profilin did not significantly alter the Mg^{2+} independence of Arp2/3 nucleation. **(E)** Polymerization from capped seeds. Short unlabeled actin seeds diluted to

1.2 μM filament were incubated with 0.2 nM CP or buffer alone (no CP). Capped seeds were added to 1 μM (30% pyrene labeled) actin, 3 μM profilin at the reaction start. **(F)** Normalized initial slope from the first 200 s of polymerization from capped seeds in E.

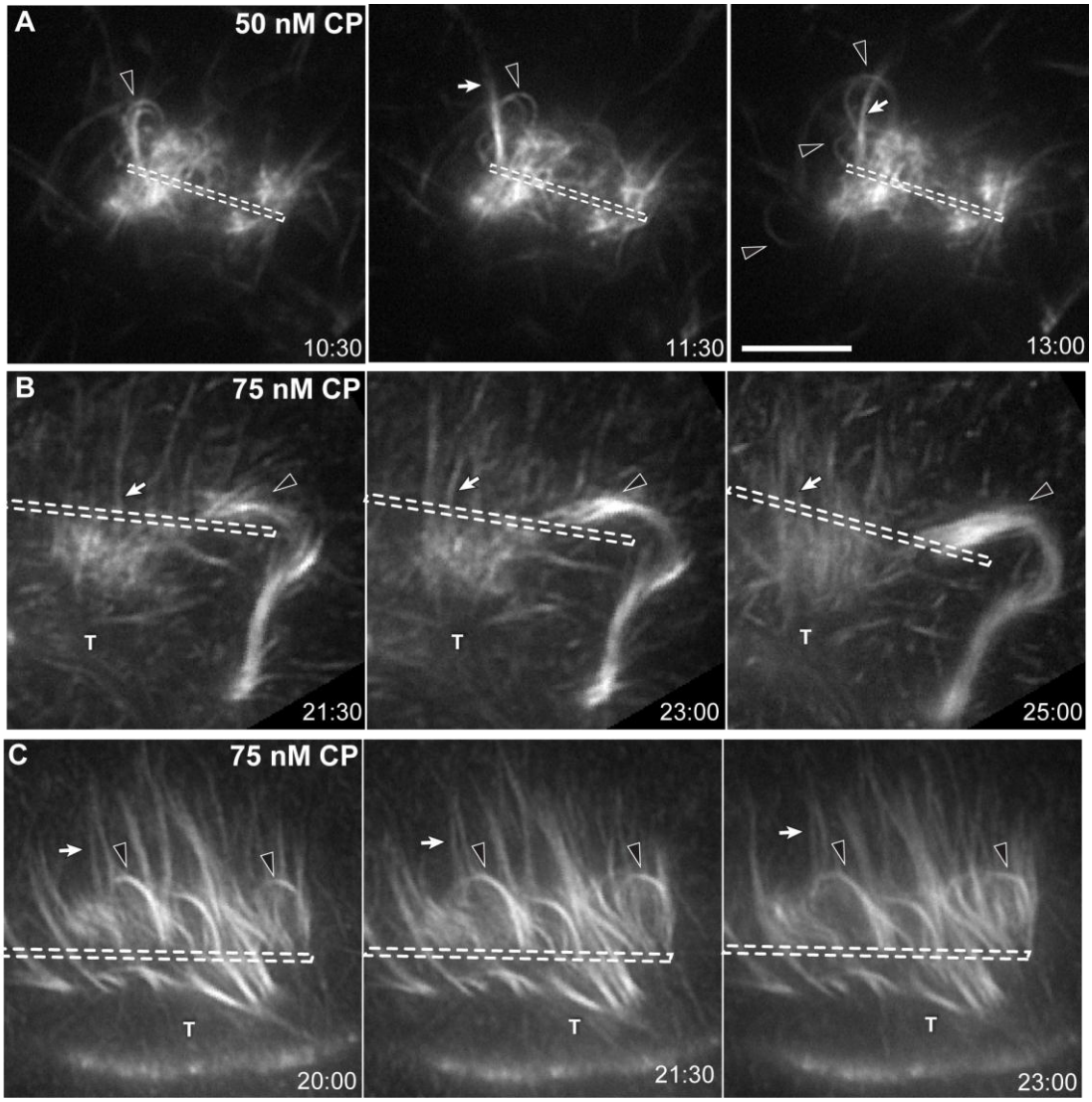

Figure 2.13.Looped bundles formed in low CP.

Conditions: 8.5 μM (8% labeled) actin, 9 μM profilin, 100 nM Arp2/3, CP as indicated. **(A-C)** At low CP concentrations, bundled loops (*black arrowheads*) often formed on both stationary (A) and moving (B-C) nanofibers. Loops grew with one end embedded in the comet tail (T) and the other attached to the nanofiber surface (*dashed outline*). In additional to looped bundles, straight bundles (*white arrows*) often projected beyond the nanofiber surface at low CP concentrations. Scale bar, 5 μm. Time, min: sec.

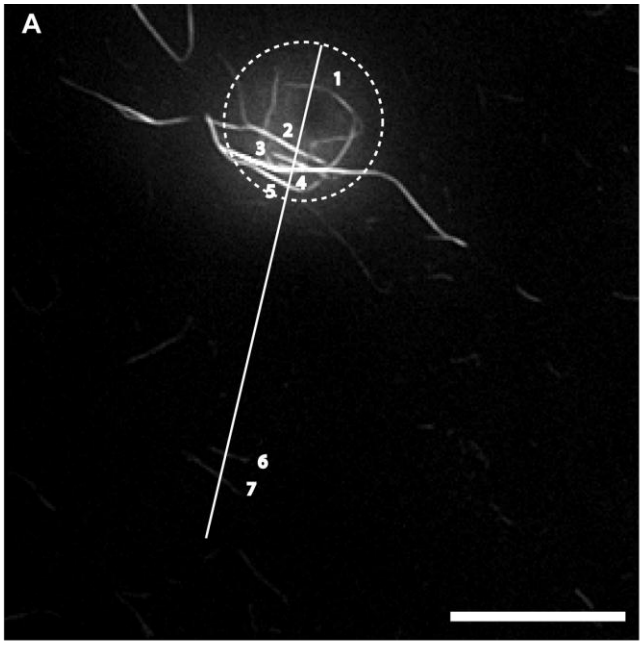

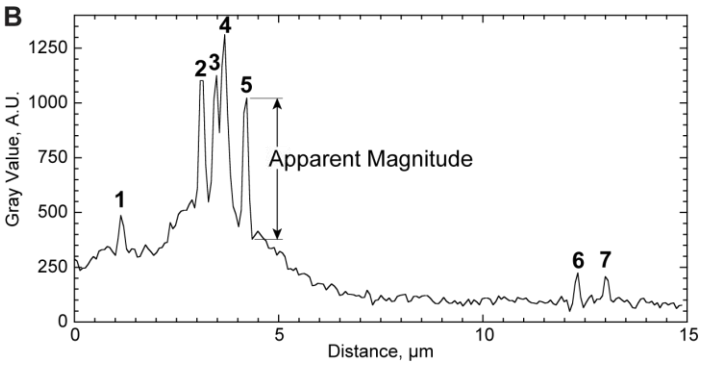

C

Filament No.	1	2	3	4	5	6	7
Magnitude	162	744	704	1048	703	135	113
Captured	+	+	+	+	+	–	–
Scored as	Fil	Bun	Bun	Bun	Bun	Fil	Fil

Figure 2.14. Scoring of bundles captured by GST-WCA coated beads.

(A) Sample TIRF microscopy image of actin filaments captured by a GST-WCA coated bead (*dashed circle*) in 0.03 mM free Mg^{2+} supplemented with 1 mM Lys-Lys^{2+}. Scale bar, 5 µm. **(B)** Profile plot of fluorescent intensity along the line in A that intersects seven filaments. Numbered peaks correspond to marked filaments. Two dim background filaments are included for comparison. **(C)** Sample scoring method for experiments shown in Figure **2.7**. Camera gain, acquisition time, and display range were kept constant between experiments to give roughly the

same apparent magnitude (peak-to-trough intensity) of background filaments (6-7). Filaments were scored as captured (+) if they crossed or were contained within the bead boundary as measured with DIC microscopy. Captured filaments with apparent magnitudes similar to background filaments were scored as individual filaments (Fil). Captured filaments with apparent magnitudes of at least double the average magnitude of background filaments were scored as bundles (Bun).

Tables

Table I. Average particle velocities in 8.5 μM profilin-actin, 100 nM Arp2/3.

Particle	[ATP] *mM*	[Cofilin] *μM*	[CP] *nM*	Tail Growth *μm/min*
Nanofibers	0.38	–	75	0.08 ± 0.05 (14)
Nanofibers	0.38	–	100	0.14 ± 0.05 (24)
Nanofibers	0.38	–	200	0.11 ± 0.06 (20)
4.5 μm Beads	0.38	2.0	200	0.51 ± 0.04 (10)
4.5 μm Beads	0.38	–	200	0.48 ± 0.12 (10)
4.5 μm Beads	0.2	–	200	0.17 ± 0.02 (7)

Table II Frequency of bundle formation on nanofibers.

Conditions as in Table I.

[CP]	Percentage of Nanofibers			No. Nanofibers
nM	with bundles	with loops	with buckles	observed
≤ 75	100	27	0	37
100	96	8	25	24
200	95	21	51	57

Chapter 3 Capping protein and N-Wasp cooperate to orient barbed end toward the leading edge

Xiaohua Hu and Jeffrey R. Kuhn

Abstract

Motile cells orient actin filament at the leading edge such that fast-growing barbed ends face the membrane. We used in vitro motility assays with N-WASP WWCA coated nanofibers and total internal reflection fluorescence (TIRF) microscopy to determine how WWCA domains, capping protein (CP), and Arp2/3 generate this barbed end orientation. In the absence of CP, Arp2/3 nucleates barbed ends that grow away from the nanofiber surface and branches remain stably attached to their WWCA tethers. CP addition causes barbed ends to pivot toward the nanofiber. CP-mediated reorientation is accompanied by both the shedding of short branches from the nanofiber and barbed end capture by the nanofiber. On drifting nanofibers, reoriented branches pivoted at their barbed end, showing specific barbed end tethering rather than branch-point attachment. Barbed end retention by nanofibers correlated to capping, and barbed end rapidly detached from the nanofiber upon the resumption of growth. These observations indicate that WWCA and CP bind simultaneously to barbed ends. We used filament pull-down assays and fluorescence anisotropy to confirm cooperative binding of WWCA and CP to barbed ends in the absence of Arp2/3. In pull-down assays, GST-WWCA coated beads captured an average of 8-9 barbed ends as counted by TIRF microscopy. CP addition lead to a biphasic response with a peak of 13 filaments captured per bead at 5 nM CP and a reduction to ~4 ends per bead at 200 nM CP – half the number captured by WWCA alone. We used bulk WWCA binding assays to measure WWCA affinity for mechanically sheared filament barbed ends. End concentration was estimated from seeded pyrene-actin polymerization assays and WWCA binding was measured in parallel by fluorescence anisotropy. We found that labeled WWCA bound to barbed ends with an affinity of 14 pM and unlabeled WWCA with an affinity of 75 pM, similar to the known 80 –

100 pM affinity of CP for barbed ends. CP addition increased WWCA binding slightly at low CP concentrations and decreased WWCA binding to 50% at high CP concentrations. Reduction of WWCA binding by half in both assays shows that CP competes with the terminal WWCA binding site at the barbed end but does not preclude WWCA binding to the penultimate actin subunit. Molecular models of CP and WH2 domains bound respectively to the terminal and penultimate actin subunit showed no overlap between the two molecules and that CP orientation might blocks WWCA dissociation from the penultimate subunit. We propose that simultaneous binding of CP and WWCA to barbed ends is essential to the establishment of filament orientation at the leading edge. Rapid CP association limits growth of Arp2/3 nucleated barbed ends away from the leading edge. Subsequent N-WASP binding to capped barbed ends causes Arp2/3 at the nearby branch junction to detach from N-WASP, pivoting the branch to point in the direction of productive motility. Cooperative CP/N-WASP binding thus presents a new mechanism that refines our understanding of dendritic nucleation at the leading edge.

Introduction

Directed cell migration requires spatially controlled actin nucleation and coordinated actin filament turnover to form a flat protrusion called the lamellipodium. The lamellipodium produces both the protrusive force and traction that drives cell motility. The protrusive force is directed toward the plasma membrane and is driven by actin filament polymerization at the leading edge. Actin polymerization in turn depends on free filament barbed ends nucleated by the Arp2/3 complex. In cells, the majority of Arp2/3 generated barbed ends face toward the leading edge membrane. For example, 80% of myosin S1 decorated actin filament barbed ends in fish keratocytes face toward the leading edge, 5% face away from it, and the remaining 15% lie parallel to the membrane [153]. Computational analysis of undecorated filaments in fixed cells showed that filaments are oriented at $\pm 35^{o}$to the leading edge [175] [133, 176], in accord with the 70º angle between mother and daughter filaments. In contrast, "granddaughter" filaments in isotropically nucleated networks frequently grow in opposite directions of their grandmother source to form a 140 ^{o}angle to the grandmother [19, 31, 121]. In order to maintain the majority of barbed ends facing toward the membrane, the orientation of mother and daughter filaments must be restricted to the canonical at $\pm 35^{o}$. The mechanism by which this orientation of barbed ends toward the leading edge is generated and maintained is still not fully understood.

Membrane-restricted activation of nucleation promoting factors (NPFs) may play a major role in maintaining this "barbed end forward" orientation. The C-terminal WCA domains of cellular NPFs are only exposed at the leading edge membrane to activate the Arp2/3 complex [177, 178]. Membrane-bound WCA domains and Arp2/3 thus nucleate actin branches near the cell membrane. However, this nucleation mechanism is not sufficient to define the orientation preference of barbed ends. When WCA is attached to a bead or nanofiber and incubated with

Arp2/3 and actin, Arp2/3 invariably generates branches with barbed ends facing away from WCA at the particle surface [59, 131, 133, 134]. Therefore, Arp2/3 activation itself is insufficient to generate the canonical "barbed end forward" orientation *in vitro*.

Capping protein (CP) appears to play a key role in organizing branch orientation *in vitro*. Addition of CP to WCA coated particles in *in vitro* motility assays reorganizes the branched network so that actin barbed ends face toward the particle surface rather than away from it [75, 121, 153, 175]. Several hypotheses have been proposed to explain the mechanism of CP mediated reorientation of barbed end. In the First hypothesis, CP reorganizes the actin network by restricting actin network growth near the WCA coated particles, but without necessarily affecting the orientation of branches in the network [131]. In these experiments with CP, the branch orientation was defined by measuring fluorescent intensity along the WCA coated particles followed by photobleaching. Under such condition, fluorophore-labeled actin monomer addition to barbed end would have been inhibited by capping would not indicate the distribution of capped barbed ends. In the second hypothesis, CP somehow acts through Arp2/3 complex to reorganize the actin network [133, 134]. CP increases nucleation efficiency at the particle surface [59], and promotes the formation of dendritic network rather than the stellate structure with barbed ends growing away from particle surface. While this model contributes to understand the role of CP in actin-based motility, it does not completely address how the dendritic actin network is directed to grow toward the particle surface.

Recently, WCA domains were found to tether actin barbed ends to moving leading edges in motility reconstitution assays *in vitro* [31, 75, 86, 179], leading to the proposal that WCA domains contribute to reorient actin network by binding barbed ends. If WCA is involved in this process, the relationship between WCA and CP in binding barbed end and reorganizing actin

network architecture must be defined. Current models of the barbed end tethering assume that CP and WCA binding to barbed ends are mutually exclusive [75]. How then can CP and WCA coordinate barbed end binding and actin network reorganization?

We used total internal reflection microscopy (TIRF) to observe the reorganization of actin architecture in the presence of CP. We have found that, in contrast to mutual exclusivity, CP and N-WASP WWCA domains bind simultaneously to actin filament barbed ends. We show how this cooperative binding leads to a self-correcting mechanism that organizes the canonical "barbed end forward" orientation as motility is initiated. We used bead binding assays and fluorescence anisotropic measurements of WWCA binding to filament barbed ends to show that WWCA domains and CP bind barbed ends with similar affinities, that the order of binding is important, and that CP can enhance WWCA binding to barbed ends. This simple model of cooperative binding between CP and NPFs at the leading edge explains how CP and WCA domains organize barbed ends at the leading edge to generate protrusive forces.

Materials and Methods

Protein expression, purification, and fluorescent labeling. Actin was purified from rabbit skeletal muscle acetone powder through one round of polymerization, depolymerization, and gel filtration [123]. Actin was labeled with pyrenyl iodoacetamide (Invitrogen, Carlsbad, CA) [180]or with Oregon green 488 iodoacetamide (Invitrogen) as previously described [181]. Before use, labeled and unlabeled actins were dialyzed overnight against fresh buffer G (2 mM Tris-HCl pH 8, 0.2 mM ATP, 1 mM NaN_3, 0.1 mM $CaCl_2$, 0.5 mM dithiothreitol, DTT) and centrifuged at 100,000 g for 2 hr at 4 ℃. Arp2/3 complex was purified from bovine thymus as described [182]. Recombinant mouse capping protein was expressed in *E. Coli* and purified as described [126]. Human N-WASP-WWCA was expressed as a glutathione S-transferase (GST) fusion proteins in *E. Coli* and purified on a Glutathione Agarose affinity column (Thermo Scientific, Rockford, IL) followed by anion exchange chromatography on a Source Q (GE Healthcare, Piscataway, NJ) column [111]. Recombinant human profilin I was expressed in *E. Coli* and purified by poly-L-proline affinity chromatography as described [127]. Actin and labeled actins were stored for 1 month at 4 ℃. All other proteins were flash frozen in liquid nitrogen and stored at -80 ℃.

Preparation and labeling of N-WASP WWCA. All cysteines within the sequence of N-WASP WWCA were mutated to alanine using multisites mutagenesis kit (Quickchange II site-directed mutagenesis kit, Agilent, CA). A cysteine was added at to the C-terminus prior to the stop codon using the same method.

Nanofiber preparation. Nanofibers (200 nm nominal diameter, Johns Mansville, Denver, CO) were separated in chloroform with a Dounce homogenizer, centrifuged at 3750 rpm for 15 min in a clinical centrifuge, and the chloroform was evaporated in a fume hood. Nanofibers were washed once with deionized water by centrifugation and sonicated for 1 hour in 1M KOH in a

bath sonicator to remove contaminants. Nanofibers were washed briefly in deionized water, resuspended in 1 M HCl, sonicated for 1 hour, and incubated overnight in HCl. Cleaned nanofibers were subsequently pelleted by centrifugation and sonicated for 30 minutes each in in ddH_2O, 1 mM ethylene diamine tetraacetic acid (EDTA), 70% ethanol, and absolute ethanol to dry, with pelleting between each step. Cleaned nanofibers were stored in glass containers in absolute ethanol for up to three months.

To crosslink GST N-WASP WWCA to glass nanofibers, nanofibers were treated with 3-aminopropyltriethoxysilane (APTES) (Sigma) and incubated with heterobifunctional cross linker (5 mg/ml maleimide-dPEG12-NHS ester (Sigma) dissolved in chloroform and 0.7% triethylamine for 2h at room temperature. PEG-modified nanofibers were incubated with 10 mM glutathione in phosphate buffered saline (PBS, pH 7.2) for 1h at room temperature. The unreacted maleimide groups were blocked by free cystein (1mM in PBS, pH 7.2). Glutathione-coupled nonafiber was then immersed in the solution of GST-N-WASP WWCA for 1 hour at room temperature, washed with PBS 5 times and immediately used in the experiment [183].

Reconstitution of branch initiation using nanofiber. Glass slides and coverslips were cleaned as previously described [181]. Glass slides and coverslips were blocked overnight in 1% BSA at 4 ℃ and dried in air before use. We placed 16 µl of reaction mixture on a BSA coated slide, covered with a BSA coated coverslip, and sealed the chamber with VALAP (1:1:1 vaseline/ lanolin/paraffin).

Labeled and unlabeled Ca-ATP actin were diluted to the desired labeled fraction, mixed 9:1 with 10x magnesium exchange buffer (10x ME: 10 mM ethylene glycol tetraacetic acid, EGTA, 1 mM $MgCl_2$) and incubated on ice for 2 minutes to form 4x final concentrations of Mg^{2+}-ATP actin. We placed 8 µl of Mg-ATP actin at the bottom of a 1.5 ml Eppendorf tube and added 7 µl

of protein mixtures and 1 µl of GST-N-WASP WWCA coated nanofibers on the side of the tube. Arp2/3 and CP were diluted in nanoparticle storage buffer (10 mM HEPES pH 7.8, 0.1 M KCl, 1 mM $MgCl_2$, 1 mM ATP, 0.1 mM $CaCl_2$, 0.01% NaN_3). We washed both drops together with 16 µl 2x TIRF buffer (2x: 100 mM KCl, 2 mM $MgCl_2$, 2 mM EGTA, 20 mM imidazole, pH 7.0, 200 mM DTT, 0.4 mM ATP, 30 mM glucose, 0.5% 1500 cP methylcellulose, 40 µg/ml catalase, 200 ug/ml glucose oxidase) and placed the reaction mixture in slide-coverslip as described above.

Capped filaments binding to microspheres. Coverslips were coated with 1 mg/ml poly-L-lysine (30 to 70 kDa, Sigma-Aldrich) for 2 minutes, rinsed 3x with deionized water, and dried in air. We polymerized 6 µM (30% Oregon green labeled) Mg-ATP actin in buffer F (buffer G with 10 mM Imidazole pH 7, 50 mM KCl, 1.1 mM $MgCl_2$, 2 mM EGTA) for 10 minutes at room temperature. Actin seeds were diluted 3-fold in buffer F and vortexed at maximum speed for 1 minute to break filaments (Vortex Genie 2, VWR Scientific Products, West Chester, PA.) Capping protein was added to seeds and incubated for 10 - 30 minutes. To capped seeds, we added 4.5 µm diameter GST-WWCA coated microspheres, 1 µM Oregon green labeled Mg-ATP actin monomers, and 1 mg/ml BSA. The reaction was incubated for 10 minutes at room temperature, beads and bound filaments were pelleted by centrifugation at 3000 rpm for 1 min, and the supernatant was removed. The pellet containing beads and bound filaments was gently diluted 16-fold in buffer F, mixed 1:1 with 2x TIRF buffer, and 16 µl was added to a poly-L-lysine coated coverslip. Filaments and beads were observed, respectively, by TIRF or DIC microscopy.

Image acquisition and processing. Actin fluorescence was observed with a 60x 1.49 NA TIRF objective on an Olympus IX2 inverted microscope. Images were captured with a Retiga EXi cooled CCD camera (QImaging) using SlideBook image acquisition software (Intelligent

Imaging Innovations, Inc). All subsequent image-processing steps were performed in ImageJ, available at http://rsbweb.nih.gov/ij. TIRF microscopy images were gamma corrected using a value of between 0.5 and 0.8. An unsharp-mask filter was applied with a radius of 1 to 1.3 pixels and a 60% mask weight. Images were rotated and cropped for publication.

Fluorescence Anisotropy. Anisotropy measurements were made with a filter-based spectrofluometer (Infinite 200 PRO, Tecan, Switzerland). We polymerized 6 μM Mg-ATP actin in buffer F (buffer G with 10 mM Imidazole pH 7, 50 mM KCl, 1 mM $MgCl_2$, 2 mM EGTA) for 10 minutes at room temperature. Actin seeds were diluted 3-fold in buffer F, carefully aliquoted, and mechanically broken by pipetting or vortexing for various times to generate varying concentrations of barbed ends. A 15 μl aliquot of seeds was carefully added to a reaction totaling 150 μl. Fixed rhodamine-labeled N-WASP WWCA concentration (25 nM) were mixed with various concentrations of barbed ends in KMEI buffer (10x: 500 mM KCl, 10 mM $MgCl_2$, 10 mM EGTA, 100 mM Imidazole, pH 7). Rhodamine was excited with polarized light at 540 ± 25 nm and the emitted light was detected at 590 ± 20 nm through both horizontal and vertical polarizers. Measurements were made at 15 s intervals, and the average anisotropy was calculated from 300 seconds, the same time window used to calculate concentration of barbed end. Based on the fact that concentration of ligand (25 nM rhodamine-labeled N-WASP WWCA) is much more than concentration of reactant (100 pM barbed end), the dissociation-equilibrium constants (K_d) were calculated by fitting equation (1) in Kelaidograph.

$$r = r_f + [L] \times r_{max}/(K_d + [L]) \quad (1)$$

where r_f is the anisotropy value of free rhodamine-labeled N-WASP WWCA, [L] is the concentration of ligand (25 nM rhodamine-labeled N-WASP WWCA).

In experiments in which a non-fluorescent ligand (unlabeled N-WASP WWCA) competed with rhodamine-labeled N-WASP WWCA for binding to barbed end, equation (2) was fitted to IC 50. The derived IC50 is used to calculate the dissociation-equilibrium constants (K_d) of unlabeled N-WASP WWCA and barbed end by equation (2).

$$K_i = IC50/ (1 + [C]/K_d) \quad (2)$$

Where K_i is the dissociation-equilibrium constant of competing ligand (unlabeled N-WASP WWCA) and barbed end, [C] is the concentration of competing ligand (unlabeled N-WASP WWCA), K_d is the dissociation-equilibrium constant of rhodamine-labeled N-WASP WWCA and barbed end.

In experiments in which CP competed with rhodamine-labeled N-WASP WWCA for binding to barbed end, two experiment procedures were used. Actin was added to the mixture of CP and rhodamine-labeled N-WASP WWCA, and equation 2 was used to fit the data. Alternatively, or rhodamine-labeled N-WASP WWCA and actin were preincubated for 3 minutes, and CP was added. In the latter case, a binding affinity curve (equation 1) was used to fit the data.

Bulk pyrene-actin spectroscopy assays. To measure the concentration of barbed end used in fluorescence anisotropy experiments, seeded pyrene-actin polymerization assay is used. Actin seeds with various concentrations of barbed ends used in fluorescence anisotropy experiments were placed in the upper row (reaction wells) of a 96 well half area flat bottom plate (Corning) along with 1.6 µl of 100x antifoam (100x: 0.005% antifoam-204, Sigma-Aldrich), 2x initial concentration of Mg KMEI (10x: 500 mM KCl, 10 mM $MgCl_2$, 10 mM EGTA, 100 mM Imidazole, pH 7), and buffer G. We diluted labeled and unlabeled Ca-ATP actin to 30% labeled fraction, mixed 9:1 with 10x ME exchange buffer, and incubated on ice for 2 minutes to form 2x

final concentrations of Mg-ATP actin in the lower row (preparatory wells) of the same plate. We started the reaction by transferring 75 µl of actin monomer mixture from the lower preparatory row to the upper reaction row containing 75 µl in each well for a 150 µl total reaction with a final concentration of 1 µM actin monomer and same dilution of actin seeds (1:10 fold) as in anisotropy experiments. The reaction was gently mixed with a 12-channel pipette and wide tips, and pyrene-actin fluorescence was measured in a Spectra fluorescent plate reader (Tecan, Switzerland) with excitation and emission wavelengths of 364 nm and 407 nm, respectively.

Assuming that the concentration of filamentous pyrenyl-actin was zero at the beginning of the reaction and the polymerization rate was constant for the first 4 min, we used a linear fit of the first 300 s of each polymerization trace to estimate fluorescence intensity at 0 s and subtracted this value. Seeded actin polymerization curves that reached a plateau were used to estimate the final fluorescence intensity for [filament] = 1 - 0.12 = 0.88 µM, assuming a critical concentration of K_C = 0.12 µM [4]. We applied these scaling factors to all curves and obtained polymerization rates from the slope of a 300 s window of data [61].

Results

We used glass nanofibers coated with GST-WWCA domains from N-WASP to model the leading edge in an *in vitro* reconstruction of motility. We previously demonstrated that total internal reflection fluorescence (TIRF) microscopy could distinguish actin architecture in the resulting propulsive actin comet tails [179]. In the present study, we lowered actin, profilin, Arp2/3, and CP concentrations to address the generation of actin filament orientation during the initiation of motility.

We confirmed previous studies that capping protein (CP) addition dramatically affected the orientation of barbed ends and branches nucleated by Arp2/3 [59, 131, 154]. In the absence of CP, actin filaments formed a "fishbone" structure with mother filament "primers" aligned along the nanofiber long axis [59, 131, 154] and daughter filaments growing away from the nanofiber (**Figure 3.1**A, **Figure 3.7**). Photobleaching of growing filaments and subsequent growth of bright filament tips confirmed that daughter barbed ends faced away from nanofiber surface. Addition of capping protein dramatically reoriented daughter barbed ends to face toward the nanofiber surface as previously shown [59, 154]. Given that CP appears to drive the canonical filament orientation found in both motile cells and actin comet tails, we sought to determine this reorientation mechanism.

CP addition led to dissociation of branches from the nanofiber. In the absence of CP, detached branches were rarely observed in the solution (**Figure 3.1**A,D). Upon addition of 10 nM CP, small actin branches appeared in the solution surrounding the nanofiber (**Figure 3.1**B, **Figure 3.8**A). Detached branches followed a Gaussian distribution centered at or near the nanofiber axis (**Figure 3.1**C, **Figure 3.8**B), confirming the nanofiber as the source. Detached branches frequently showed an asymmetrical distribution, with the peak shifted 0.57 μm – 1.56

μm from the nanofiber axis, indicating either asymmetrical branch nucleation or detachment. After an initial nucleation phase (~300 sec), the detached branch population increased linearly. Observations of several nanofibers gave an average detachment rate of 0.0025 ± 0.0019 branches s^{-1} per μm of nanofiber length (N=6), compared to a rate of zero in the absence of CP (N=11) (**Figure 3.1**D). We propose that this dissociation or "shedding" of branches serves as an important step in barbed end reorientation.

Similar to previous findings that WH2 domains capture barbed ends [75, 179], we found that barbed ends of dissociated branches could be recaptured by WWCA coated nanofibers. Attached branches frequently pivoted about a single point either from thermal fluctuations, buffer convection, or drift of the nanofiber along the chamber surface (**Figure 3.2**A). We used these pivot points to determine where branches were tethered and the canonical 70 ºArp2/3 branch to designate filament orientation. Of the pivoting branches, 75% were tethered to the nanofiber at their barbed end, and 25% were tethered at their pointed end branch junction (N=92). Although some mother filaments adhered along their length to the nanofiber long axis to serve as nucleation "primers", we never observed filament pivoting other than at barbed or pointed ends. Pivoting of barbed or pointed ends that were connected to drifting nanofibers indicates that ends were specifically tethered rather than physically trapped between the nanofiber and coverslip. Thus, pivoting likely represented a high-affinity attachment to a single point at the nanofiber surface rather than a summation of several low-affinity side-binding sites along a section of filament, as seen for mother filaments "primers". Given that we only observed end tethering in the presence of CP, we sought to determine whether tethered barbed ends were capped or uncapped.

Analysis of tethered barbed ends showed that these branches remained capped during their attachment period. Tethered branches remain the same length during an average attachment time of 33.7 ± 22.4 sec, (**Figure 3.2**B-C, E, G). When the tethered branch resumed growing, both mother and daughter filaments detached from the nanofiber immediately within an average of 2.9 ± 1.8 sec (**Figure 3.2**D, F-G). Therefore, barbed end capping was always coupled with barbed end attachment to WWCA domain, indicating that CP and WWCA domain might bind to barbed end simultaneously.

Branches tethered at their pointed ends in 10 nM CP were retained for shorter periods than those tethered at their barbed ends. The majority of these pointed end tethers (91.7%) were mother filaments with their barbed ends facing outward (**Figure 3.3**A-B). These were retained at the nanofiber for an average of 7.8 ± 6 sec (N=24). Branch retention times could be extended to 43 ± 23 sec (N=3) if subsequent "granddaughter" filaments were nucleated toward the nanofiber (at 140 ºto the original grandmother filament) and their barbed ends subsequently became attached (**Figure 3.3**C).

We observed an increase in daughter debranching when mother filaments were attached at their pointed ends. For these branches, 37.5% (N=24) of distal daughter filaments detached from the branch junction within 5.25 ± 3.75 sec of their formation (**Figure 3.3**A-B). Debranching was often preceded by flexing of untethered mother and daughter filaments, indicating that thermal fluctuations in the branch angle may play a role in debranching. In contrast, debraching was rarely observed (0%, N=68) when the daughter branch was attached via its barbed end. Together, these results indicate that barbed end attachment to WWCA stabilizes correctly oriented dendritic branches during motility initiation

Given that Co et al [75] found that 200 nM CP appeared to abolish filament attachment to microspheres coated with WASP C-terminus constructs, we sought to determine how CP and WASP family WWCA domains might interact at filament barbed ends. We used similar bead pull-down assays to measure adhesion of pre-polymerized filaments to GST-WWCA coated microspheres in a range of CP concentrations. Addition of CP to polymerizing filaments can dramatically reduce overall filament length and thus filament fluorescence. Rather than measure overall filament fluorescence surrounding a microsphere [75], we counted the number of filaments attached to the bottom half of the microsphere by TIRF microscopy [179]. Even short filaments can be seen by TIRF microscopy [181]. Thus, filament counts report end binding independent of any CP-mediated changes in filament length (**Figure 3.4**A).

We found that CP did not completely abolish barbed end binding to GST-WWCA coated beads. We incubated short fluorescent actin seeds with CP for 10 to 30 minutes to insure capping. Capped seeds were incubated with coated beads and fresh actin monomer for 10 minutes and beads and the captured filaments were then separated by low speed centrifugation. In the absence of CP, TIRF microscopy showed that WWCA coated beads captured 8.7 ± 1.2 (mean $\pm$ S.D.) actin filaments each (**Figure 3.4**A-B). In contrast, albumin coated beads coincidentally overlapped with an average of 0.9 ± 0.3 filaments in control experiments. Addition of 200 nM CP reduced binding to an average of 3.8 ± 0.9 filaments per bead, precisely half-way between the number of filaments counted in the absence of CP and coincidental overlap between bead and filaments. Surprisingly, modest CP concentrations increased the number of filaments captured by WWCA domains, with a peak of 12.8 ± 1.4 filaments captured per bead in 2 μM CP. Thus, CP did not fully inhibit WWCA binding to filaments, and moderate CP concentrations enhanced filament binding to WWCA domains when actin monomers were present.

For CP and WWCA to interact at the barbed end, both would need affinities similar to the barbed end concentration in cells. While WASP WCA domains were shown to have a 600 nM affinity for actin monomers, the barbed end affinities of WASP family proteins have never been measured. We developed a bulk binding assays using fluorescence anisotropy to measure the affinity of N-WASP WWCA domains for barbed ends, independent of its affinity for monomers and filaments. We found that careful mechanical shearing of ends could create a reproducible but variable end concentration from the same total filament length. Actin seeds were polymerized only to near-completion to reduce entanglement, diluted, and mechanically pipetted or vortexed for various times to create variable ends. Seeds were split into two reactions and used immediately. In the first reaction, seeds were mixed with rhodamine tagged WWCA peptides to measure end-binding induced shifts in fluorescence anisotropy. In the second reaction, seeds were added to fresh pyrene-actin monomers to estimate end concentration in the first reaction (**Figure 3.5**A).

End binding assays were validated by several controls. First, the concentration of actin we applied (final 0.2 μM) produced a stable filamentous actin concentration over the time-course of WWCA binding (**Figure 3.9**A-B), indicating that monomer concentrations did not rise appreciably during WWCA binding. Thus, any anisotropic shift due to side binding to filaments or binding to monomer would be near constant with respect to filament shearing. Second, from the 33 nM of free actin monomer in each reaction (**Figure 3.9**C) and the binding affinity of WWCA to monomers of 600 nM [111], only 5.3% of WWCA would be bound to actin monomer. Thus, any increase in anisotropy would be primarily due to filament end binding, rather than monomer binding. Third, to minimize the effect of barbed end annealing, we measured the anisotropy at 5 min after the reaction start, when barbed end annealing rate was greatly

attenuated [184]. Fourth, the initial slopes of seeded pyrene actin polymerization assays used to estimate end concentration were measured over the same timeframe as WWCA binding (**Figure 3.5**A).

Based on anisotropy measurements, we measured an affinity of 14 ± 7.5 pM (N=4) for rhodamine-labeled WWCA binding to barbed end (**Figure 3.5**B). Rhodamine labeling has been shown to increase the binding affinity of WASP to actin monomer and Arp2/3 complex in anisotropy experiment [111]. We therefore used unlabeled WWCA in competition assays with rhodamine labeled WWCA to estimate the unlabeled binding affinity. IC_{50} plots of increasing concentrations of unlabeled WWCA competing with constant rhodamine-WWCA for barbed ends yielded a dissociation constant of 75 ± 13 pM (N=3) for unlabeled WWCA binding to barbed end (**Figure 3.5**C), similar to the 80-100 pM binding affinity of CP to barbed end [61, 185]. Moreover, this binding affinity of WWCA to barbed end was 8000-fold higher than its affinity for actin monomers [111]. The high affinity of WWCA for barbed ends is thus consistent with our observation that GST-WWCA coated nanofibers capture filaments in preference to actin monomers (*not shown*).

To further investigate the relationship between CP, WWCA domains, and barbed ends, we monitored the fluorescence anisotropy of rhodamine-labeled WWCA in the presence of both CP and barbed ends. When CP and rhodamine-WWCA were simultaneously added to constant seeds, CP addition lead to a concentration-dependent reduction in WWCA binding to ends (**Figure 3.5**D), confirming that anisotropy shift represented barbed end binding rather than actin monomer binding. However, even at high CP concentrations, rhodamine-WWCA anisotropy dropped by only 67%, indicating that some WWCA likely remain bound to seeds in high CP. Neglecting the failure of CP to completely eliminate WWCA binding, this CP competition assay

could be used as an IC_{50} experiment to estimate an upper limit to the binding affinity of WWCA for barbed ends. Given that 1.74 nM CP reduced 25 nM rhodamine labeled WWCA binding by 35% (half of the 67% reduction), we estimate an upper limit of 1.2 nM for the affinity of rhodamine-WWCA binding to barbed ends and corresponding 6.4 nM affinity for unlabeled WWCA binding. Thus, the K_d of WWCA binding to barbed ends is at least two orders of magnitude higher than its affinity for actin monomers, and likely a similar order of magnitude as that of CP.

CP competition with WWCA showed a complex dependence on binding order. When competition reactions were allowed to proceed to the half-life for CP dissociation (40 min), increasing CP concentrations had only modest effects on WWCA-anisotropy (**Figure 3.5**E). When the reaction reached equilibrium (10 hrs), increasing CP roughly doubled the anisotropy of WWCA binding to barbed ends (**Figure 3.5**E). To determine whether the increase or decrease is depended upon binding order, we preincubated constant seeds with rhodamine WWCA for 5 minutes prior to adding CP (**Figure 3.5**F). Here, increasing CP concentrations did not decrease WWCA binding, but increased anisotropy in a concentration dependent manner to approximately 140%. Taken together, these experiments confirm that WWCA binds to filament barbed ends with high affinity, and that when WWCA binds first, subsequent CP binding can lock WWCA onto the barbed end.

Discussion

We confirmed that CP has a dramatic effect on the orientation actin branches after their nucleation by Arp2/3. However, single filament analysis of branches showed that the reorientation mechanism is different than previously thought. Akin [59] proposed that WASP family nucleation promoting factors (NPFs) at the membrane could either bind barbed ends or activate Arp2/3. In this model, CP binding to barbed ends frees NPFs to activate Arp2/3 and generate branches. Achard et al [131] proposed that CP decreases the length of mother filament primers. Short primers initiate small, independent branches that eventually connect to form an entangled network with the correct orientation. We propose that CP and NPFs cooperate to tether barbed ends soon after their nucleation. Barbed end capture by WWCA places stress on a nearby branch point that accelerates branch dissociation from NPF. CP binding to WWCA-bound barbed ends enhances this tethering effect. Branches thus "pivot" to face toward rather than away from the leading edge.

We used three separate experimental regimes to show that CP does not entirely inhibit WWCA binding to barbed ends and can enhance WWCA binding at moderate concentrations. (1) TIRF microscopic reconstructions of motility initiation showed that capped barbed ends were quickly captured by WWCA coated nanofibers and resided in this tethered state while capped. Barbed end dissociation from the nanofiber was accompanied by resumption in barbed end growth. (2) Barbed end capture by WWCA coated beads was enhanced by moderate CP and only reduced by half at high CP concentration, even in the absence of Arp2/3 and profilin. (3) Fluorescence anisotropic measurements of WWCA binding showed that WWCA has a high affinity for barbed ends, that high CP concentrations do not abolish WWCA binding, and that if WWCA binds first, CP enhances WWCA binding to the barbed end.

Is there a structural basis for cooperative binding of CP and WWCA to the barbed end? The WH2 (W) domains of N-WASP form short N-terminal amphipathic α-helixes that bind along the hydrophobic cleft of actin subunit between subdomains 1 and 3. The remainder of the WH2 domain binds along the exposed surface of the subunit [114, 186]. CP would need to cover the hydrophobic cleft of both the terminal and penultimate actin subunits to completely block WH2 binding. In a low-resolution 23 Å cryo-electron structure of CP bound to barbed ends, Narita et al [60] proposed that the α-tentacle of CP binds to the inner, acidic interface between the two barbed end actin subunits. The β-tentacle then pivots to bind and cover the hydrophobic cleft at the terminal actin subunit. A molecular dynamics simulation of CP docked to the filament barbed end by Kim et al [187] refined and confirmed the Narita model. Interestingly, the hydrophobic cleft of the penultimate actin subunit is open in the Kim et al refinement, leaving the penultimate subunit of a capped barbed end free to bind WWCA. Overlapping the structure of WH2 bound actin monomer with either barbed end subunit in the Kim et al model of a capped filament (**Figure 3.6**) shows that WH2 binding to the terminal subunit clashes with the β-tentacle. However, WH2 bound to the penultimate actin subunit does not overlap with CP. Thus, simultaneous binding of CP to the terminal actin subunit and WWCA to the penultimate actin subunit is structurally feasible.

We propose that CP competes with WWCA binding at the terminal barbed end subunit, but locks WWCA to the penultimate actin subunit. In support, high CP concentrations reduced WWCA tethering of barbed ends by half in bead binding assays and by two-thirds in anisotropy experiments. Thus, CP likely blocks only one of two WWCA binding sites at the barbed end. How then would CP lock WWCA to penultimate subunit? We showed that WWCA had a high affinity of 75 nM for barbed ends with low concentrations of actin monomers. When

concentrations of actin monomers increased, subsequent monomer addition to barbed end may change this affinity. WH2 binding site partially overlaps with the longitudinal actin dimer interface in the filament [112], and like profilin-actin, WASP-bound actin monomers do not prevent monomer addition the barbed end [188]. To add longitudinal actin subunit to barbed end, WWCA must partially or fully dissociate from the barbed end. WWCA dissociation from the barbed end may therefore be linked to subsequent barbed end elongation (manuscript under review). Thus, WWCA may bind barbed ends with lower affinity due to a fast monomer-addition-coupled WWCA dissociation. When CP is included in this model, monomer addition to barbed end is inhibited and WWCA dissociation will be blocked. The order of this ternary complex formation provides an important clue to the competition between capping and elongation. At the leading edge where exposed WWCA is abundant, WWCA would temporarily tether barbed ends between elongation steps. CP binding to a barbed end with WWCA-bound to the penultimate subunit would then block WWCA dissociation either directly or by preventing further subunit addition to lock WWCA into its high-affinity state. In nanofiber experiments, capped short filaments with an average length of 0.3 μm were nucleated on the nanofiber in all directions. Before capping, many of these growing daughter barbed ends remained within range of the 200 – 700 nm diameter nanofibers for around 7 seconds and likely interacted with WWCA along the surface while growing. CP would also have ample time to form this ternary complex before the barbed end escaped the nanofiber surface.

How would CP-induced barbed end tethering lead to branch detachment? When locked into place by CP, WWCA would bind to barbed end with K_d between 75 – 6400 pM, much tighter than its affinity of 900 nM for Arp2/3 at the branch point [111]. Consequently, as filaments fluctuated from thermal forces, buffer convection, or sibling growth, the lower affinity branch

point attachments would be more vulnerable to WWCA dissociation than high affinity barbed end attachments. Pointed end detachment and barbed end tethering would thus "pivot" the newly nucleated branch to face the nanofiber. In support, we measured 3-fold more branched filaments tethered to nanofibers at their barbed end than at their pointed end branch points. This ratio is likely a consequence of residence times. Branches connected at their barbed ends remained tethered to nanofibers longer than branches tethered at their pointed ends/branch junctions. We note that barbed end tethering also stabilized daughter filaments against debranching from mother filaments. Thus, a portion of branch shedding may be due to complete dissociation of the Arp2/3-mother-daughter branch complex.

When taken together, these experiments point to the following model for barbed end generation and orientation at the leading edge. (1) Arp2/3 nucleates new daughter filaments from short, capped mother filaments. (2) Daughters with barbed ends facing away from the leading edge are likely to either debranch or untether from their pointed end. (3) Nucleation of a forward facing granddaughter filament may temporarily stabilize its rearward facing grandmother against un-tethering. (4) Daughters with barbed ends that face toward or parallel to the leading edge make temporary contacts with nearby exposed WWCA domains. (5) CP binding to a WWCA-tethered barbed end temporarily "locks" WWCA onto the barbed end. (6) Thermal filament fluctuations favor the detachment of WWCA tethers from the branch point over tethers to barbed ends. (7) The branch pivots around its barbed end tether to face the leading edge. (8) Tethered barbed ends may either detach from WWCA or WWCA attachment speeds uncapping. (9) Untethered and capped barbed ends are "shed" from the leading edge to join the dendritic network. (10) Uncapped barbed ends resume growth, become untethered, but remain in a proper orientation to direct the force of polymerization against the membrane.

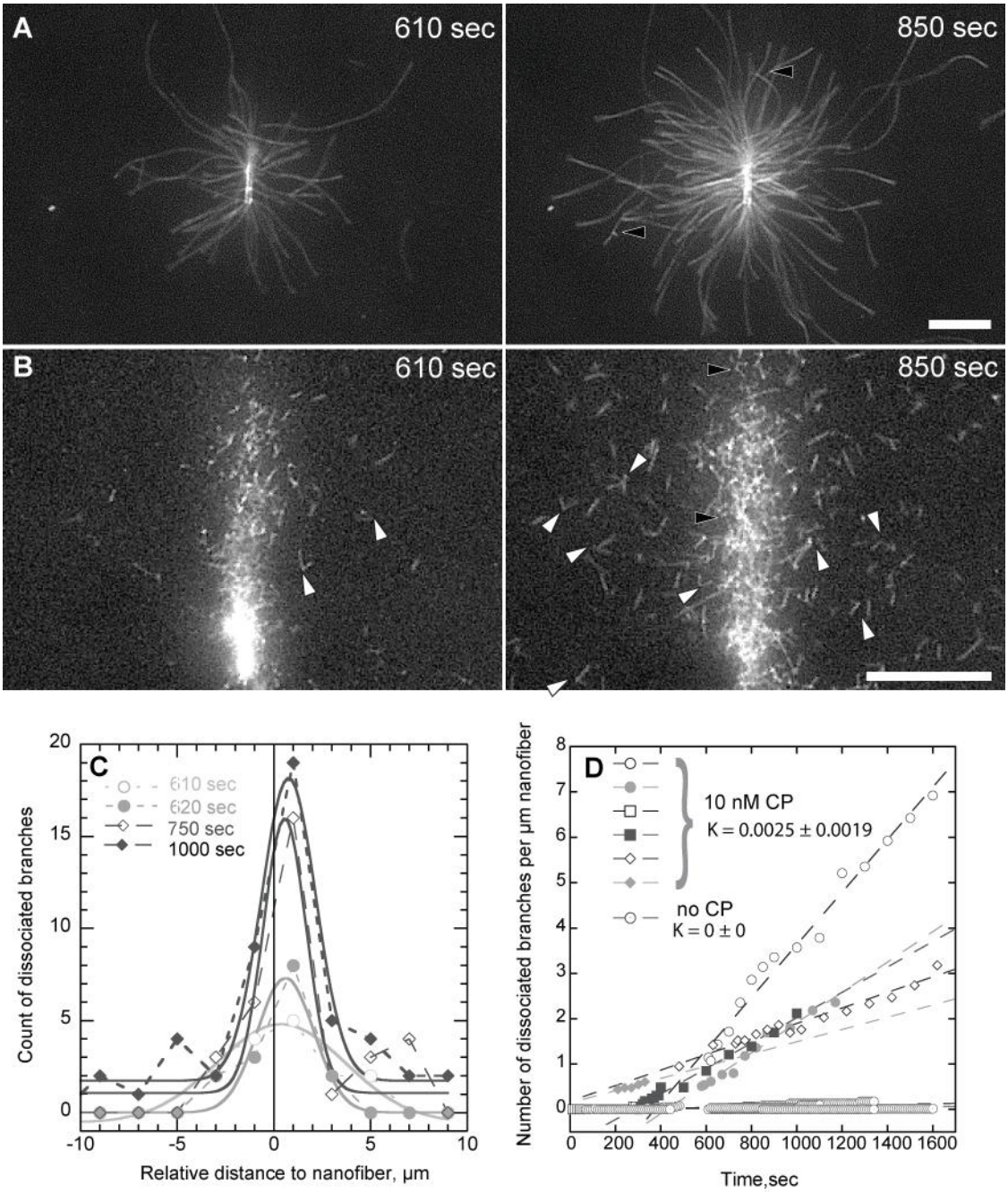

Figure 3.1. Branches dissociate from GST-WWCA coated nanofiber.

Conditions: 1.5 µM (8% labeled) actin, 2 µM profilin, 10 nM Arp2/3, CP as indicated, 10 µM GST-WWCA covalently linked to glass nanofibers, buffer including 10 mM imidazole, pH 7.0, 50 mM KCl, 1 mM MgCl2, 1 mM EGTA, 100 mM DTT, 0.2 mM ATP, 50 µM CaCl2, 15

mM glucose, 20 μg/ml catalase, 100 μg/ml glucose oxidase, 0.25% CP1500 methylcellulose at 25 ℃. **(A)** In the absence of CP, detachment of branches from the nanofiber was rarely observed. Barbed ends (black arrowhead) were growing away from nanofiber surface. **(B)** When concentration of CP was increased to 10 nM, branches detached from the nanofiber surface (dashed outline). Barbed ends were either free in solution (white arrowheads) or attached to nanofiber (black arrowheads). **(C)** Histogram showing the distribution of detached branches along the horizontal axis of nanofiber in (B). The markers represent count of branches in each bin (Y-axis) and midpoint value of each 2 μm bin (X-axis). The distribution of detached branches fits with Gaussian distribution (solid line) with R2 value ranging from 0.94 to 0.97. **(D)** Count of detached branches per μm nanofiber over time in the absence and presence of 10 nM CP. Detached branches were counted within 10 μm distance to nanofiber at both sides. The counting area was 20 μm × the length of each nanofiber. To normalize the data, the count of detached branches was divided by the length of nanofiber. Linear regression (dashed lines) was used to obtain each slope. S.D. was from 11 independent experiments (CP = 0) and 5 independent experiments (CP = 10 nM). Scale bar, 5 μm.

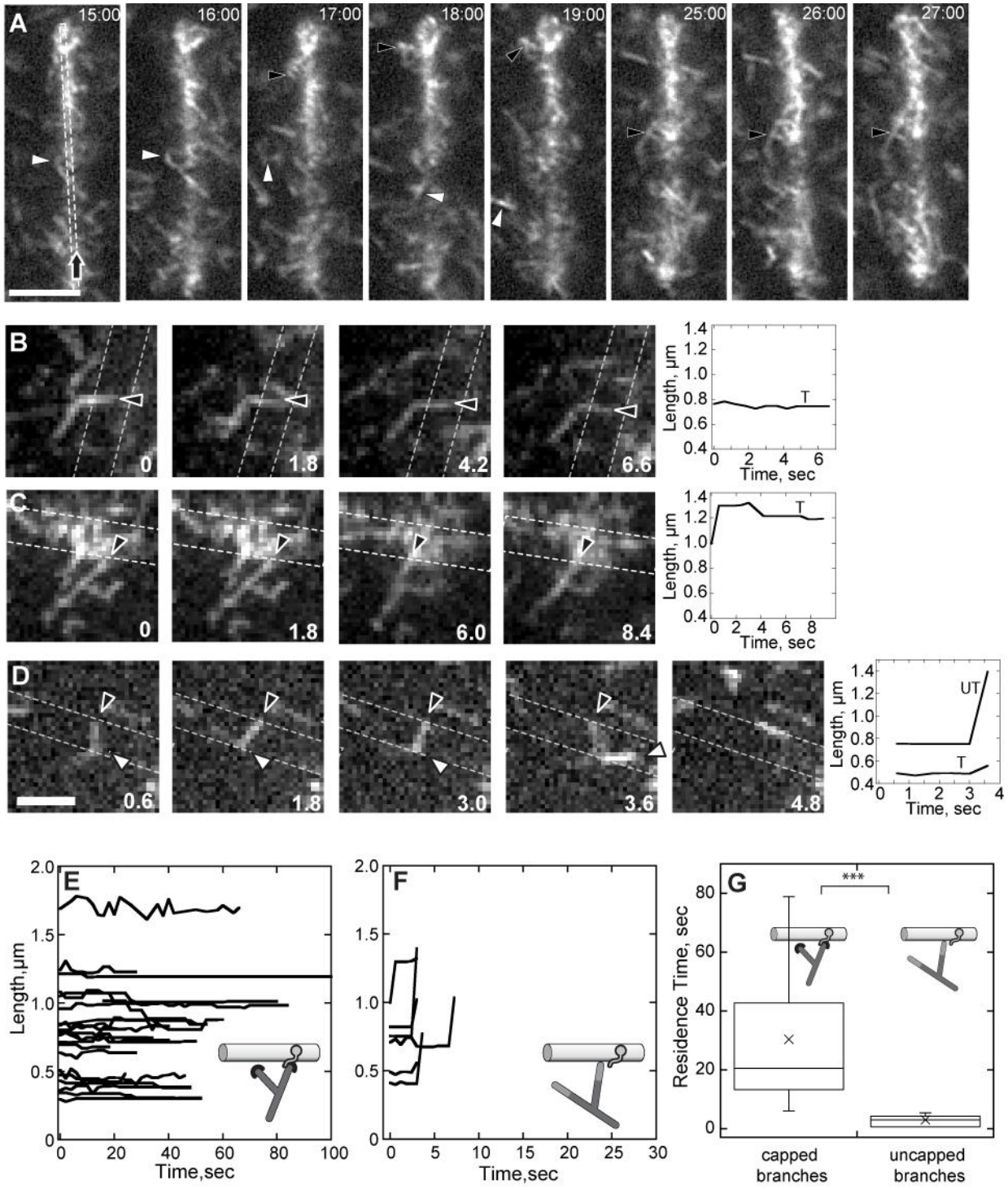

Figure 3.2. Capped barbed end attach to GST-WWCA coated nanofiber.

Conditions: 1.5 μM (8% labeled) actin, 2 μM profilin, 10 nM Arp2/3, 10 nM CP, 10 μM GST-WWCA covalently linked to glass nanofiber, buffer as described in Figure **3.1**. **(A)** Branches pivoted around tethered barbed end (*black arrowheads*) as the nanofiber drifts (*dashed outline*) in 10 nM CP. **(B)** An example of branch that stopped growing while attached to nanofiber via its barbed end. Graph (*right*) shows the length trace of the tethered filament. **(C)** An example of branch that "hopped" at the nanofiber via its barbed end. Graph (*right*) shows the length trace of the tethered filament. The length increase accompanied rapid detachment of the barbed end from its original tethering site, while the stable length was coupled with barbed end attachment. **(D)** An example of branch that originally tethered to the nanofiber. The branch detached from the nanofiber immediately after the elongation of barbed end. Graph (*right*) shows the length trace of two filaments in the branch. **(E)** The length traces of branches that tethered to nanofiber. X-axis shows the residence time of branches on nanofiber. Tethered branches stopped elongation, indicating the binding of CP. **(F)** Length traces of branches that resumed elongation. X-axis shows the residence time of branches on nanofiber. The branch detached from the nanofiber once barbed ends resumed elongation, indicating uncapping. **(G)** Boxplot showing the residence time on nanofiber of capped branches and uncapped branches. The average retention time is shown in (×). Scale bar, 1 μm. Time, sec.

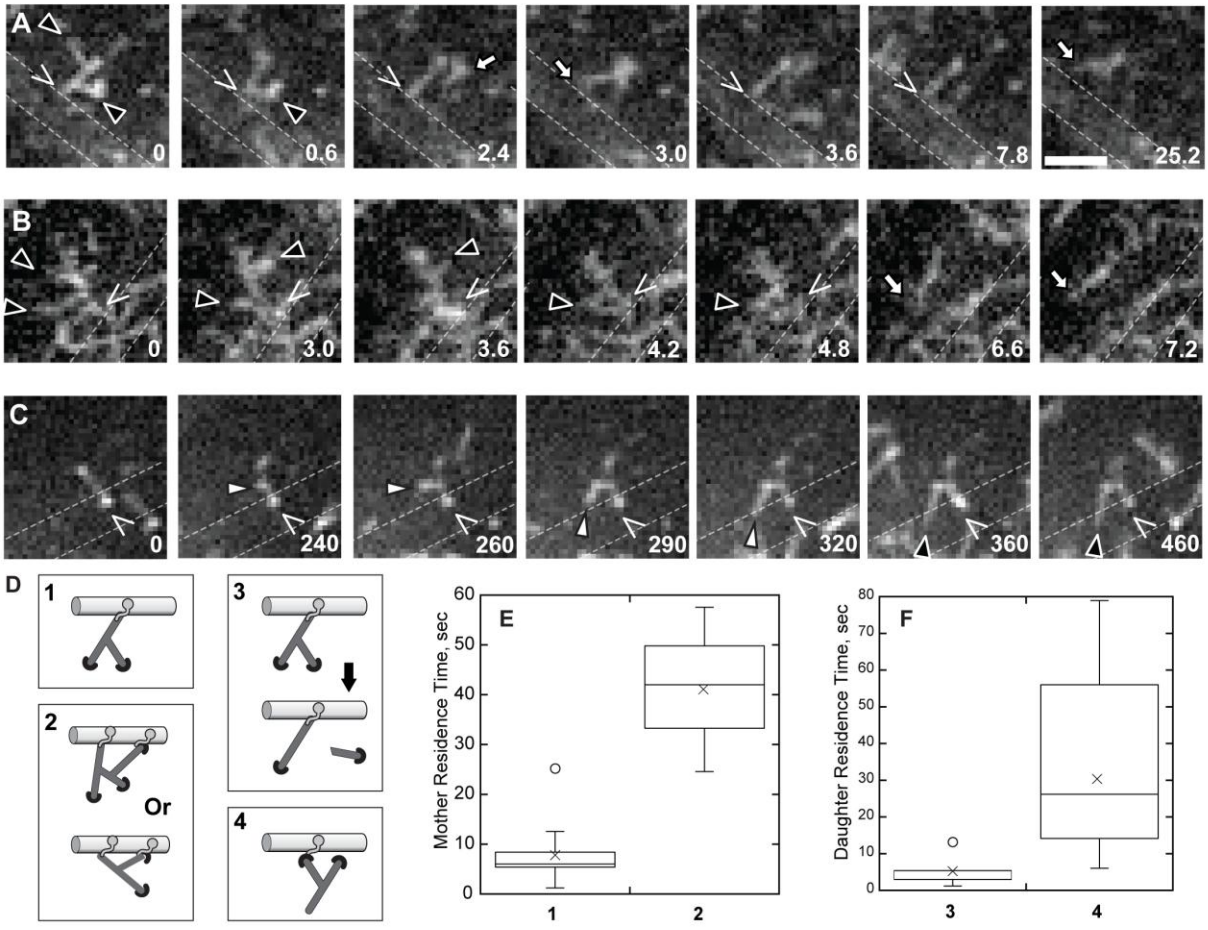

Figure 3.3. Barbed end tethering to WWCA domain slows debranching rate.

Conditions: 1.5 µM (8% labeled) actin, 2 µM profilin, 10 nM Arp2/3, 10 nM CP, 10 µM GST-WWCA covalently linked to glass nanofiber, buffer as described in Figure **3.1**. **(A-B)** Branches tethered to nanofiber via mother filaments point ends (^). Untethered daughter filaments (*black arrowhead before dissociation, white arrow after dissociation*) dissociated from mother filaments. **(C)** New branch was nucleated, elongated, and was tethered to nanofiber via barbed end. Note that although mother filament was attached to nanofiber via point end (^), daughter filament (*black arrowhead*) was reoriented with barbed end growing toward nanofiber. . **(D)** Illustrations of observed branch attachments (1-2) or daughter debranching (3-4): mother

filaments tethered via pointed ends with free daughter barbed ends (1) or daughters or granddaughters barbed ends tethered to the nanofiber (2); debranching of daughter filaments with untethered (3) or tethered (4) barbed ends. **(E)** Boxplot of residence times of mother branches tethered via pointed ends with free or attached daughter or granddaughter barbed ends. Numbers refer to illustrations in (D). (**F**) Boxplot of branch stability for untethered and tethered daughter branches. Numbers refer to illustrations in (D). Average retention times are shown (×). Scale bar, 1 μm. Time, sec.

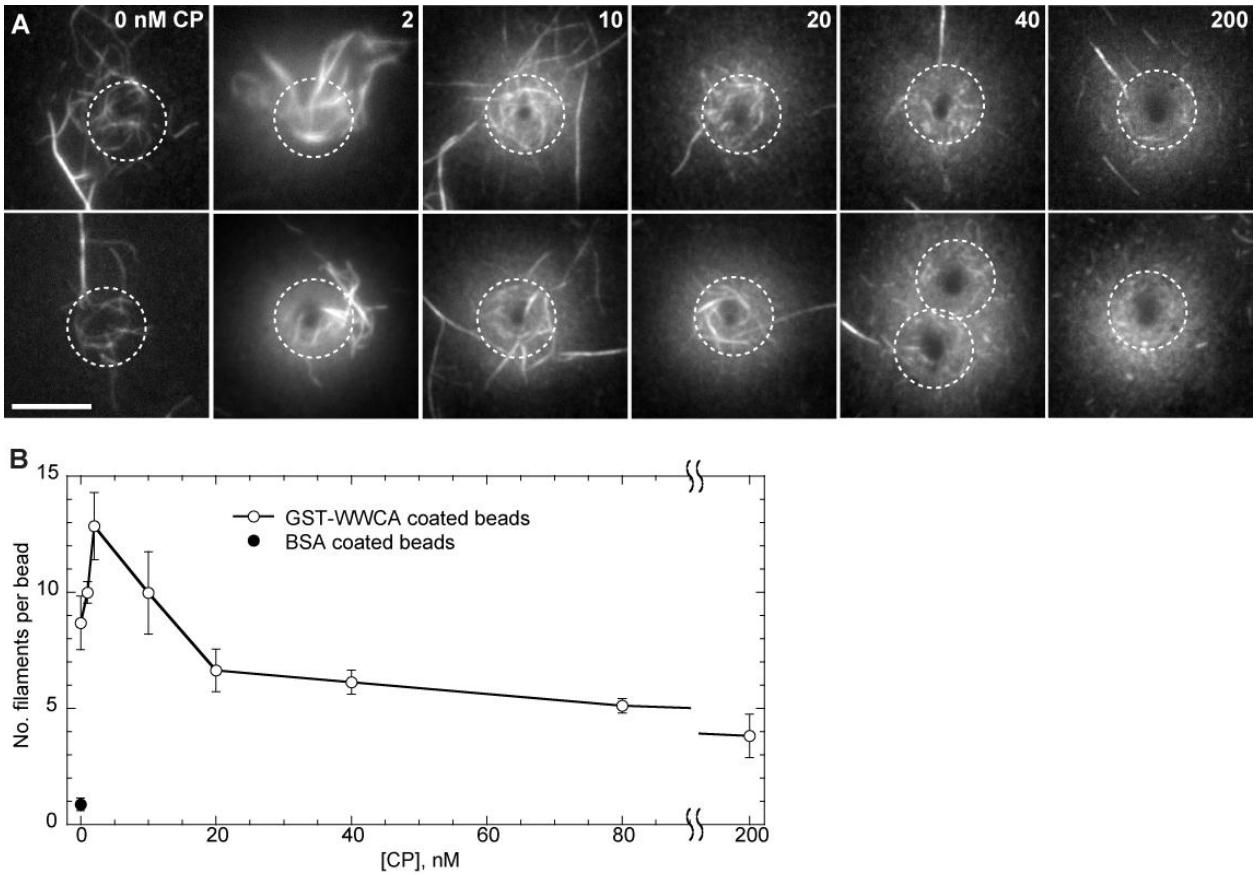

Figure 3.4. CP can enhance filament tethering to WWCA domains.

Conditions: 6 μM (30% labeled) Mg-ATP actin seeds incubated with indicated final concentration of CP for 10 - 30 minutes. Capped seeds were incubation with GST-WWCA coated microspheres for 10 minutes, centrifuged, resuspended in TIRF buffer, and imaged on poly-lysine coated coverslips. **(A)** TIRF microscopy images of actin filaments and bundles attached to the bottom of coated microspheres. The number of actin filaments and bundles crossing the bead boundary (dashed circle) were counted for each bead. Bundles of unknown filament number were scored as two filaments. **(B)** Count of average number of filaments per bead as a function of CP concentration (○). Error bars show S.D. from three independent experiments. Number of filaments overlapping with BSA coated control microsphere is shown for reference (●).Scale bar in A is 5 μm.

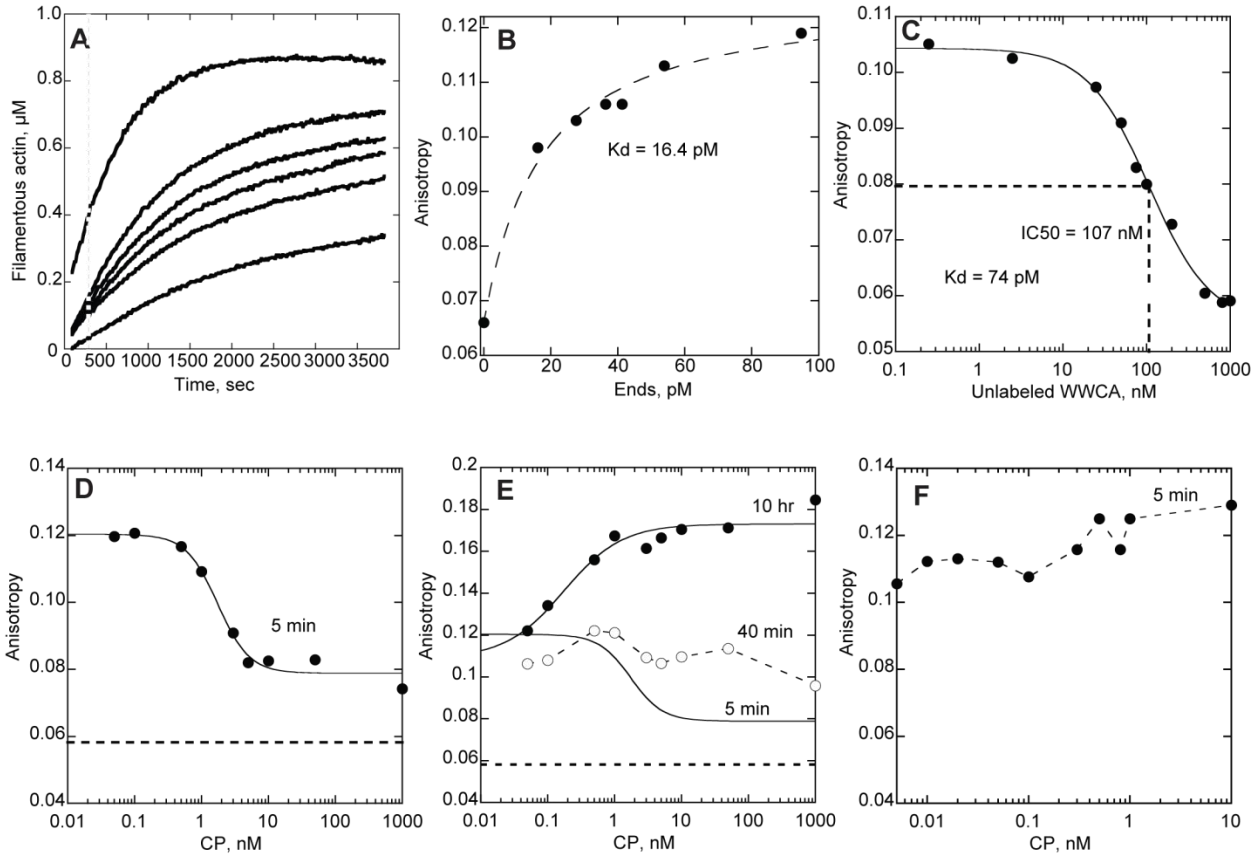

Figure 3.5. WWCA domain binds to barbed end with high affinity, and CP enhances WWCA domain binding to barbed end.

Conditions: 6 µM Mg-ATP actin seeds polymerized for 10 minutes, diluted 3-fold with F buffer, and vortexed for various time to generate constant filamentous actin but various barbed ends. 15 µl of actin seeds were added to 150 µl F buffer with or with no labeled, unlabeled WWCA or CP. Pyrene-labeled actin polymerization assay and fluorescent anisotropy measurement were performed in parallel to measure the barbed end concentrations and binding affinity, respectively. **(A)** The concentrations of barbed ends were measured by pyrene labeled actin polymerization assay. From bottom to top, actin seeds were used directly, pipetted for 6 times, touch vortexed, vortexed for 1 second, vortexed for 30 seconds, and vortexed for 60

seconds. **(B)** Fluorescent anisotropy measurement of binding affinity of rhodamine-labeled WWCA to barbed end. 25 nM rhodamine-labeled WWCA was mixed with actin seeds with various end concentrations. Same batch of actin seeds were used in (A) and (B). Curve shows best fit of equation (1) in the methods to yield an average dissociation constant of 14 ± 8 pM from four independent experiments. **(C)** Competition between unlabeled WWCA and rhodamine-labeled WWCA for binding to barbed end from one experiment. Various concentrations of unlabeled WWCA competed with 25 nM rhodamine labeled WWCA to bind with barbed ends. Actin seeds were prepared as described and vortexed for 60 seconds. Curve shows an IC50 fit (equation 2) yielding a K_i. The K_i is used in equation (3) to yield a dissociation constant of 75 ± 13 pM from three independent experiments. **(D-E)** Competition between CP and rhodamine-labeled WWCA for binding to barbed end at 5 min **(D)**, 40 min and 10 hr **(E)**. Curve *(solid line)* shows the initial IC 50 fit (5 min) from equation (1) for the 5 min and 10 hr curves. Actin seeds were added to the mixture of various concentrations of CP and 25 nM rhodamine-labeled WWCA. Actin seeds were prepared as described and vortexed for 60 secconds. CP competes with rhodamine-labeled WWCA for binding to barbed end at the beginning of reaction, and eventually CP enhances the WWCA binding to barbed end. **(F)** CP enhances WWCA binding to barbed end in a concentration dependent manner. Actin seeds were prepared as described and vortexed for 60 seconds. 25 nM rhodamine-labeled WWCA and actin seeds were preincubated for 3 minutes. Various concentrations of CP were then added to the mixture.

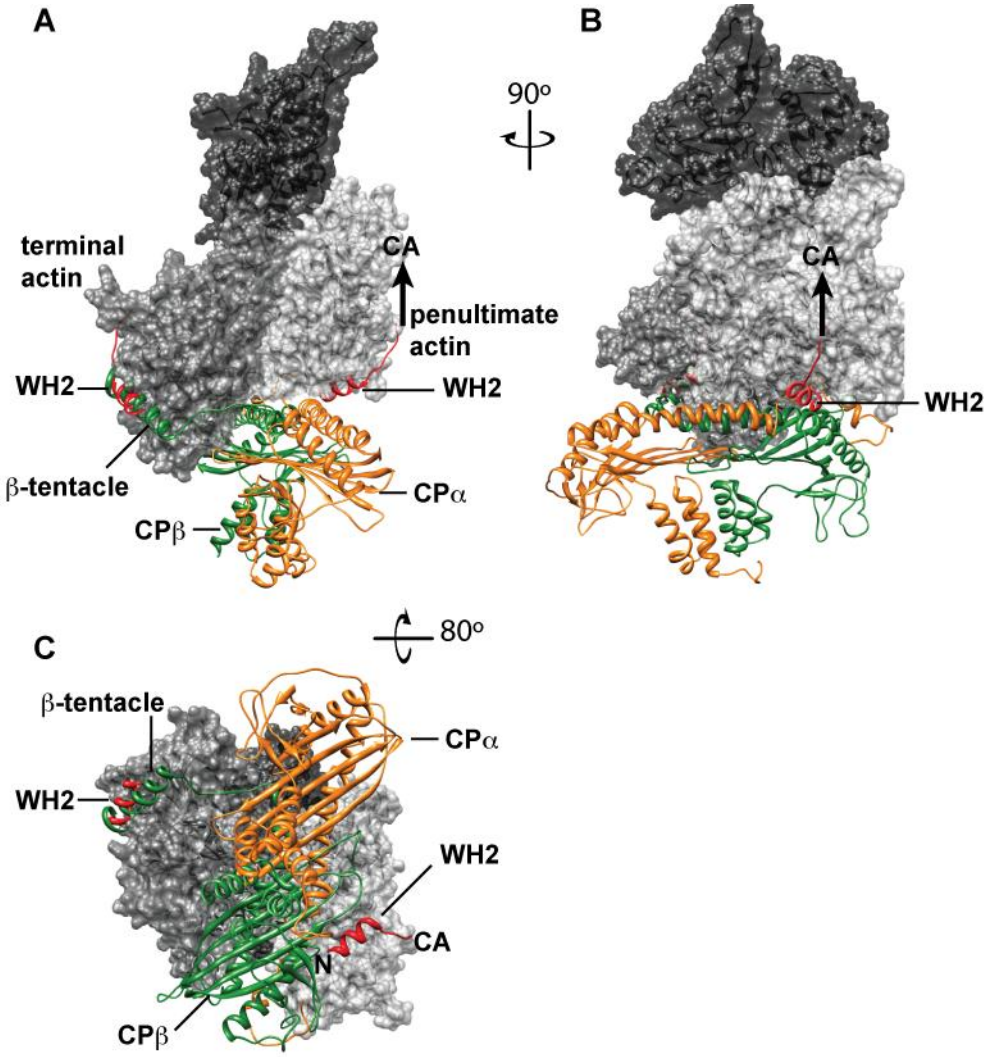

Figure 3.6. Structural comparison of CP and WH2 binding to the filament barbed end.

Molecular dynamics refinement structure of capping protein α (orange) and β (green) subunits docked to the barbed end of an actin filament (gray) from Kim *et al* [187]. The structure of WH2 domains (red) bound to an actin monomer (PDB 2A3Z) from Chereau *et al* [114] was matched to both the terminal actin subunit and the penultimate actin subunit of the filament barbed end. **(A)** While the β-tentacle of CP overlaps with the WH2 binding site at the terminal

actin subunit, the WH2 binding site at the penultimate subunit remains free in the CP bound filament. **(B)** Rotation showing binding of WH2 (red) on the penultimate actin subunit. The C-terminal Central and Acidic (CA) domains of WASP family activators continue toward the pointed end of the actin subunit. **(C)** View of the barbed end of the filament. The N-terminus (N) of the WH2 domain at the penultimate subunit continues to the poly-proline region and membrane binding domains in WASP.

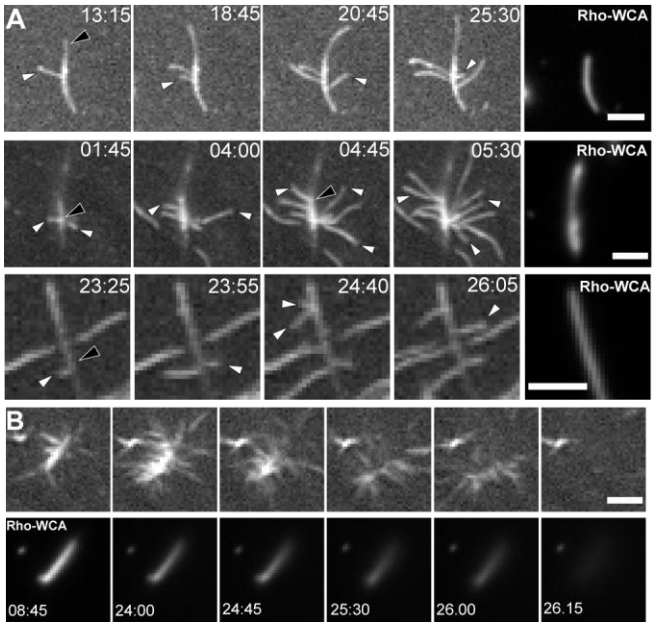

Figure 3.7. Architecture of Arp2/3 nucleated branch network in low [CP].

Condition: 2 µM (8% labeled) Mg-ATP actin, 3 µM profilin, 500 nM bovine Arp2/3, 2.5 nM *Mm*CP, nanofibers coated with 10 µM GST-WCA from N-WASP,buffer as described in Figure**Figure 3.1**. **(A)** In low, 2.5 nM CP and high, 500 nM Arp2/3, mother filaments (black arrowheads indicate barbed ends) growing along nanofibers coated with rhodamine labeled GST-WCA (Rhodamine-WCA) generated daughter filaments (white arrowheads) with barbed ends growing away from the nanofiber surface. Branch detachments from the nanofiber were never observed in low CP and high Arp2/3. **(B)** Nanofibers were not permanently attached to the chamber bottom. In low viscosity buffers (no methylcellulose), growth of barbed ends away from the nanofiber surface provided sufficient force to lift nanofibers away from the surface. Scale bar, 1 µm.

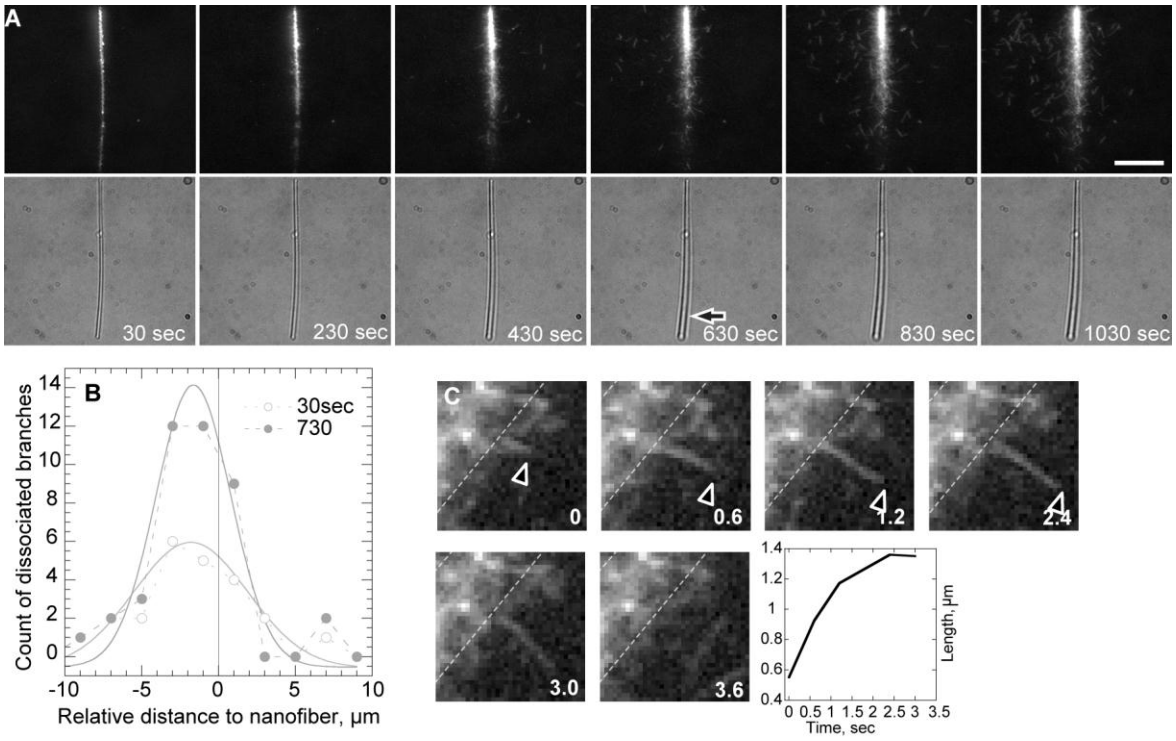

Figure 3.8. More example of branches dissociating from GST tagged N-Wasp WWCA coated nanofiber.

Condition**:** 1.5 µM (8% labeled) actin, 2 µM profilin, 10 nM Arp2/3, 10 nM CP, 10 µM GST-WWCA covalently linked to glass nanofiber, buffer as described in Figure **3.1**. **(A)** Branches detached from the nanofiber surface in the presence of 10nM CP *(top)*. Part of nanofiber detached from the chamber bottom *(bottom)* . **(B)** Histogram showing the asymmetric distribution of detached branches along the horizontal axis of nanofiber in (A). The markers represent count of branches in each bin (Y-axis) and midpoint value of each bin (X-axis). 0 at X-axis represents the position of nanofiber. Bin size: 2 µm. The distribution of detached branches fits with Gaussian distribution (*solid line*). **(C)** An example of filament growing away from nanofiber surface, been capped *(black arrowhead)* and dissociated from nanofiber.

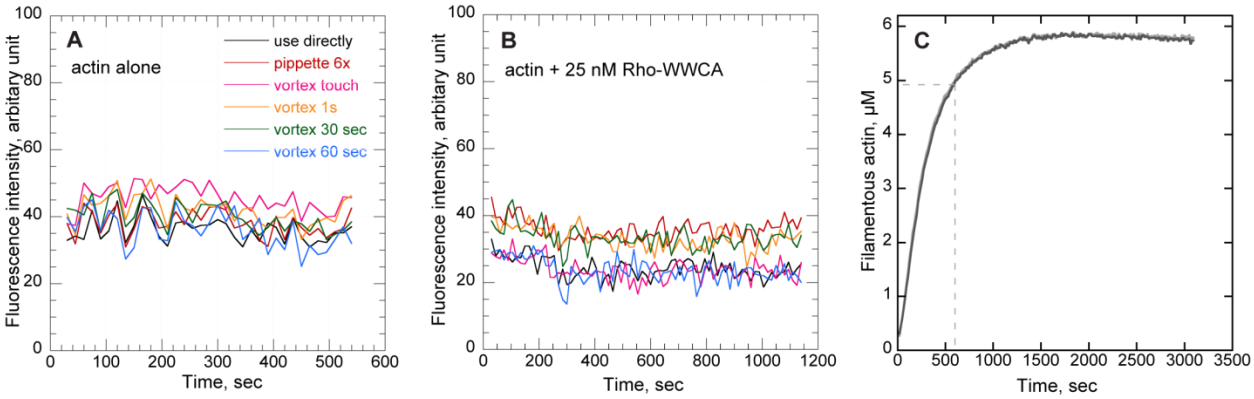

Figure 3.9. Filamentous actin seed used in fluorescence anisotropy remains constant over time.

Condition: 30% pyrene-labeled 6 µM actin polymerized for 10 minutes, diluted 3 fold with F buffer, and mechanically sheared for various time in absence of presence of 25 nM rhodamine-labeled WWCA. The seeds were further diluted to the same concentration used in fluorescence anisotropy experiments. Fluorescent signal was then monitored using a Spectra fluorescent plate reader for (A-B). **(A)** Concentrations of filamentous actin remain constant over 10 minutes in the absence of WWCA. **(B**) Concentrations of filamentous actin remain constant over 20 minutes in the presence of 25 nM rhodamine-labeled WWCA. **(C)** The polymerization course of 30% pyrene-labeled 6 µM actin. The concentrations of filamentous actin and free actin monomer at 10 minutes were calculated as described in the methods.

Chapter 4 Conclusions and Future Directions

Conclusions

The work presented here addressed two fundamental questions in actin dynamics at the leading edge membrane: (1) how filament networks remain attached to the leading edge as they grow, and (2) how polarized actin networks are initiated and maintained with most barbed ends facing toward the leading edge.

In Chapter 2, by reconstructing actin-based motility using nanofiber or bead in a minimum set of purified proteins, I found that physiological concentration of divalent cation are sufficient to bundle actin filament. Filament bundles attached to N-WASP coated particle processively as the bundles grew. Several different types of bundling factors, including extra Mg^{2+}, di-lysine^{2+}, and the crosslinker protein fascin, were added to a system with no bundling activity on its own. My experiments showed that filament bundling is essential to maintain attachments between filaments barbed ends and moving surfaces. We proposed a model whereby bundles cooperate efficiently to maintain barbed end attachment. One filament in a bundle is attached to WCA, while sister filaments are free to either polymerize by subunit addition, bind to a nearby free WCA, or bind to a profilin-actin bound WCA. The force of polymerization is efficiently transmitted through the stiff bundle to tethered barbed ends and promotes tether dissociation.

In Chapter 3, to examine how actin filament orientation was generated, I lowered actin, profilin, Arp2/3 and CP concentrations to observe individual filament dynamics at the initiation stage of nanofiber motility. I observed dissociation of branches from nanofiber in the presence of CP for the first time. Branches were either free in the solution or tethered to nanofiber via their barbed ends. The latter case is the hallmark for reorientation of barbed end toward the nanofiber.

By carefully examining and quantifying the tethering of branches to nanofiber, I found that barbed end retention was always coupled to end capping. This result indicated that CP and WWCA might bind simultaneously to filament barbed ends. Bead pull-down assay and fluorescence anisotropy experiments further confirmed the ternary structure. I developed a novel assay to measure the binding affinity of WWCA to barbed end by fluorescence anisotropy. The high affinity (K_d = 80 pM) enables WWCA to rapidly capture and hold barbed end. We proposed that simultaneous binding of CP and WWCA to barbed ends is essential to the establishment of filament orientation at the leading edge. Rapid CP association limits growth of Arp2/3 nucleated barbed ends away from the leading edge. Subsequent N-WASP binding and tethering of capped barbed ends directs thermal forces from actin fluctuations toward tethered branch junctions. Thus branch junctions detaches from immobilized N-WASP on nanofiber, pivoting the branch to point in the direction of productive motility. Cooperative CP/N-WASP binding thus presents a new mechanism that refines our understanding of dendritic nucleation at the leading edge.

Combining the findings in Chapter 2 and 3, we propose a mechanism whereby CP and WWCA cooperate to initiate barbed end orientation near leading edge, and bundling of filaments further stabilizes the filament direction and maintains attachments between growing actin filaments and the leading edge. In support of this, one of my lab colleagues, Nimisha Khanduja, found that like Ena/VASP and formin family proteins, N-WASP WWCA domains can processively attach to growing barbed bundles and increase their diffusion-limited elongation rate in the absence of Arp2/3 complex.

Future Diretions

To further confirm the proposed mechanism, future lab members will work on providing more direct microscopic evidence and testing the model in the cell. The motility reconstitution system I developed will provide a powerful tool to study actin-based motility. The work is not complete, and several other regulating proteins could be tested by using this method.

Using two-color TIRF to confirm CP and WWCA binding to barbed ends simultaneously.

To provide more direct microscopic evidence for the terniary structure at barbed ends, single molecular observation with multi-colored TIRF will be invaluable to investigate the relationship between actin monomer, WWCA, CP and filament barbed end. As the first step, with proper dilution, the dynamic localization of rhodamine-labeled N-WASP WWCA at Oregon green 488-labeled barbed end will be tested to confirm WWCA binding to barbed ends. The next step will be to test the localization of rhodamine-labeled N-WASP WWCA at capped barbed ends. We expect that rhodamine-labeled N-WASP WWCA will processively attached to both free and capped barbed ends. Dissociation constants could be further calculated to verify the synergistic binding. To test how common these mechanisms are, future lab members will investigate longer constructs of N-WASP and other NPFs, such as ActA and WASP using the microscopic and fluorescence anisotropic techniques I developed.

Determine whether monomer addition leads to partial dissociation of WWCA from barbed end.

Free barbed ends bound with rhodamine-labeled N-WASP WWCA can be formed and tethered to the coverslip surface of a flow cell. Extra actin monomers would be removed by buffer exchange and various concentration of Oregon green 488-labeled actin monomers added. We expect that rhodamine-labeled N-WASP WWCA will dissociate from barbed ends with

increased concentrations of actin monomers. The frequencies of WWCA bound to the side of filaments would be also increased. Because CP prevents monomer addition to barbed ends, similar experiments will be performed using capped barbed ends bound with rhodamine-labeled N-WASP WWCA. We expect that CP will attenuate monomer-coupled WWCA dissociation from barbed ends. This experiment would help to clarify the question of whether the attachment of WWCA on barbed end influences barbed end elongation.

Testing branch reorientation and bundling dependent attachment *in vivo*.

To test the bundling dependent attachment model, binding ligands of physiological polycations, such as spermine binding protein (Sbp), will be overexpressed in fibroblast cells to reduce filament bundling. Fluorescent speckle microscopy and TIRF microcopy will be combined to observe the actin dynamics in the cell. We expect that reduction of polycations will reduce protrusions and attenuate actin filament distribution at the leading plasma membranes. If no dramatic effect was observed, further knockdown of specific actin bundling proteins, such as fascin, α-actinin, will be performed to reduce filament bundling.

To test the mechanism of barbed end reorientation in vivo, cells with be transfected with constructs containing CP with mutations of the β-tenacle or mutated WH2 domain of WWCA that prevents barbed end binding. Electron microscopy (EM) will be used to observe the distribution of barbed ends decorated with myosin S1. We expect to observe a reduction of barbed ends near the plasma membranes.

Role of coronin in reorganizing the dendritic actin network.

Coronin is an actin depolymerization factors that plays an important role in regulating turnover of actin filaments. Coronin 1B limits Arp2/3-dependent actin branches through inhibition of Arp2/3 docking or facilitating debranching [189]. Coronin 1B can replace Arp2/3 at

actin branches and create more flexible branches. We will test whether coronin facilitates the barbed end reorientation at the leading edge by enhancing Arp2/3 dissociation and debranching. Alexa 568-labled coronin 1B will be added in an *in vitro* reconstructed system in the absence of CP. We expect to see enhanced debranching and filament dissociation from immobilized NPF on nanofiber. We will determine whether barbed ends tethering on NPF-coated nanofiber were observed. If no barbed end attachment is observed, a suboptimal concentration of CP could be added to limit the length of filament and help WWCA to capture barbed ends.

References

1. Le Clainche, C. and M.F. Carlier, *Regulation of actin assembly associated with protrusion and adhesion in cell migration.* Physiol Rev, 2008. **88**(2): p. 489-513.
2. Pollard, T.D. and G.G. Borisy, *Cellular motility driven by assembly and disassembly of actin filaments.* Cell, 2003. **112**(4): p. 453-65.
3. Sept, D. and J.A. McCammon, *Thermodynamics and kinetics of actin filament nucleation.* Biophys J, 2001. **81**(2): p. 667-74.
4. Pollard, T.D., *Rate constants for the reactions of ATP- and ADP-actin with the ends of actin filaments.* J Cell Biol, 1986. **103**(6 Pt 2): p. 2747-54.
5. Blanchoin, L. and T.D. Pollard, *Hydrolysis of ATP by polymerized actin depends on the bound divalent cation but not profilin.* Biochemistry, 2002. **41**(2): p. 597-602.
6. Blanchoin, L. and T.D. Pollard, *Mechanism of interaction of Acanthamoeba actophorin (ADF/Cofilin) with actin filaments.* J Biol Chem, 1999. **274**(22): p. 15538-46.
7. Melki, R., S. Fievez, and M.F. Carlier, *Continuous monitoring of Pi release following nucleotide hydrolysis in actin or tubulin assembly using 2-amino-6-mercapto-7-methylpurine ribonucleoside and purine-nucleoside phosphorylase as an enzyme-linked assay.* Biochemistry, 1996. **35**(37): p. 12038-45.
8. Pollard, T.D., *Regulation of actin filament assembly by Arp2/3 complex and formins.* Annu Rev Biophys Biomol Struct, 2007. **36**: p. 451-77.
9. Machesky, L.M., et al., *Purification of a cortical complex containing two unconventional actins from Acanthamoeba by affinity chromatography on profilin- agarose.* J Cell Biol, 1994. **127**(1): p. 107-115.
10. Svitkina, T.M. and G.G. Borisy, *Arp2/3 complex and actin depolymerizing factor/cofilin in dendritic organization and treadmilling of actin filament array in lamellipodia.* J Cell Biol, 1999. **145**(5): p. 1009-1026.
11. Higgs, H.N. and T.D. Pollard, *Regulation of actin filament network formation through ARP2/3 complex: activation by a diverse array of proteins.* Annual review of biochemistry, 2001. **70**: p. 649-676.
12. Domann, E., et al., *A novel bacterial virulence gene in Listeria monocytogenes required for host cell microfilament interaction with homology to the proline-rich region of vinculin.* The EMBO Journal, 1992. **11**(5): p. 1981-90.
13. Loisel, T.P., et al., *Reconstitution of actin-based motility of Listeria and Shigella using pure proteins.* Nature, 1999. **401**(6753): p. 613-616.
14. Zalevsky, J., I. Grigorova, and R.D. Mullins, *Activation of the Arp2/3 complex by the Listeria acta protein. Acta binds two actin monomers and three subunits of the Arp2/3 complex.* J Biol Chem, 2001. **276**(5): p. 3468-75.
15. Gournier, H., et al., *Reconstitution of human Arp2/3 complex reveals critical roles of individual subunits in complex structure and activity.* Mol Cell, 2001. **8**(5): p. 1041-52.
16. Wiesner, S., et al., *A biomimetic motility assay provides insight into the mechanism of actin-based motility.* J Cell Biol, 2003. **160**(3): p. 387-398.
17. Goley, E.D., et al., *Critical conformational changes in the Arp2/3 complex are induced by nucleotide and nucleation promoting factor.* Mol Cell, 2004. **16**(2): p. 269-79.

18. Dayel, M.J., E.A. Holleran, and R.D. Mullins, *Arp2/3 complex requires hydrolyzable ATP for nucleation of new actin filaments.* Proc Natl Acad Sci U S A, 2001. **98**(26): p. 14871-6.
19. Blanchoin, L., et al., *Direct observation of dendritic actin filament networks nucleated by Arp2/3 complex and WASP/Scar proteins.* Nature, 2000. **404**(6781): p. 1007-11.
20. Padrick, S.B., et al., *Arp2/3 complex is bound and activated by two WASP proteins.* Proc Natl Acad Sci U S A, 2011. **108**(33): p. E472-9.
21. Padrick, S.B., et al., *Hierarchical regulation of WASP/WAVE proteins.* Mol Cell, 2008. **32**(3): p. 426-38.
22. Egile, C., et al., *Mechanism of filament nucleation and branch stability revealed by the structure of the Arp2/3 complex at actin branch junctions.* PLoS Biol, 2005. **3**(11): p. e383.
23. Nolen, B.J., R.S. Littlefield, and T.D. Pollard, *Crystal structures of actin-related protein 2/3 complex with bound ATP or ADP.* Proc Natl Acad Sci U S A, 2004. **101**(44): p. 15627-32.
24. Robinson, R.C., et al., *Crystal structure of Arp2/3 complex.* Science, 2001. **294**(5547): p. 1679-84.
25. Rouiller, I., et al., *The structural basis of actin filament branching by the Arp2/3 complex.* J Cell Biol, 2008. **180**(5): p. 887-95.
26. Beltzner, C.C. and T.D. Pollard, *Identification of functionally important residues of Arp2/3 complex by analysis of homology models from diverse species.* J Mol Biol, 2004. **336**(2): p. 551-65.
27. Vorobiev, S., et al., *The structure of nonvertebrate actin: implications for the ATP hydrolytic mechanism.* Proc Natl Acad Sci U S A, 2003. **100**(10): p. 5760-5.
28. Martin, A.C., M.D. Welch, and D.G. Drubin, *Arp2/3 ATP hydrolysis-catalysed branch dissociation is critical for endocytic force generation.* Nat Cell Biol, 2006. **8**(8): p. 826-33.
29. Dayel, M.J. and R.D. Mullins, *Activation of Arp2/3 complex: addition of the first subunit of the new filament by a WASP protein triggers rapid ATP hydrolysis on Arp2.* PLoS Biol, 2004. **2**(4): p. E91.
30. Le Clainche, C., D. Pantaloni, and M.F. Carlier, *ATP hydrolysis on actin-related protein 2/3 complex causes debranching of dendritic actin arrays.* Proc Natl Acad Sci U S A, 2003. **100**(11): p. 6337-42.
31. Mahaffy, R.E. and T.D. Pollard, *Kinetics of the formation and dissociation of actin filament branches mediated by Arp2/3 complex.* Biophys J, 2006. **91**(9): p. 3519-28.
32. Weaver, A.M., et al., *Cortactin promotes and stabilizes Arp2/3-induced actin filament network formation.* Curr Biol, 2001. **11**(5): p. 370-4.
33. Blanchoin, L., T.D. Pollard, and R.D. Mullins, *Interactions of ADF/cofilin, Arp2/3 complex, capping protein and profilin in remodeling of branched actin filament networks.* Curr Biol, 2000. **10**(20): p. 1273-82.
34. Nobes, C.D. and A. Hall, *Rho, rac, and cdc42 GTPases regulate the assembly of multimolecular focal complexes associated with actin stress fibers, lamellipodia, and filopodia.* Cell, 1995. **81**(1): p. 53-62.
35. Takenawa, T. and S. Suetsugu, *The WASP-WAVE protein network: connecting the membrane to the cytoskeleton.* Nat Rev Mol Cell Biol, 2007. **8**(1): p. 37-48.

36. Stradal, T.E. and G. Scita, *Protein complexes regulating Arp2/3-mediated actin assembly.* Curr Opin Cell Biol, 2006. **18**(1): p. 4-10.
37. Zalevsky, J., et al., *Different WASP family proteins stimulate different Arp2/3 complex-dependent actin-nucleating activities.* Curr Biol, 2001. **11**(24): p. 1903-13.
38. Miki, H., et al., *Induction of filopodium formation by a WASP-related actin-depolymerizing protein N-WASP.* Nature, 1998. **391**(6662): p. 93-6.
39. Miki, H., S. Suetsugu, and T. Takenawa, *WAVE, a novel WASP-family protein involved in actin reorganization induced by Rac.* EMBO J, 1998. **17**(23): p. 6932-41.
40. Suetsugu, S. and A. Gautreau, *Synergistic BAR-NPF interactions in actin-driven membrane remodeling.* Trends Cell Biol, 2012. **22**(3): p. 141-50.
41. Otsuki, M., T. Itoh, and T. Takenawa, *Neural Wiskott-Aldrich syndrome protein is recruited to rafts and associates with endophilin A in response to epidermal growth factor.* J Biol Chem, 2003. **278**(8): p. 6461-9.
42. Kessels, M.M. and B. Qualmann, *Syndapins integrate N-WASP in receptor-mediated endocytosis.* EMBO J, 2002. **21**(22): p. 6083-94.
43. Schafer, D.A., et al., *Dynamin2 and cortactin regulate actin assembly and filament organization.* Curr Biol, 2002. **12**(21): p. 1852-7.
44. Miki, H., et al., *IRSp53 is an essential intermediate between Rac and WAVE in the regulation of membrane ruffling.* Nature, 2000. **408**(6813): p. 732-5.
45. Kim, A.S., et al., *Autoinhibition and activation mechanisms of the Wiskott-Aldrich syndrome protein.* Nature, 2000. **404**(6774): p. 151-8.
46. Martinez-Quiles, N., et al., *WIP regulates N-WASP-mediated actin polymerization and filopodium formation.* Nat Cell Biol, 2001. **3**(5): p. 484-91.
47. Ho, H.Y., et al., *Toca-1 mediates Cdc42-dependent actin nucleation by activating the N-WASP-WIP complex.* Cell, 2004. **118**(2): p. 203-16.
48. Tomasevic, N., et al., *Differential regulation of WASP and N-WASP by Cdc42, Rac1, Nck, and PI(4,5)P2.* Biochemistry, 2007. **46**(11): p. 3494-502.
49. Carlier, M.F., et al., *GRB2 links signaling to actin assembly by enhancing interaction of neural Wiskott-Aldrich syndrome protein (N-WASp) with actin-related protein (ARP2/3) complex.* J Biol Chem, 2000. **275**(29): p. 21946-52.
50. Innocenti, M., et al., *Abi1 regulates the activity of N-WASP and WAVE in distinct actin-based processes.* Nat Cell Biol, 2005. **7**(10): p. 969-76.
51. Rohatgi, R., et al., *Nck and phosphatidylinositol 4,5-bisphosphate synergistically activate actin polymerization through the N-WASP-Arp2/3 pathway.* J Biol Chem, 2001. **276**(28): p. 26448-52.
52. Brown, M.D. and D.B. Sacks, *IQGAP1 in cellular signaling: bridging the GAP.* Trends Cell Biol, 2006. **16**(5): p. 242-9.
53. Bensenor, L.B., et al., *IQGAP1 regulates cell motility by linking growth factor signaling to actin assembly.* J Cell Sci, 2007. **120**(Pt 4): p. 658-69.
54. Le Clainche, C., et al., *IQGAP1 stimulates actin assembly through the N-WASP-Arp2/3 pathway.* J Biol Chem, 2007. **282**(1): p. 426-35.
55. Torres, E. and M.K. Rosen, *Contingent phosphorylation/dephosphorylation provides a mechanism of molecular memory in WASP.* Mol Cell, 2003. **11**(5): p. 1215-27.
56. Cory, G.O., et al., *Phosphorylation of the WASP-VCA domain increases its affinity for the Arp2/3 complex and enhances actin polymerization by WASP.* Mol Cell, 2003. **11**(5): p. 1229-39.

57. Cooper, J.A. and D. Sept, *New insights into mechanism and regulation of actin capping protein.* Int Rev Cell Mol Biol, 2008. **267**: p. 183-206.
58. Pantaloni, D., C. Le Clainche, and M.F. Carlier, *Mechanism of actin-based motility.* Science, 2001. **292**(5521): p. 1502-6.
59. Akin, O. and R.D. Mullins, *Capping protein increases the rate of actin-based motility by promoting filament nucleation by the Arp2/3 complex.* Cell, 2008. **133**(5): p. 841-51.
60. Narita, A., et al., *Structural basis of actin filament capping at the barbed-end: a cryo-electron microscopy study.* EMBO J, 2006. **25**(23): p. 5626-33.
61. Kuhn, J.R. and T.D. Pollard, *Single molecule kinetic analysis of actin filament capping. Polyphosphoinositides do not dissociate capping proteins.* J Biol Chem, 2007. **282**(38): p. 28014-28024.
62. Hansen, S.D. and R.D. Mullins, *VASP is a processive actin polymerase that requires monomeric actin for barbed end association.* J Cell Biol, 2010. **191**(3): p. 571-84.
63. Witke, W., *The role of profilin complexes in cell motility and other cellular processes.* Trends Cell Biol, 2004. **14**(8): p. 461-9.
64. Didry, D., M.F. Carlier, and D. Pantaloni, *Synergy between actin depolymerizing factor/cofilin and profilin in increasing actin filament turnover.* J Biol Chem, 1998. **273**(40): p. 25602-11.
65. Bernstein, B.W. and J.R. Bamburg, *ADF/cofilin: a functional node in cell biology.* Trends Cell Biol, 2010. **20**(4): p. 187-95.
66. Andrianantoandro, E. and T.D. Pollard, *Mechanism of actin filament turnover by severing and nucleation at different concentrations of ADF/cofilin.* Mol Cell, 2006. **24**(1): p. 13-23.
67. Chan, C., C.C. Beltzner, and T.D. Pollard, *Cofilin dissociates Arp2/3 complex and branches from actin filaments.* Curr Biol, 2009. **19**(7): p. 537-45.
68. Dabiri, G.A., et al., *Listeria monocytogenes moves rapidly through the host-cell cytoplasm by inducing directional actin assembly.* Proc Natl Acad Sci U S A, 1990. **87**(16): p. 6068-72.
69. Tilney, L.G., P.S. Connelly, and D.A. Portnoy, *Actin filament nucleation by the bacterial pathogen, Listeria monocytogenes.* J Cell Biol, 1990. **111**(6 Pt 2): p. 2979-88.
70. Theriot, J.A., et al., *The rate of actin-based motility of intracellular Listeria monocytogenes equals the rate of actin polymerization.* Nature, 1992. **357**(6375): p. 257-60.
71. Theriot, J.A., et al., *Involvement of profilin in the actin-based motility of L. monocytogenes in cells and in cell-free extracts.* Cell, 1994. **76**(3): p. 505-17.
72. Egile, C., et al., *Activation of the CDC42 effector N-WASP by the Shigella flexneri IcsA protein promotes actin nucleation by Arp2/3 complex and bacterial actin-based motility.* The Journal of Cell Biology, 1999. **146**(6): p. 1319-32.
73. Goldberg, M.B. and J.A. Theriot, *Shigella flexneri surface protein IcsA is sufficient to direct actin-based motility.* Proc Natl Acad Sci USA, 1995. **92**(14): p. 6572-6.
74. Loisel, T.P., et al., *Reconstitution of actin-based motility of Listeria and Shigella using pure proteins.* Nature, 1999. **401**(6753): p. 613-6.
75. Co, C., et al., *Mechanism of actin network attachment to moving membranes: barbed end capture by N-WASP WH2 domains.* Cell, 2007. **128**(5): p. 901-13.
76. Carlier, M.F., et al., *Actin depolymerizing factor (ADF/cofilin) enhances the rate of filament turnover: implication in actin-based motility.* J Cell Biol, 1997. **136**(6): p. 1307-22.

77. Giganti, A., et al., *Actin-filament cross-linking protein T-plastin increases Arp2/3-mediated actin-based movement.* J Cell Sci, 2005. **118**(Pt 6): p. 1255-65.
78. Brieher, W.M., M. Coughlin, and T.J. Mitchison, *Fascin-mediated propulsion of Listeria monocytogenes independent of frequent nucleation by the Arp2/3 complex.* The Journal of Cell Biology, 2004. **165**(2): p. 233-42.
79. van der Gucht, J., et al., *Stress release drives symmetry breaking for actin-based movement.* Proc Natl Acad Sci U S A, 2005. **102**(22): p. 7847-52.
80. Paluch, E., et al., *Deformations in actin comets from rocketing beads.* Biophys J, 2006. **91**(8): p. 3113-22.
81. Trichet, L., et al., *VASP governs actin dynamics by modulating filament anchoring.* Biophys J, 2007. **92**(3): p. 1081-9.
82. Bernheim-Groswasser, A., et al., *The dynamics of actin-based motility depend on surface parameters.* Nature, 2002. **417**(6886): p. 308-11.
83. Cameron, L.A., et al., *Biophysical parameters influence actin-based movement, trajectory, and initiation in a cell-free system.* Mol Biol Cell, 2004. **15**(5): p. 2312-23.
84. Kuo, S.C. and J.L. McGrath, *Steps and fluctuations of Listeria monocytogenes during actin-based motility.* Nature, 2000. **407**(6807): p. 1026-9.
85. McGrath, J.L., et al., *The force-velocity relationship for the actin-based motility of Listeria monocytogenes.* Curr Biol, 2003. **13**(4): p. 329-32.
86. Delatour, V., et al., *Arp2/3 controls the motile behavior of N-WASP-functionalized GUVs and modulates N-WASP surface distribution by mediating transient links with actin filaments.* Biophys J, 2008. **94**(12): p. 4890-905.
87. Mogilner, A., *On the edge: modeling protrusion.* Curr Opin Cell Biol, 2006. **18**(1): p. 32-9.
88. Svitkina, T.M. and G.G. Borisy, *Arp2/3 complex and actin depolymerizing factor/cofilin in dendritic organization and treadmilling of actin filament array in lamellipodia.* The Journal of Cell Biology, 1999. **145**(5): p. 1009-26.
89. Higgs, H.N. and T.D. Pollard, *Regulation of actin filament network formation through ARP2/3 complex: activation by a diverse array of proteins.* Annu Rev Biochem, 2001. **70**: p. 649-676.
90. Pollard, T.D. and G.G. Borisy, *Cellular motility driven by assembly and disassembly of actin filaments.* Cell, 2003. **112**(4): p. 453-465.
91. Dabiri, G.A., et al., *Listeria monocytogenes moves rapidly through the host-cell cytoplasm by inducing directional actin assembly.* Proc Natl Acad Sci USA, 1990. **87**(16): p. 6068-72.
92. Tilney, L.G. and D.A. Portnoy, *Actin filaments and the growth, movement, and spread of the intracellular bacterial parasite, Listeria monocytogenes.* The Journal of Cell Biology, 1989. **109**(4 Pt 1): p. 1597-608.
93. Higley, S. and M. Way, *Actin and cell pathogenesis.* Curr Opin Cell Biol, 1997. **9**(1): p. 62-9.
94. Lambrechts, A., et al., *Listeria comet tails: the actin-based motility machinery at work.* Trends Cell Biol, 2008. **18**(5): p. 220-7.
95. Mullins, R.D., *Cytoskeletal Mechanisms for Breaking Symmetry.* Cold Spring Harb Perspect Biol, 2010. **2**: p. a003392.
96. Dayel, M.J., et al., *In silico reconstitution of actin-based symmetry breaking and motility.* PLoS Biol, 2009. **7**(9): p. e1000201.

97. Dickinson, R.B., *A Multi-Scale Mechanistic Model for Actin-Propelled Bacteria.* Cel. Mol. Bioeng., 2008. **1**(2-3): p. 110-121.
98. Cameron, L.A., et al., *Motility of ActA protein-coated microspheres driven by actin polymerization.* Proc Natl Acad Sci U S A, 1999. **96**(9): p. 4908-4913.
99. Cameron, L.A., et al., *Dendritic organization of actin comet tails.* Curr Biol, 2001. **11**(2): p. 130-5.
100. Welch, M.D., A. Iwamatsu, and T.J. Mitchison, *Actin polymerization is induced by Arp2/3 protein complex at the surface of Listeria monocytogenes.* Nature, 1997. **385**(6613): p. 265-9.
101. Footer, M.J., J.K. Lyo, and J.A. Theriot, *Close packing of Listeria monocytogenes ActA, a natively unfolded protein, enhances F-actin assembly without dimerization.* J Biol Chem, 2008. **283**(35): p. 23852-62.
102. Schwartz, I.M., et al., *The role of substrate curvature in actin-based pushing forces.* Curr Biol, 2004. **14**(12): p. 1094-8.
103. Upadhyaya, A., et al., *Probing polymerization forces by using actin-propelled lipid vesicles.* Proc Natl Acad Sci USA, 2003. **100**(8): p. 4521-6.
104. Giardini, P.A., D.A. Fletcher, and J.A. Theriot, *Compression forces generated by actin comet tails on lipid vesicles.* Proc Natl Acad Sci USA, 2003. **100**(11): p. 6493-8.
105. Co, C., et al., *Mechanism of Actin Network Attachment to Moving Membranes: Barbed End Capture by N-WASP WH2 Domains.* Cell, 2007. **128**(5): p. 901-913.
106. Delatour, V., et al., *Arp2/3 controls the motile behavior of N-WASP-functionalized GUVs and modulates N-WASP surface distribution by mediating transient links with actin filaments.* Biophys J, 2008.
107. Mogilner, A. and G. Oster, *Polymer motors: pushing out the front and pulling up the back.* Curr Biol, 2003. **13**(18): p. R721-33.
108. Mogilner, A. and G. Oster, *Force Generation by Actin Polymerization II: The Elastic Ratchet and Tethered Filaments.* Biophys J, 2003. **84**(3): p. 1591-1605.
109. Soo, F.S. and J.A. Theriot, *Adhesion controls bacterial actin polymerization-based movement.* Proc Natl Acad Sci USA, 2005. **102**(45): p. 16233-8.
110. Alberts, J.B. and G.M. Odell, *In silico reconstitution of Listeria propulsion exhibits nano-saltation.* PLoS Biol, 2004. **2**(12): p. e412.
111. Marchand, J.B., et al., *Interaction of WASP/Scar proteins with actin and vertebrate Arp2/3 complex.* Nature cell biology, 2001. **3**(1): p. 76-82.
112. Rebowski, G., et al., *Structure of a longitudinal actin dimer assembled by tandem w domains: implications for actin filament nucleation.* Journal of molecular biology, 2010. **403**(1): p. 11-23.
113. Dominguez, R., *The beta-Thymosin/WH2 Fold: Multifunctionality and Structure.* Annals of the New York Academy of Sciences, 2007. **1112**(1): p. 86-94.
114. Chereau, D., et al., *Actin-bound structures of Wiskott-Aldrich syndrome protein (WASP)-homology domain 2 and the implications for filament assembly.* Proceedings of the National Academy of Sciences of the United States of America, 2005. **102**(46): p. 16644-16649.
115. Dickinson, R.B. and D.L. Purich, *Clamped-filament elongation model for actin-based motors.* Biophysical Journal, 2002. **82**(2): p. 605-617.
116. Dickinson, R.B., L. Caro, and D. Purich, *Force Generation by Cytoskeletal Filament End-Tracking Proteins.* Biophysical Journal, 2004. **87**(4): p. 2838-2854.

117. Breitsprecher, D., et al., *Clustering of VASP actively drives processive, WH2 domain-mediated actin filament elongation.* EMBO J, 2008. **27**(22): p. 2943-54.
118. Kovar, D.R. and T.D. Pollard, *Insertional assembly of actin filament barbed ends in association with formins produces piconewton forces.* Proc Natl Acad Sci U S A, 2004. **101**(41): p. 14725-14730.
119. Cunningham, C.C., et al., *Actin-binding protein requirement for cortical stability and efficient locomotion.* Science, 1992. **255**(5042): p. 325-7.
120. Adams, J.C. and M.A. Schwartz, *Stimulation of fascin spikes by thrombospondin-1 is mediated by the GTPases Rac and Cdc42.* J Cell Biol, 2000. **150**(4): p. 807-22.
121. Amann, K.J. and T.D. Pollard, *Direct real-time observation of actin filament branching mediated by Arp2/3 complex using total internal reflection fluorescence microscopy.* Proc Natl Acad Sci U S A, 2001. **98**(26): p. 15009-15013.
122. Kuhn, J.R. and T.D. Pollard, *Real-time measurements of actin filament polymerization by total internal reflection fluorescence microscopy.* Biophys J, 2005. **88**(2): p. 1387-1402.
123. Spudich, J.A. and S. Watt, *The regulation of rabbit skeletal muscle contraction. I. Biochemical studies of the interaction of the tropomyosin-troponin complex with actin and the proteolytic fragments of myosin.* The Journal of biological chemistry, 1971. **246**(15): p. 4866-4871.
124. Pollard, T.D. and J.A. Cooper, *Quantitative analysis of the effect of Acanthamoeba profilin on actin filament nucleation and elongation.* Biochemistry (Mosc), 1984. **23**(26): p. 6631-6641.
125. Higgs, H.N., L. Blanchoin, and T.D. Pollard, *Influence of the C terminus of Wiskott-Aldrich syndrome protein (WASp) and the Arp2/3 complex on actin polymerization.* Biochemistry, 1999. **38**(46): p. 15212-22.
126. Palmgren, S., et al., *Interactions with PIP2, ADP-actin monomers, and capping protein regulate the activity and localization of yeast twinfilin.* J Cell Biol, 2001. **155**(2): p. 251-260.
127. Kaiser, D.A., et al., *Characterization of renatured profilin purified by urea elution from poly-L-proline agarose columns.* Cell Motil Cytoskeleton, 1989. **14**(2): p. 251-262.
128. Ono, S., et al., *Identification of an actin binding region and a protein kinase C phosphorylation site on human fascin.* J Biol Chem, 1997. **272**(4): p. 2527-33.
129. Patton, C., S. Thompson, and D. Epel, *Some precautions in using chelators to buffer metals in biological solutions.* Cell calcium, 2004. **35**(5): p. 427-431.
130. Nuccitelli, R., *A practical guide to the study of calcium in living cells*1994.
131. Achard, V., et al., *A "primer"-based mechanism underlies branched actin filament network formation and motility.* Curr Biol, 2010. **20**(5): p. 423-8.
132. Bernheim-Groswasser, A., et al., *The dynamics of actin-based motility depend on surface parameters.* Nature, 2002. **417**(6886): p. 308-311.
133. Vignjevic, D., et al., *Formation of filopodia-like bundles in vitro from a dendritic network.* J Cell Biol, 2003. **160**(6): p. 951-62.
134. Haviv, L., et al., *Reconstitution of the transition from lamellipodium to filopodium in a membrane-free system.* Proceedings of the National Academy of Sciences of the United States of America, 2006. **103**(13): p. 4906-4911.
135. Mejillano, M.R., et al., *Lamellipodial versus filopodial mode of the actin nanomachinery: pivotal role of the filament barbed end.* Cell, 2004. **118**(3): p. 363-73.

136. Popp, D., A. Yamamoto, and Y. Maeda, *Crowded surfaces change annealing dynamics of actin filaments.* Journal of molecular biology, 2007. **368**(2): p. 365-374.
137. Popp, D., et al., *Direct visualization of actin nematic network formation and dynamics.* Biochemical and biophysical research communications, 2006. **351**(2): p. 348-353.
138. Tang, J.X. and P.A. Janmey, *The polyelectrolyte nature of F-actin and the mechanism of actin bundle formation.* J Biol Chem, 1996. **271**(15): p. 8556-63.
139. Tang, J.X., et al., *Opposite effects of electrostatics and steric exclusion on bundle formation by F-actin and other filamentous polyelectrolytes.* Biochemistry, 1997. **36**(41): p. 12600-12607.
140. Köhler, S., O. Lieleg, and A.R. Bausch, *Rheological Characterization of the Bundling Transition in F-Actin Solutions Induced by Methylcellulose.* PloS one, 2008. **3**(7): p. e2736.
141. Hosek, M. and J.X. Tang, *Polymer-induced bundling of F actin and the depletion force.* Physical review E, Statistical, nonlinear, and soft matter physics, 2004. **69**(5 Pt 1): p. 051907.
142. Suzuki, A., M. Yamazaki, and T. Ito, *Polymorphism of F-actin assembly. 1. A quantitative phase diagram of F-actin.* Biochemistry, 1996. **35**(16): p. 5238-5244.
143. Vignjevic, D., et al., *Formation of filopodia-like bundles in vitro from a dendritic network.* The Journal of Cell Biology, 2003. **160**(6): p. 951-62.
144. Reymann, A.-C., et al., *Nucleation geometry governs ordered actin networks structures.* Nature Materials, 2010. **9**(10): p. 827-32.
145. Kuhn, J.R. and T.D. Pollard, *Real-time measurements of actin filament polymerization by total internal reflection fluorescence microscopy.* Biophys J, 2005. **88**(2): p. 1387-402.
146. Romani, A.M. and A. Scarpa, *Regulation of cellular magnesium.* Front Biosci, 2000. **5**: p. D720-34.
147. Romani, A. and A. Scarpa, *Regulation of cell magnesium.* Arch Biochem Biophys, 1992. **298**(1): p. 1-12.
148. Rink, T.J., R.Y. Tsien, and T. Pozzan, *Cytoplasmic pH and free Mg2+ in lymphocytes.* The Journal of Cell Biology, 1982. **95**(1): p. 189-96.
149. Bonder, E.M., D.J. Fishkind, and M.S. Mooseker, *Direct measurement of critical concentrations and assembly rate constants at the two ends of an actin filament.* Cell, 1983. **34**(2): p. 491-501.
150. Claessens, M.M.A.E., et al., *Actin-binding proteins sensitively mediate F-actin bundle stiffness.* Nature Materials, 2006. **5**(9): p. 748-753.
151. van der Gucht, J., et al., *Stress release drives symmetry breaking for actin-based movement.* Proceedings of the National Academy of Sciences of the United States of America, 2005. **102**(22): p. 7847-7852.
152. Ideses, Y., et al., *Arp2/3 branched actin network mediates filopodia-like bundles formation in vitro.* PloS one, 2008. **3**(9): p. e3297.
153. Svitkina, T.M., et al., *Analysis of the actin-myosin II system in fish epidermal keratocytes: mechanism of cell body translocation.* J Cell Biol, 1997. **139**(2): p. 397-415.
154. Svitkina, T.M., et al., *Mechanism of filopodia initiation by reorganization of a dendritic network.* J Cell Biol, 2003. **160**(3): p. 409-421.
155. Romero, S., et al., *Formin is a processive motor that requires profilin to accelerate actin assembly and associated ATP hydrolysis.* Cell, 2004. **119**(3): p. 419-429.

156. Pasic, L., T. Kotova, and D.A. Schafer, *Ena/VASP proteins capture actin filament barbed ends.* J Biol Chem, 2008. **283**(15): p. 9814-9.
157. Padrick, S.B. and M.K. Rosen, *Physical mechanisms of signal integration by WASP family proteins.* Annual review of biochemistry, 2010. **79**: p. 707-735.
158. Padrick, S.B., et al., *Hierarchical regulation of WASP/WAVE proteins.* Molecular cell, 2008. **32**(3): p. 426-438.
159. Schafer, D.A., P.B. Jennings, and J.A. Cooper, *Dynamics of capping protein and actin assembly in vitro: uncapping barbed ends by polyphosphoinositides.* J Cell Biol, 1996. **135**(1): p. 169-179.
160. Takeichi, M. and T.S. Okada, *Roles of magnesium and calcium ions in cell-to-substrate adhesion.* Experimental cell research, 1972. **74**(1): p. 51-60.
161. Takagi, J., *Structural basis for ligand recognition by integrins.* Current opinion in cell biology, 2007. **19**(5): p. 557-564.
162. Onley, D.J., et al., *Micromolar Ca2+ concentrations are essential for Mg2+-dependent binding of collagen by the integrin alpha 2beta 1 in human platelets.* The Journal of biological chemistry, 2000. **275**(32): p. 24560-24564.
163. Plow, E., et al., *Ligand binding to integrins.* Journal of Biological Chemistry, 2000. **275**(29): p. 21785.
164. Mould, A.P., S.K. Akiyama, and M.J. Humphries, *Regulation of integrin alpha 5 beta 1-fibronectin interactions by divalent cations. Evidence for distinct classes of binding sites for Mn2+, Mg2+, and Ca2+.* The Journal of biological chemistry, 1995. **270**(44): p. 26270-26277.
165. Grzesiak, J.J. and M.D. Pierschbacher, *Shifts in the concentrations of magnesium and calcium in early porcine and rat wound fluids activate the cell migratory response.* The Journal of clinical investigation, 1995. **95**(1): p. 227-233.
166. Forscher, P. and S.J. Smith, *Actions of cytochalasins on the organization of actin filaments and microtubules in a neuronal growth cone.* J Cell Biol, 1988. **107**(4): p. 1505-16.
167. Günther, T., *Concentration, compartmentation and metabolic function of intracellular free Mg2+.* Magnesium research : official organ of the International Society for the Development of Research on Magnesium, 2006. **19**(4): p. 225-236.
168. Takaya, J., et al., *Effects of Insulin and Insulin-like Growth Factor-1 on Intracellular Magnesium of Platelets* 1,* 2.* Experimental and Molecular Pathology, 1998. **65**(2): p. 104-109.
169. Matsuno, K., et al., *Cytosolic free magnesium concentration in human platelets.* Thrombosis Research, 1993. **69**(1): p. 131-137.
170. Le Clainche, C., et al., *A Hip1R-cortactin complex negatively regulates actin assembly associated with endocytosis.* EMBO J, 2007. **26**(5): p. 1199-210.
171. Bernardini, D., et al., *Magnesium and microvascular endothelial cells: a role in inflammation and angiogenesis.* Frontiers in bioscience : a journal and virtual library, 2005. **10**: p. 1177-1182.
172. Lapidos, K.A., et al., *Mg(++)-induced endothelial cell migration: substratum selectivity and receptor-involvement.* Angiogenesis, 2001. **4**(1): p. 21-28.
173. Hong, B.-Z., et al., *Vascular endothelial growth factor increases the intracellular magnesium.* Biochemical and biophysical research communications, 2006. **347**(2): p. 496-501.

174. Hong, B., et al., *Basic fibroblast growth factor increases intracellular magnesium concentration through the specific signaling pathways.* Molecules and Cells, 2009. **28**(1): p. 13-17.
175. Verkhovsky, A.B., et al., *Orientational order of the lamellipodial actin network as demonstrated in living motile cells.* Mol Biol Cell, 2003. **14**(11): p. 4667-75.
176. Maly, I.V. and G.G. Borisy, *Self-organization of a propulsive actin network as an evolutionary process.* Proc Natl Acad Sci U S A, 2001. **98**(20): p. 11324-9.
177. Lebensohn, A.M. and M.W. Kirschner, *Activation of the WAVE complex by coincident signals controls actin assembly.* Mol Cell, 2009. **36**(3): p. 512-24.
178. Abou-Kheir, W., et al., *Membrane targeting of WAVE2 is not sufficient for WAVE2-dependent actin polymerization: a role for IRSp53 in mediating the interaction between Rac and WAVE2.* J Cell Sci, 2008. **121**(Pt 3): p. 379-90.
179. Hu, X. and J.R. Kuhn, *Actin filament attachments for sustained motility in vitro are maintained by filament bundling.* PloS one, 2012. **7**(2): p. e31385.
180. Cooper, J.A., et al., *Kinetic evidence for a monomer activation step in actin polymerization.* Biochemistry, 1983. **22**(9): p. 2193-202.
181. Kuhn, J.R. and T.D. Pollard, *Real-time measurements of actin filament polymerization by total internal reflection fluorescence microscopy.* Biophysical Journal, 2005. **88**(2): p. 1387-1402.
182. Higgs, H.N., L. Blanchoin, and T.D. Pollard, *Influence of the C terminus of Wiskott-Aldrich syndrome protein (WASp) and the Arp2/3 complex on actin polymerization.* Biochemistry, 1999. **38**(46): p. 15212-15222.
183. Yoshimura, S.H., et al., *Development of glutathione-coupled cantilever for the single-molecule force measurement by scanning force microscopy.* FEBS Lett, 2006. **580**(16): p. 3961-5.
184. Murphy, D.B., et al., *Direct demonstration of actin filament annealing in vitro.* J Cell Biol, 1988. **106**(6): p. 1947-54.
185. Schafer, D.A., P.B. Jennings, and J.A. Cooper, *Dynamics of capping protein and actin assembly in vitro: uncapping barbed ends by polyphosphoinositides.* J Cell Biol, 1996. **135**(1): p. 169-79.
186. Hertzog, M., et al., *The beta-thymosin/WH2 domain; structural basis for the switch from inhibition to promotion of actin assembly.* Cell, 2004. **117**(5): p. 611-23.
187. Kim, T., J.A. Cooper, and D. Sept, *The interaction of capping protein with the barbed end of the actin filament.* J Mol Biol, 2010. **404**(5): p. 794-802.
188. Egile, C., et al., *Activation of the CDC42 effector N-WASP by the Shigella flexneri IcsA protein promotes actin nucleation by Arp2/3 complex and bacterial actin-based motility.* J Cell Biol, 1999. **146**(6): p. 1319-32.
189. Chan, K.T., S.J. Creed, and J.E. Bear, *Unraveling the enigma: progress towards understanding the coronin family of actin regulators.* Trends Cell Biol, 2011. **21**(8): p. 481-8.